HYPERSPECTRAL IMAGING IN SWIR AND LWIR OF LOW-GRADE METAMORPHIC ROCKS

Exaud Jeckonia Humbo

February, 2019

SUPERVISORS:

Dr. F.J.A. (Frank) van Ruitenbeek

W.H. (Wim) Bakker, MSc

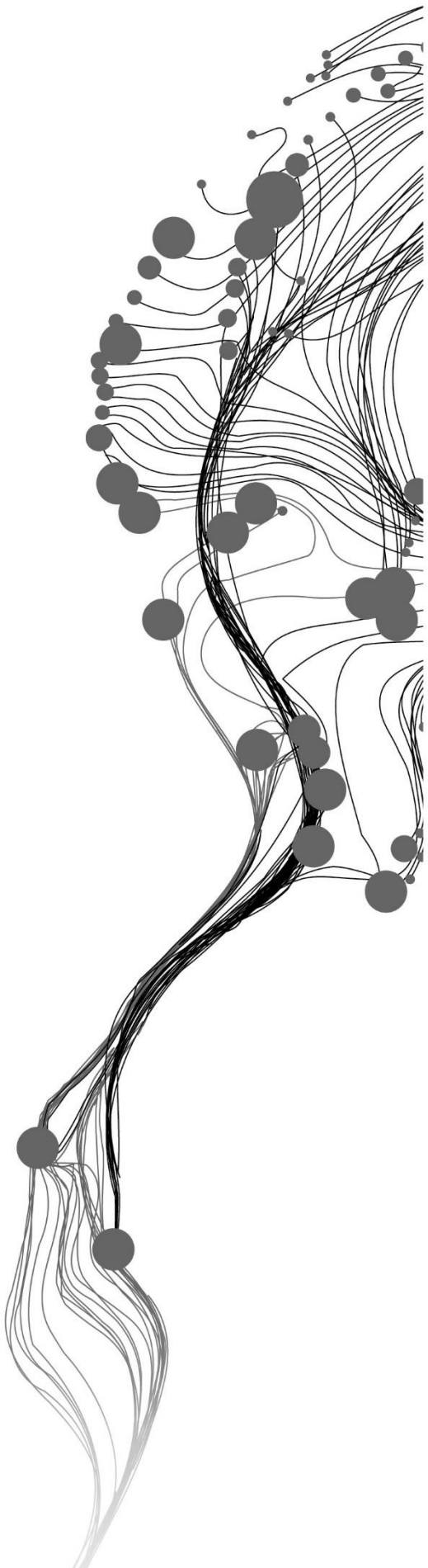

HYPERSPECTRAL IMAGING IN SWIR AND LWIR OF LOW-GRADE METAMORPHIC ROCKS

Exaud Jeckonia Humbo

Enschede, The Netherlands, February, 2019

Thesis submitted to the Faculty of Geo-Information Science and Earth Observation of the University of Twente in partial fulfilment of the requirements for the degree of Master of Science in Geo-information Science and Earth Observation.

Specialization: Geological Remote Sensing

SUPERVISORS:

Dr. F.J.A. (Frank) van Ruitenbeek

W.H. (Wim) Bakker MSc

THESIS ASSESSMENT BOARD:

Prof. Dr. F.D van der Meer (Chair)

Prof. Dr. Kim Hein (External Examiner, emeritus professor University of the Witwatersrand, South Africa)

ABSTRACT

This study presents the first investigation of the effectiveness of the hyperspectral imaging method on studying metamorphic grades. Low-grade metamorphic rocks, in particular, host multitude high-grade mineral deposits of economic importance. The research focused on combining laboratory-based hyperspectral imaging of SWIR (1.0 – 2.5 μm) and LWIR (7.5 – 14 μm) ranges to study low-grade metamorphic rocks of the Pilbara greenstone belts, Western Australia. Moreover, it involves quantitative estimates of metamorphic mineral assemblages, the interpretation of metamorphic grades and evaluates the dominant control of the metamorphic mineral assemblages. The determination of mineral assemblages, the chemistry of metamorphic rocks and interpretation of the metamorphic grade were widely studied using conventional methods such as petrography, isotopes, XRF and XRD. Recently, a point measurement, an ASD fieldspec3 spectrometer was used to determine metamorphic grades of Pilbara greenstone belts, Western Australia. However, the ASD found to have disadvantages on determining good estimation of the mineralogical composition of the whole surface of the sample due to biases on taking point measurements and is difficult to identify silicate minerals like plagioclase, quartz and pyroxenes within its wavelength range of 0.35 – 2.5 μm, which can only be identified in LWIR (7.5 – 14 μm).

In this research, the hyperspectral images were acquired from 237 rock slabs in both SWIR, and LWIR ranges and the minerals were identified, classified and quantified. Twelve sets of spectral mineral assemblages were obtained by combining SWIR and LWIR mineral abundances. The determined mineral assemblages were integrated with lithogeochemical data and the wavelength position related to MgOH absorption features measured by ASD from the same rock slabs. The results showed a systematic variation of the spectral mineral assemblages along the wavelength position of MgOH absorptions. This variation is dominantly controlled by the change in temperature and pressure condition reached during metamorphism (metamorphic grade). Moreover, three different metamorphic facies, namely lower amphibolite, greenschist and prehnite-pumpellyite facies were determined and interpreted from the spectral mineral assemblages. Furthermore, it was observed that metamorphism decreases towards a longer wavelength of the MgOH absorptions wavelength position.

Therefore, hyperspectral imaging of SWIR and LWIR has addressed well the limitations of the point measurement ASD fieldspec3 spectrometer. Furthermore, the method found to have advantages over the ASD on the number of minerals can be identified, mineral quantification and the ability to separate mixed spectra. The results obtained in this study provides compelling evidence about the ability of the combined SWIR and LWIR hyperspectral imaging for determining the metamorphic grade and assessing the dominant control of metamorphic mineral assemblages, which is relevant in the classification of low-grade metamorphosed volcanic rocks. Additionally, hyperspectral methods may be important for regional geological mapping and successful exploration of metamorphic mineral deposits hosted in the greenstone belts. This study revealed a new approach of using combined imaging spectrometry of SWIR and LWIR to geologists and researchers working on the field of tectonism and ore exploration of metamorphic mineral deposits of Pilbara Craton, Western Australia and other related metamorphic terranes

.

ACKNOWLEDGEMENTS

First, I would like to express my hearty gratitude to my supervisors Dr Frank van Ruitenbeek and Wim Bakker for their invaluable guidance, encouragement, assistance and the fruitful discussion that sharpen my knowledge and scientific way of thinking.

I extend my gratitude to Dr Fiorenza Dion for the fully assistance on XRD and thin section interpretation.

My special thanks go to all ITC – ESA staffs and lecturers for their cooperation during the whole time of my studies.

I'm beyond grateful to my fellow students Amarjargal Davaadorj, Oroghene Chokor, Mickiale Giday, Mathew Kamau and the entire GRS class of 2017 – 2019 for their full cooperation particularly in the interclass discussion, peer reviews and assistance during the whole time of studies.

Deep thanks go to the Netherland Fellowship Program (NFP) for awarding me an opportunity to broaden my knowledge and experience.

Lastly but not least, I give thanks to all my friends and family for their support and encouragement during my study time.

TABLE OF CONTENTS

LIST OF FIGURES

LIST OF TABLES

1. INTRODUCTION

1.1. Research background

Metamorphism of rocks refers to partial or complete recrystallization of the existing rocks due to geological processes (e.g., plate tectonics, igneous intrusion), that results into formation of new minerals or the structural and chemical modification of the existing ones if involved processed where pressure and temperature change. Three factors have been identified to control metamorphism: the bulk chemical composition of the original (precursor/protolith) rock, the pressure and temperature "P-T" condition reached during the metamorphism (metamorphic grades) and the composition of any fluid phase which has interacted with the rocks that were present at the time of metamorphism. The set of mineral assemblages in metamorphic rocks is the indication of the temperature and pressure environment (metamorphic facies) that the rock was subjected to. Bucher & Grapes (2011), indicated that metamorphic facies show a regular relationship between bulk chemical composition and particular metamorphic grade, such that metamorphic facies vary gradually in correspondence with the variation in the bulk rock composition and metamorphic grade, although of other variables such as fluid may also be important.

Metamorphic rocks have substantial significance because they host high-grade mineral deposits of economic importance. Mineral deposits associated with metamorphic rocks have a strong relation with metamorphic grades, in particular, low-grade metamorphic rocks. According to Groves et al. (1998), Archaean greenstone belts (low-grade metamorphism) show a strong association with gold deposits, e.g., Kalgoorlie Au deposit, Australia. However, some high-grade metamorphic rocks are also found hosting various types of mineral deposits, such as the East African Mozambique belt which hosts gemstones, gold, coal, base metals and construction materials resources (Lehto & Gonçalves, 2002).

An exploration target of metamorphic mineral deposits is to identify diagnostic mineral assemblages of metamorphic facies such as greenschist, amphibolite, pyroxene hornfels, etc. Determination of the mineral assemblages and chemistry of metamorphic rocks and interpretation of metamorphic grade was widely studied using conventional methods such as petrography, isotopes, XRF, XRD, etc. (Appaji & Kumararaman, 2013; Hallberg & Glikson, 1981; Kiyokawa et al., 2002; White, 2003). Petrographic studies provide the spatial distribution of mineral abundances while the XRD method gives a semi-quantitative abundance of minerals within the rock sample.

Alternatively, spectral analysis techniques have been known to have a wide range of applications in geology including mineral identification and mineral alteration mapping (Van Der Meer & de Jong, 2002). For many years, the spectroscopic studies on metamorphic rocks have been focusing on the identification of hydrothermal mineral alterations related to mineral deposits (e.g., Van Ruitenbeek et al. 2006, 2012). However, very few studies have focused on the identification of metamorphic grades. Duke (1994), mapped metamorphic grade of low grade to upper amphibolite facies using laboratory and field-portable near infrared (NIR) spectrometer (0.8-2.5 μm) of white micas in metasedimentary rocks. Longhi et al. (2000; 2001) determined metamorphic grades in siliceous muscovite bearing rocks and classified the rocks using laboratory-based spectrometer with a spectral range of 0.4 – 2.5 μm (double-beam Perkin Elmer Lambda 19). Another study on the classification of metamorphic rocks was carried out by Appaji & Kumararaman, (2013) using FTIR (The Fourier Transform Infrared Spectroscopy) spectrometer. Lastly, Abweny et al. (2016) identified metamorphic grades of Pilbara greenstone belts, Western Australia using field-based portable visible-near infrared to shortwave infrared (VNIR-SWIR) 0.35-2.5 μm an ASD Fieldspec spectrometer. The results of Abweny et al. (2016)'s work showed that chlorite of varying composition, actinolite, epidote, hornblende and white mica are the main spectrally identified metamorphic minerals in the volcanic rock samples collected on the study area.

The introduction of laboratory-based hyperspectral imaging (HI) enabled to image drill core and rock samples in hundreds of contiguous bands covering from visible through shortwave to longwave infrared (VNIR-SWIR-LWIR) range with high spatial resolution and large field of view (FOV). Compared to single point measurements by field-based spectrometers, it can identify and map the spatial distribution of the

individual minerals within the rock samples at high spatial resolution from 26 μm to 400 μm pixel sizes and thus, to provide quantitative estimates of mineral abundances within the rock samples. To highlight a few recent studies using hyperspectral images of rock samples, investigation of alteration mineralogy was carried out by Acosta (2017) on mapping epithermal alteration minerals, Davaabayar (2018) on estimating mineral abundances and Mathieu et al. (2017) for alteration mapping on drill cores.

The current research aims to use laboratory-based HI along with XRD and petrographic analyses to study metamorphic grades of East Pilbara granite-greenstone terranes, in Pilbara Craton, Western Australia. The Pilbara greenstone belt hosts a number of ore deposits such as Au, Cu-Zn, Cu-Mo and Ni in mafic to ultramafic rocks consisting of a variety of different minerals. This makes the Pilbara important and suitable for studying using remote sensing spectroscopic techniques. The geologic settings of the study area and previous studies conducted in Pilbara will be provided in the following sections.

1.2. Research problem

As stated earlier, mineralogical composition of metamorphic rocks has been studied using spectral analysis techniques, but only using field spectral point measurements. However, one of the disadvantages of using point measurement is its areal coverage due to single spot measurement in the rocks sample. Measurements are performed selectively based on human decision, not covering the whole surface of the rock sample and consequently, it cannot provide good estimate about mineralogical composition of the whole rock sample.

On the other hand, laboratory HI instruments can be used to solve the point measurement problems, as they can cover the whole rock sample surface. With HI instrument, each pixel from the whole surface of the rock sample can be measured. The previous studies mostly demonstrated the ability to discriminate and quantify hydrothermal alteration minerals at different spatial and spectral resolutions using laboratory-based HI. These studies mainly used laboratory IS in the SWIR range (1000-2500nm) and very few studies in LWIR (7500-14000 nm) range. As far as I know, very little research has been published on studying the metamorphic mineralogy using laboratory HI in both SWIR and LWIR ranges.

Therefore, the current research focused on combining laboratory-based hyperspectral HI of SWIR and LWIR ranges to study metamorphic rocks of low-grade greenstone belts of East granite-greenstone terrane, in Pilbara Craton, Western Australia. The study involves the quantitative estimates of metamorphic mineral assemblages and interpretation of metamorphic grades using the obtained results of the study area and assess the dominant control of the metamorphic mineral assemblages. The spectroscopic studies on Pilbara were previously conducted by Abweny et al. (2016), who used field spectrometer to determine metamorphic grades, and van Ruitenbeek et al. (2006, 2012), who used airborne hyperspectral images to study hydrothermal alteration system in Pilbara. Thus, in Pilbara, there is no research done yet on identifying metamorphic mineral assemblages and grade of metamorphism using laboratory HI.

This aspect of using SWIR and LWIR laboratory HI to study metamorphic grade by quantifying mineral assemblages and to determine dominant control of metamorphic rocks makes it different from other spectroscopic studies. The results of this work may have a profound effect on exploration success of the metamorphic mineral deposits by adding a new approach of identifying metamorphic grades in Archean greenstone belts.

1.3. Research objective

The main objective is to determine the ability of combining short- and long- wave infrared imaging spectroscopy on quantifying metamorphic minerals of the volcanic rocks of Pilbara Greenstone Belts, and use the obtained results to determine metamorphic grades and dominant control of the metamorphic mineral assemblages.

1.3.1. Specific objectives

1. To determine abundances of metamorphic mineral assemblages from each of the rock samples.
2. To create a mineral maps from the rock samples that represent the different metamorphic grades using SWIR (1000-2500 nm) and LWIR (7500-14000 nm) imagery.
3. To interpret metamorphic grades and facies from spectrally determined mineral assemblages.

4. To determine dominant control of metamorphic mineral assemblages by assessing the influence of lithological composition of the precursor rocks on the mineralogical assemblages
5. To compare the spectrally determined results of mineral abundances by interpreting semi-quantitatively mineral assemblages with XRD and thin section analyses.
6. To compare the spectral determined results of this study with those obtained by Abweny et al. (2016) to see if similar results can be reproduced using hyperspectral image data.

1.4. Research questions

1. How can SWIR and LWIR mineralogy from both SWIR and LWIR hyperspectral images be combined and interpreted?
2. What is the dominant control of the metamorphic mineral assemblages?
3. Can Abweny et al. (2016)'s findings be reproduced and improved by using hyperspectral image data?

1.5. Research hypothesis

1. The combination of the two, SWIR and LWIR datasets provides added information to the detection of the metamorphic mineral assemblages compared to the single datasets alone.
2. The detected metamorphic mineral assemblages are dominantly controlled by bulk composition of the precursor rock. This is because, when metamorphism takes place, the chemical composition of the precursor rock counts for stability of the formed minerals as metamorphic grades change.

1.6. Study area and geological setting

1.6.1. Study area

The study area of this research is East Pilbara granite-greenstone terrane in Pilbara Craton, Western Australia. The area was selected because of three main reasons: first, the availability of the datasets such as rock samples and geochemical analytical report of the same samples. The details of the datasets have been provided in section 3.2. Secondly, is the interesting results obtained by Abweny et al. (2016), who studied metamorphic grades of the rock samples from the same study area using ASD, and concluded that it is possible to map metamorphic rocks by using SWIR spectroscopy. Lastly, the presence of different metamorphic rocks (which have dominantly metamorphosed to greenschist facies) of varying compositions hosting different types of ore minerals. The following subsection summarizes on the major units, formation, metamorphism, stratigraphy and mineralization of East Pilbara granite-greenstone terranes.

1.6.2. Geological setting

The East Pilbara granite-greenstone terrane (EP) consists of two principle lithological components: greenstone belts and granitic complexes. Greenstone belts are the well-preserved area of land bounded by tectonic structures such as faults, intrusive and sheared granitic intrusive contacts, uncomfortably overlying supercrustal rocks (Van Kranendonk et al., 2002). The greenstone belts of the study area are characterized by variety of un-altered rocks of ultramafic-mafic to intermediate volcanics sequences intruded by granitic rocks with associated sedimentary rocks that occurred within Archaean craton.

Recent studies in Archaean granite-greenstone belts of Pilbara Craton suggest of two tectonic interpretations of greenstone belts: accreted fragments of island arcs, submarine plateau and/or oceanic crust, and flood basalts that formed during continental rifting by mantle plume-induced magmatism. These seafloor tectonic processes of greenstones formation may result into formation of metasomatism or hydrothermal alteration minerals similar to those mineral assemblages that formed during regional metamorphism (Gifkins et al., 2005).

Metamorphism of the rocks in the study area developed during 3.5-2.7 Ga tectonic development of the craton. Contact metamorphism of low pressure and high temperature have affected the greenstones of Pilbara Supergroup which varies to greenschist and prehnite-pumpellyite facies as moving away from granitic rocks (Van Kranendonk et al., 2002). Amphibolite facies assemblages developed under low to medium pressures and in some places to higher pressure of kyanite-bearing schist assemblages. Petrographic

studies showed that metamorphic grade increases with depth in the sequences and towards granitoid complex. The main protoliths in the study area are ultramafic, mafic, intermediate and felsic rocks. The metamorphism of mafic and intermediate rocks gives epidote, chlorite, amphiboles, garnet, quartz and plagioclase. (Van Kranendonk et al., 2002, 2007).

Stratigraphically, EP comprises two major tectonic units: the 3.52-3.20 Ga Pilbara Supergroup and the 3.02-2.93 Ga De Grey Supergroup (Smithies et al., 2007). Pilbara Supergroup, where the rock samples of this research come from consist of four groups: Warrawoona, Kelly, Sulphur Spring and Soanesville. These groups are consist of succession of metavolcanics and metasedimentary rocks of mainly low to medium grade metamorphism. Figure 1-1 below summarizes groups and subgroups for the respective Supergroups (Van Kranendonk et al., 2007).

Regarding mineralogy, East Pilbara granite-greenstone terrane host a quite number of mineral resources. Such minerals include shear zone hosted gold deposits in basaltic and ultramafic rocks, platinum-group elements and Nickel in layered ultramafic-mafic intrusion, epithermal barite, volcanogenic Cu-Zn and porphyry Cu-Mo (Van Kranendonk, 2010).

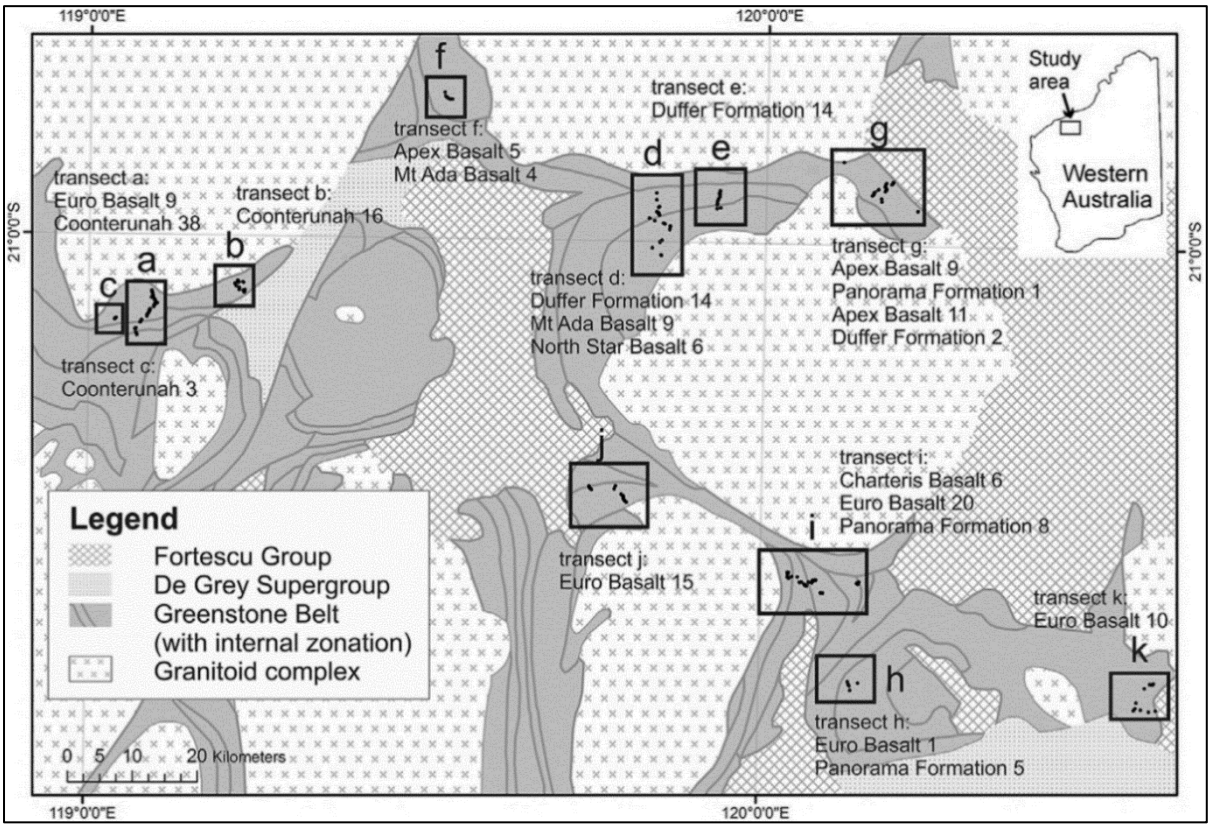

Figure 1-1: Generalized geological map of the East Pilbara Granite-Greenstone Terrane in Western Australia showing location of transects, rock samples and number of samples collected from each of the stratigraphic unit (adopted from Abweny et al., 2016)

1.7. Datasets and material feasibility

Various datasets and instruments have been used in this study. This section discusses in detail the origin of all dataset provided for this research. The section also discusses the types, specifications and the availability of all instruments that have been used for data acquisition in this research. Subsections below provide detailed descriptions about datasets and material feasibility.

1.7.1. Datasets

In this research, a total of 237 rock samples collected by the Geological Survey of Australia (GSWA) from 8 different rock units in greenstone belts of the Pilbara Supergroup (Figure 1-2) were used. The samples were collected within a geological study of the region with the purpose of identifying geochemical

characteristics of volcanic rocks sequences and to further study the tectonic settings (Smithies et al., 2007). The collected samples include the full (3.52-2.93 Ga) depositional range of the low grade metamorphic volcanic greenstone rocks within the craton, predominantly intermediate to mafic composition, and were carefully collected from fresh, unweathered rocks with no signs of alteration (Smithies et al., 2007).

All rock samples were cut into slabs (~3.0 x 6.0 cm) and scanned using HI in LWIR range of 7058 – 20561 nm in reflectance (nanometer), which was done in Sweden by Maninus Daln of Technical University of Delft. The specifications of the LWIR HI instrument can be found in Table 1-1. The 13 slides of thin sections made from 13 selected out of 237 rock samples were also provided for petrographic study (Kamps et al., 2018). The 237 rock slabs and 13 thin-section slides are available in ITC laboratory.

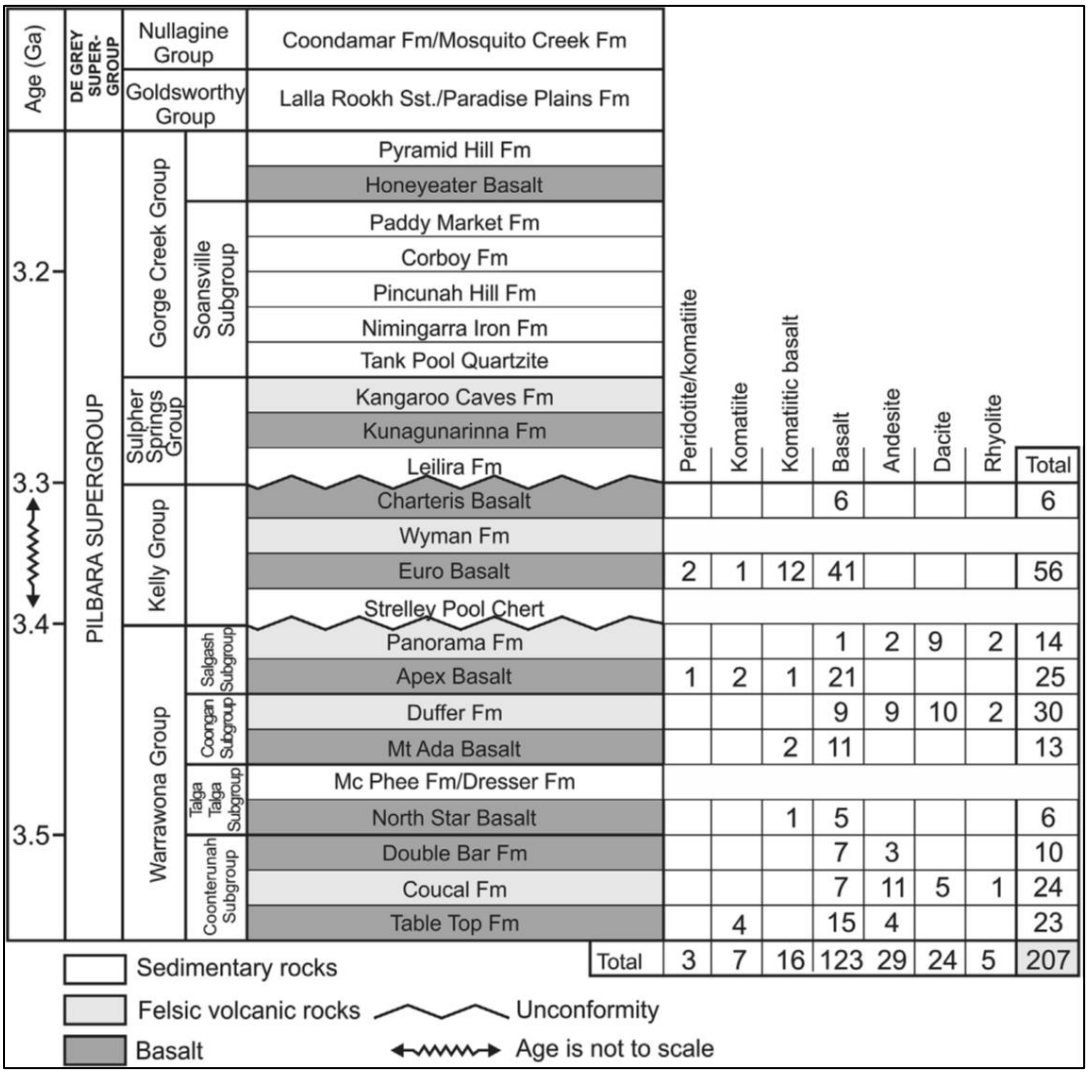

Figure 1-2: Lithostratigraphy of the Pilbara and De Grey Supergroup of the East Pilbara Granite-Greenstone Terrane Number of collected samples from each stratigraphic unit and their lithological composition is indicated (adopted from Abweny et al., 2016)

Geochemical data

A geochemical report produced by Smithies et al. (2007) which includes the analysis of the whole rock geochemistry of the same samples has been used in this study for data analysis. The report contains locations and geologic descriptions of 216 rock samples, the analytical results of major elements, trace elements and rare earth elements (REE) as well as interpretation of geochemical analysis. It also includes the spectral wavelength position of the mineral and the spectral mineralogy interpreted by The Spectra Geologist (TSG)

software. The mineral spectra were obtained using field spectrometer from the rock samples as a part of the research of Abweny et al. (2016).

1.7.2. Material feasibility

This research used three different instruments located in the Geoscience laboratory of ITC Faculty for data measurements. The Specim SWIR3 Hyperspectral camera for acquisition of hyperspectral images of slabs in SWIR range (with specifications in Table 1-1: Specifications of the hyperspectral cameras), Bruker D2 Phaser XRD diffractometer for XRD analysis and a Nikon Edipse 50/Pol. Leica Laorlux 12 Pol microscope for petrographic study of thin sections.

Table 1-1: Specifications of the hyperspectral cameras

Laboratory location		**ITC**	**SWEDEN**
No	**Specifications**	**Specim SWIR3 camera**	**AisaOWL LWIR**
1	Spectral range	1000 - 2500 nm	7058 – 20561 nm
2	Spectral resolution FWHM	12 nm	100 nm
	Spatial resolution	256 μm	400 μm
3	Spectral sampling	5.6 nm	48 nm
4	Image width (Number of pixels)	384	384
5	Signal-to-noise ratio	900 : 1	~200 - 500
6	Lens	OLES Macro	OLES 15
7	Focal length	73.3mm	15mm
8	F number	F/4	F/2
9	FOV	7.5°	32.3°
10	Number of bands	288	288

1.7.3. Software

For the data processing and analysis, this research used three software packages provided by ITC Faculty, University of Twente. Hyperspectral Python (HypPy) version 3 was used for pre-processing of hyperspectral images and wavelength mapping (Bakker, 2012). ENVI version 5.5 was used for endmember extraction, spectra library compilation, image processing, classification and statistical analysis (D. M. Rogge et al., 2007; Visual Information Solutions, 1988) while ArcGIS version 10.6.1 for various map compilation. The details of where these software were used and how are found in Chapter 2 of the methodology.

1.8. Thesis structure

This thesis is divided into four chapters. **Chapter 1,** Introduction**,** outlines research background and defines research problems, research objectives, research questions and research hypothesis. Also it briefly describes study area in terms of geological settings as well as the main datasets provided in this research. **Chapter 2**, Methodology, explains how the research carried out using specific methods which include acquisition of hyperspectral images, pre-processing, endmembers extraction and mineral classification, and finally the mineral abundances, metamorphic grades and dominant control of the metamorphic mineral assemblages. **Chapter 3**, Results, present the results of all steps followed. **Chapter 4**, Data integration and discussion, integrate various datasets used in this research by considering the main findings in results chapter by discussing the objectives and answering research questions. **Chapter 5**, Conclusions and Recommendations, provides a summary of the research and gives a final comment.

2. METHODOLOGY

This chapter presents and discusses all the methods and techniques used in this research. Figure 2-3 below summarizes the discussed methods.

2.1. Laboratory imaging spectrometry

Laboratory sample measurements include sample preparation and image acquisition. The careful setting of the hyperspectral SWIR imaging camera was to ensure that a high spatial resolution (or smallest pixel size) of the rock samples is obtained. The smallest pixel size of 256 μm was obtained by setting 30 cm distance between the scanned surface and the sensor, which gives 10 cm swath (Figure 2-2). Other instrumental settings include a frame rate of 38.9 frames/s, the speed of 10mm/s at an exposure time of 2.1 ms. For the tray holder of 60x40 cm, the target start and target stop were 662.58 mm and 1172.95 mm respectively.

2.1.1. Sample preparation

The sample preparation room in the ITC Geoscience Laboratory was used to prepare rock samples for image acquisition. The samples were arranged based on the sample numbers in ascending order in the 60x40 cm sample tray holder. The tray itself was covered by black material to avoid internal reflection of light and was filled with pure silica-rich sand which has a low spectral response in SWIR range. The tray carried 20 to 22 slab samples arranged in one column positioned in the middle of the tray in flat surface in order to be within the focus distance of the camera. For the 237 slab samples, a total of 12 batches (trays) and one batch which contain 13 slabs (of the samples selected for thin sections) were prepared (Figure 2-1b)

2.1.2. Image acquisition

All 13 prepared batches were scanned in SWIR (1000 – 2500 nm) range using the Specim SWIR3 camera at a spatial resolution of 256 μm. The scanning was done by putting one tray of samples on the sample stage of the camera, and the instrument settings were checked before recording. During the sample measurements, all lights in the room were switched off and the door and blinds of the windows were closed to avoid light interference from outside, allowing only light from the instrument. After rock scanning, the raw image data were converted into reflectance using white reference and dark current measurements.

.

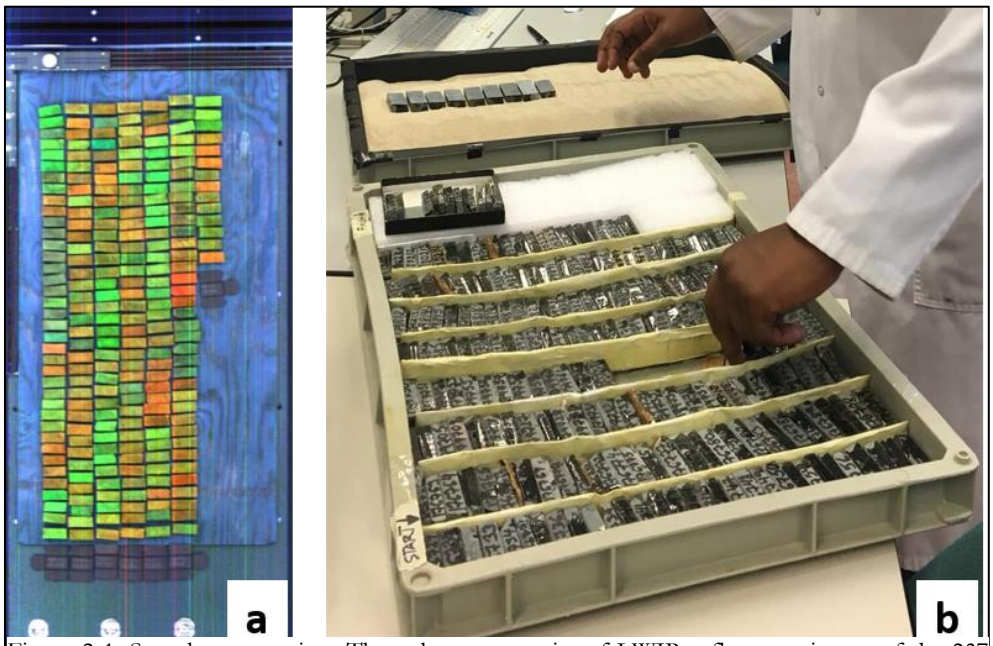

Figure 2-1: Sample preparation. The colour composite of LWIR reflectance image of the 237 rock samples (R= band33 (8563.79 nm), G= band67 (10163.50 nm), B= band102 (11810.200 nm)). b) Sample sorting for hyperspectral SWIR image acquisition

Figure 2-2: Laboratory SWIR camera with samples on the stage ready for scanning

2.2. Pre-processing

The acquired hyperspectral SWIR and LWIR images contained noisy bands and bad pixels causing processing challenges. The images were checked and cleared for any noise issues were found before proceeding with image processing (Van Der Meer et al., 2006). Pre-processing involved spatial and spectral subsetting, destriping and replacing bad pixels for both, SWIR and LWIR images. The spectral subset was done to remove noisy bands and leave the bands whose wavelength ranges show diagnostic spectral features of the minerals and high reflectance. A spatial subset was performed to exclude irregular edges of the image and to leave only rock image data. The masking tool with 'not a number' in ENVI was used to detect empty dead pixels and line striping. Using the De-striping tool in HypPy software, dead pixels and line striping were replaced by the mean values of neighbouring pixels.

2.2.1. Hyperspectral SWIR images

Some acquired hyperspectral SWIR images contained stripes caused by faulty 8th-pixel columns of the sensor. Ten images out of 13 scanned images were observed to contain the stripes, and these stripes were removed and interpolated by neighbouring pixels using Fix SWIR 8th sample tool in HypPy software. A spatial and spectral subset were done using ENVI software to remove unwanted margin and to retain SWIR 1000nm – 2500 nm wavelength range by removing band 1 (894.5100 nm) to 16 (980.1500 nm) and 288 (2511.1101 nm). This SWIR range is typically characterised by the molecular bond vibration of hydroxyl (OH), water (H_2O), carbonates (CO^-) and cation OH-bonds such as AlOH, MgOH and FeOH bond (Clark et al., 1990). Minerals that can be identified in the SWIR region have high reflectance and display characteristic features in this 1000 – 2500 nm range.

The images were further checked for more striping caused by not a number and bad pixels using maximum mean and standard deviation differences of 0.1 and 0.5 respectively in HypPy software, but there were no stripes detected. A light mean filter of 1+5+1 spatial-spectral kernel was applied to all images for smoothing.

2.2.2. Hyperspectral LWIR images

The acquired LWIR image contained all 237 rock slabs in one image (Figure 2-1a). The samples were scanned at a spatial resolution of 400 μm which is larger than the resolution of the SWIR camera. Pre-processing of the LWIR image was complicated due to many noisy bands. Before the spatial subset, a spectral subset was done from 7400 nm to 12400 nm as this wavelength region contains most abundant rock-forming minerals that display diagnostic spectral features (Salisbury et al., 1988). From the image statistics, the maximum mean and standard deviation of 0.1 and 0.05 respectively were determined and using HypPy software the first run of destriping without replacing bad pixels was done in order to define thresholds. From the offset and standard deviation images, the thresholds values of mean 0.1 and standard deviation of 0.015 were determined for the second run of destriping with the replacement of bad pixels. Next to destriping was the mean filtering using 9+9+9 to remove the outlier pixel values. Finally, the spectral subset by cutting the 1st band (band 10=7481.6602 nm) and the last two bands (band 116=12468.9004 nm and band 117=12515.9004 nm) was done because there were still stripes in these three bands.

2.3. Hyperspectral image processing

Image processing was carried out in order to map the spatial distribution of minerals in each of the rock sample and use such information to determine mineral abundances in both SWIR and LWIR images. This section describes the different types of image processing methods in detail.

2.3.1. Reflectance to Emissivity conversion of LWIR image data

The LWIR image data of the rock samples were derived in reflectance. Since the LWIR range characterizes materials' emittance at different wavelengths, a conversion from reflectance to emissivity is needed. The equation *Emissivity = 1 – Reflectance*, as described by Kirchhoff's Law (Kuenzer & Dech, 2013), was used for conversion (Kuenzer & Dech, 2013).

2.3.2. Principal Component Analysis

Hyperspectral data may have several hundred axes in such a way that a particular pixel in an image is plotted in space as a point with coordinates that corresponding to the brightness values of the pixel of the appropriate spectral components (Richards, 1993). This results in highly correlated variables and may decrease the accuracy and increase number of features during classification. Principal Component Analysis (PCA) is a mathematical procedure that transforms a number of possibly correlated variables into a smaller set of uncorrelated variables called Principal Components (PCs) (Richards, 1993). The main purpose of performing PCA in this research was to get an overview of how many materials (minerals?) are contained in the rock samples. ENVI software was used to compute PCs for each SWIR and LWIR datasets. The number of different materials was obtained by looking at the information content of the image highlighted by different colours, and the variance of the original image to the principal component was obtained from the graph of eigenvalues of that component. Although not always, it is very often that the first PC accounts for the intensity of the brightness of the materials in the particular wavelength, the succeeding PCs accounts for the remaining variability of the materials in the datasets. To highlight the different materials contained in the rock samples PC2, PC3 and PC4 were displayed in colour composite (RGB).

2.3.3. Wavelength Mapping

Wavelength mapping was used to obtain a general pattern of spatial distributions of the minerals and furthermore, to use as input images for the decision tree classification method which will be described in section 2.3.6. Wavelength mapping was performed in both SWIR and LWIR images using HypPy software created by Bakker (2012). This program identifies the wavelength of the local minimum reflectance (emissivity for the LWIR) values of the spectrum in a wavelength range specified by the user. The resultant image of one band wavelength image was then used for wavelength mapping and produces a colour map using Hue Saturation Value (HSV) fusion of an interpolated local wavelength of a minimum combined with the interpolated depth of the local minima (Bakker, 2012). From this colour map image, an overview of dominant minerals present in each pixel and pattern of the minerals in each sample have been highlighted while the abundances can be determined from the depth of absorption features as highlighted in the legend (Van Ruitenbeek et al., 2014).

For the SWIR images, the minimum wavelength was calculated at a wavelength region between 2100 nm and 2400 nm to accommodate all dominant spectral minerals that can be identified in SWIR range. The possible minerals that can be identified within this range include all that contain molecular bonds of FeOH, MgOH, AlOH and CO^- such as sulphates, carbonates and phyllosilicates (Clark et al., 1990). The resultant wavelength image was used to determine the threshold of the sample values and to mask the outlier values that existed between the gaps of the samples. The noise generated between the gaps of the samples is caused by the low reflection in the gaps during image acquisition. The depth band was used to obtain threshold values, then using the band math tool in HypPy with the expression i1[1]<0.8 and in some images i1[1]<0.9 was used to create a mask image that contains only reflectance values less than 0.8 and 0.9 respectively. With a mask image, the minimum wavelength of the same wavelength range (2100 – 2400 nm) was calculated. The depth values of 0.0 – 0.8 as observed from the histogram of the interpolated depth was set during the second step of wavelength mapper (wavelength mapping) to enhance the contrast. Similarly to SWIR, the wavelength mapping for LWIR image was done in the wavelength region between 7600 nm to 12400 nm in order to highlight and determine the wavelength position of the emissivity minima of dominant minerals. The minerals that could be identified in this region include anhydrous silicates (e.g., quartz, feldspar, pyroxenes) and carbonates (Hewson et al., 2001).

2.3.4. Endmember extraction

A spectral endmember refers to the average spectral signature of a pure surface cover type in the image that represents a class of certain type. In this research, the purpose of extracting endmembers is to identify the minerals present in the rock samples. There are several methods of extracting endmembers. With manual picking from the image, it is assumed that the image is homogeneous. Manual picking form the existing library spectra is another method, but this requires a priori knowledge of the rock composition. Minimum noisy fraction (MNF) transformation and purity pixel index (PPI) are other common methods for extracting endmembers, but they are time-consuming.

Spatial spectral endmember extraction (SSEE) was performed in both SWIR and LWIR images in order to be sure that no single mineral was left out. The method was selected because it has a high ability to obtain full spectral diversity from multiple datasets especially for endmembers with high spectral contrast (D. M. Rogge et al., 2007). It is an automated, less time-consuming method when compared to other existing endmember extracting methods.

The SSEE algorithm requires the user to define subset window size that will divide the image into equal-sized non-overlapping regions for obtaining eigenvectors of spectral variance. The minimum size of the subset window must be greater than the square root of the number of bands, and for hyperspectral images, the suggested size is ranging from minimum to 2x minimum size subset window (Rogge et al., 2012). In this research the minimum sizes of subset window used were used; that is 16 and 11 for SWIR and LWIR images respectively as they contain 271 bands for SWIR images and 105 for LWIR image. The whole wavelength ranges of SWIR images in reflectance and LWIR image in emissivity were used as inputs, which is 1000 – 2500 nm and 7600 – 12400 nm respectively.

From SSEE results, a total of 156 endmembers were extracted from SWIR images and 124 from LWIR image. The extracted endmembers were then screened by comparing them with library spectra to select the best matching endmembers. The spectral library used to compare with the image spectra are the ones from USGS speclib6a, John Hopkins University (JHU), and Arizona State University (ASU) libraries.

2.3.5. Mineral identification

The identification of minerals was made in two ways: by using literatures and by wavelength mapping. By using information from the literature, the possible minerals present in the rock samples were listed and then performing wavelength mapping by using the wavelength position of the diagnostic absorption features to highlight such a mineral. In this way, the produced wavelength maps were displayed in a linked view with the original image in ENVI software, and the Z profile (spectrum) of each highlighted colour was compared with library spectra to find the best match. This approach was used to identify minerals in SWIR images with the guide from spectral interpretation field manual G-MEX (Pontual et al., 1997). The second way is by making the wavelength maps for each of the histogram peak obtained from the minimum wavelength of the broad wavelength range (7600 – 12400 nm). This approach was useful in identifying minerals in LWIR

image because, mineral identification was not done before in the study area using LWIR. Finally, the identified minerals from both SWIR and LWIR were compared to those identified by SSEE for consistency and to ensure that all of the minerals in the samples are spectrally identified.

2.3.6. Mineral classification (Decision Tree)

The identified minerals were mapped in both SWIR and LWIR images using a multistage classification method called decision tree classifier. A decision tree, as defined by Gupta et al. (2017): "is a flowchart-like structure in which each internal node represents a test on an attribute where each branch represents the outcome of the test, and each leaf node represents a class label." It operates by using Boolean functions to construct a hierarchical 'tree-like' structure of which the expression takes as input an object or a situation described by a set of properties and output is yes/no decision (Aitkenhead, 2008).

Generally, the decision tree classifies by repetition of Boolean yes/no questions (nodes) regarding specific attributes of values or properties. Each parent node gives two more child nodes which can also be parent nodes by themselves or output nodes giving results of the expression/operations stated in the input expression. The output results are presented as the discrete classes of the stated topic which can be one thing or different. For further details on how decision tree works, a reader is referred to the following papers: (Aitkenhead, 2008; Akkaş et al., 2015; EXELIS, 2014; Gupta et al., 2017)

In this study, the minimum wavelength maps of both SWIR and LWIR were used as inputs to the decision tree classifier to produce maps of the mineral classes. The wavelength position of absorption features and depth information were used as the dominant spectral characteristic in the reflectance and emissivity spectra interpretation. This method was selected based on its advantages over the other classification method such as Spectral Angle Mapper and Linear Spectral Unmixing. For instance, it provides rapid assessment of mineral composition and focuses on mineral absorption features without prior information on the mineralogy or the rock samples and lastly, it provides objective and reproducible results (Gupta et al., 2017).

2.4. Validation

2.4.1. X-ray diffraction

For validation purpose on the mineralogy content of the samples, 20 rock samples were selected for XRD analysis. This selection was based on the lithology and mineralogy as identified by both SWIR and LWIR imaging spectroscopy. Sample preparation processes which involved slabs cutting to get a representative sample for XRD measurements, sample drying, and sample milling into powder using *Retsech PM 200 milling machine* was carried out in the ITC Geoscience Laboratory before the sample measurement. The XRD measurements were taken by inserting a sample holder containing sample powder into the *Bruker D2 X-ray diffractometer*, and each sample was scanned from 6^{o}-80^{o} range of diffraction angle at 2Φ repeatedly at the average time of one hour to get a smooth and noiseless diffractogram. The diffractograms were then interpreted using the Diffrac EVA version 3.1 software where rock-forming minerals were identified with their estimated semi abundances. The Diffrac EVA software uses a reference intensity ratio (RIR) algorithm to quantify the phases of the minerals, whereas the ratios of intensity of the diffraction peak profiles and the peak areas determine the abundance of the mineral measured. For further details on how the XRD work, a reader is referred to Lavina et al. (2014).

2.4.2. Petrographic study

The petrographic thin section is the description and systematic classification of rocks, aided by the optical microscopic examination using transmission and reflection of polarized light (Raith et al., 2012). An optical microscope was used to study the optical properties of minerals from 13 thin-section slides made from the selected rock samples to identify and estimate abundances of minerals contained in the samples. The optic phenomena observed during the microscopic investigation of minerals are described by a wave model of which, the light rays propagate as electromagnetic waves in either plane polarized light or crossed polarized light. Such optical properties used for mineral identification are the colour of a mineral, pleochroism of a mineral, mineral habit, relief, mineral cleavage and isotropism. Other optical properties include birefringence, interference colour, extinction angle, twinning, zoning and dispersion. For further details on electromagnetic waves modal, optic microscopic study of mineral identification and optic properties of

minerals a reader is referred to Raith et al. (2011). The samples selected for thin sections do not include samples scanned in LWIR. Therefore, the results from this section will be compared with SWIR and XRD results.

Furthermore, five thin sections have been analysed at the electron microprobe (EMP) using a JEOL JXA. Secondary images (SE) have been acquired, and EDS (Electron Dispersive Spectra) have been collected on single spots to determine the mineral species using an accelerating voltage of 15keVa beam current of 10nA operating in the wave dispersive mode (WDS) with a focused beam. The analyses have been performed in the laboratory of the section of inorganic and geochemistry at the German Research Centre for Geosciences in Potsdam Germany. The aim of the analyses is to verify the mineralogy using crystal chemistry analysing the grains directly.

2.5. Analysis and interpretation

The mineral classes obtained from decision tree for both SWIR and LWIR ranges were further analysed to determine mineral abundances by defining regional of interests (ROIs) as endmembers. The analysis of ROIs on the determined mineral classes from decision tree give the mineral abundances of each sample for both, SWIR and LWIR images. From the results of mineral abundances, the mineral assemblages were defined per each sample by combining mineral abundances from both SWIR and LWIR range. For the assessment of the dominant control of metamorphic mineral assemblages and interpretation of metamorphic grades, the spectroscopic data of this study and lithogeochemical data from Smithies et al. (2007) were integrated. This section will be discussed in detail in chapter 4 of data integration and discussion.

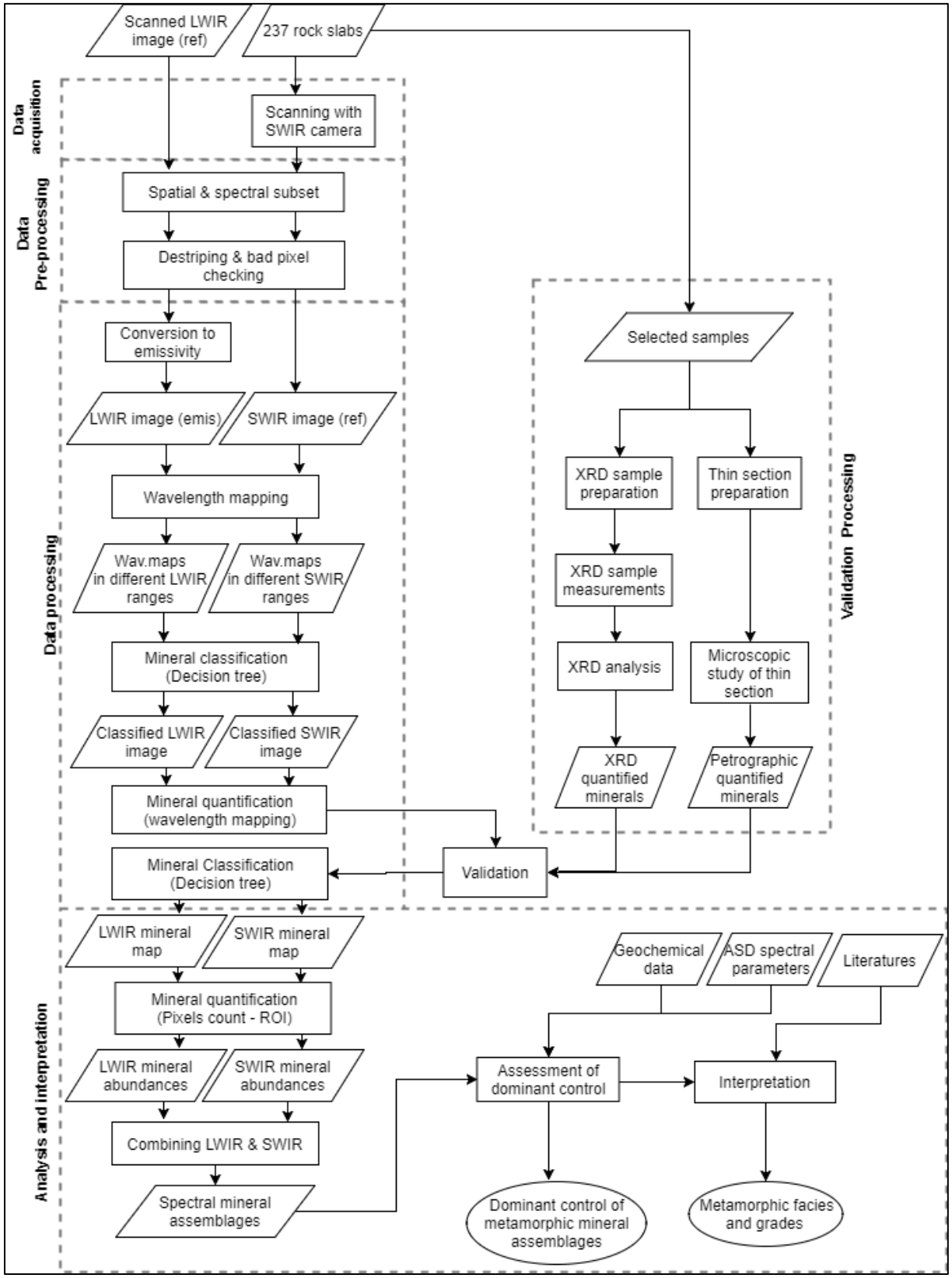

Figure 2-3: Flow-chart summarizing methodological processes

3. RESULTS

This chapter presents the results obtained from the different methods described in chapter 2. Sections below discuss results from each method. The list of sample numbers for SWIR and LWIR images re found in Appendix 2.

3.1. Principal Component Analysis (PCA)

From the principal component analysis carried out on the SWIR images, the colour composite of PC2, PC3 and PC3 in RGB gave about eight distinctive colours of uncorrelated materials such as blue, green, red, cyan, yellow, pick, maroon and pale yellow (Figure 3-1). The observed distinctive colours represent the number of meaningful components of which indicate that the rock samples contain about eight different minerals. These materials in the rock samples could be minerals. Similar procedures were applied in LWIR images, several distinctive colours were observed (Figure 3-2a).

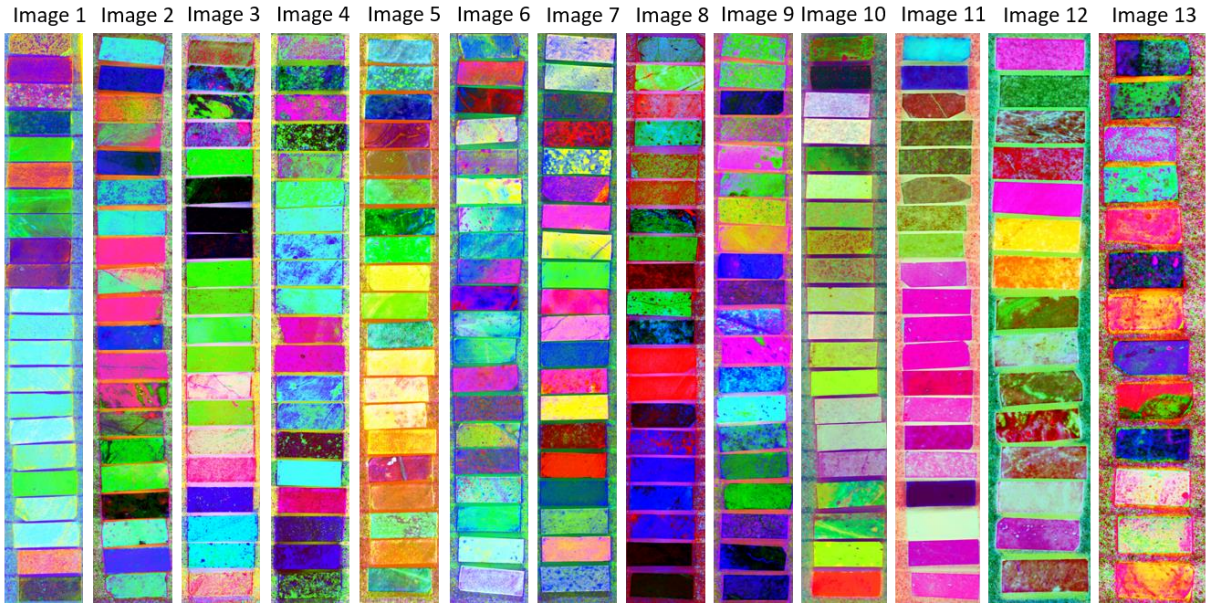

Figure 3-1: PCA of SWIR images in colour composite (RGB=PC2 PC3 PC4 respectively)

3.2. Wavelength mapping

The wavelength maps of 2.1 – 2.4 μm for SWIR images displayed distinctive colours, highlighting absorption features related to AlOH, MgOH and FeOH mineral groups (Figure 3-2). AlOH containing minerals have diagnostic features around 2.1 to 2.2 μm which were represented by colour patterns of cyan and green colours (Figure 3-2). FeOH is highlighted by yellow to orange having absorption features round 2.250 μm while MgOH is highlighted by pink to maroon colours having diagnostic absorption features around 2.3 – 2.35 μm.

The wavelength map of LWIR image at 7.6 – 12.4 μm showed diagnostic emissivity features from 8.0 μm to around 10.5 μm as represented by the colour blue, cyan, green and yellow (Figure 3-3b). However, the histogram of the minimum wavelength (7.6 – 12.4 μm) showed seven peaks representing the depth of emissivity minima of the spectral minerals covering the whole defined LWIR region at different wavelength positions. The wavelength range of each peak was defined and further stretched to highlight minerals characterised by emissivity minima (Figure 3-5).

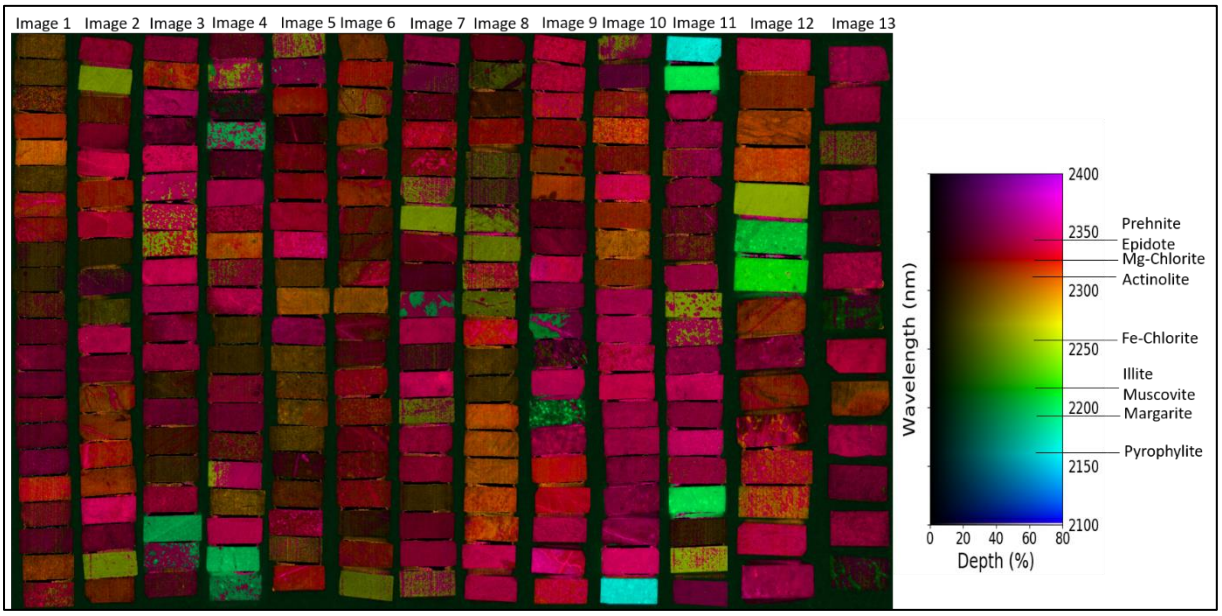

Figure 3-2: Wavelength mapping for SWIR images (2.1 – 2.4 μm)

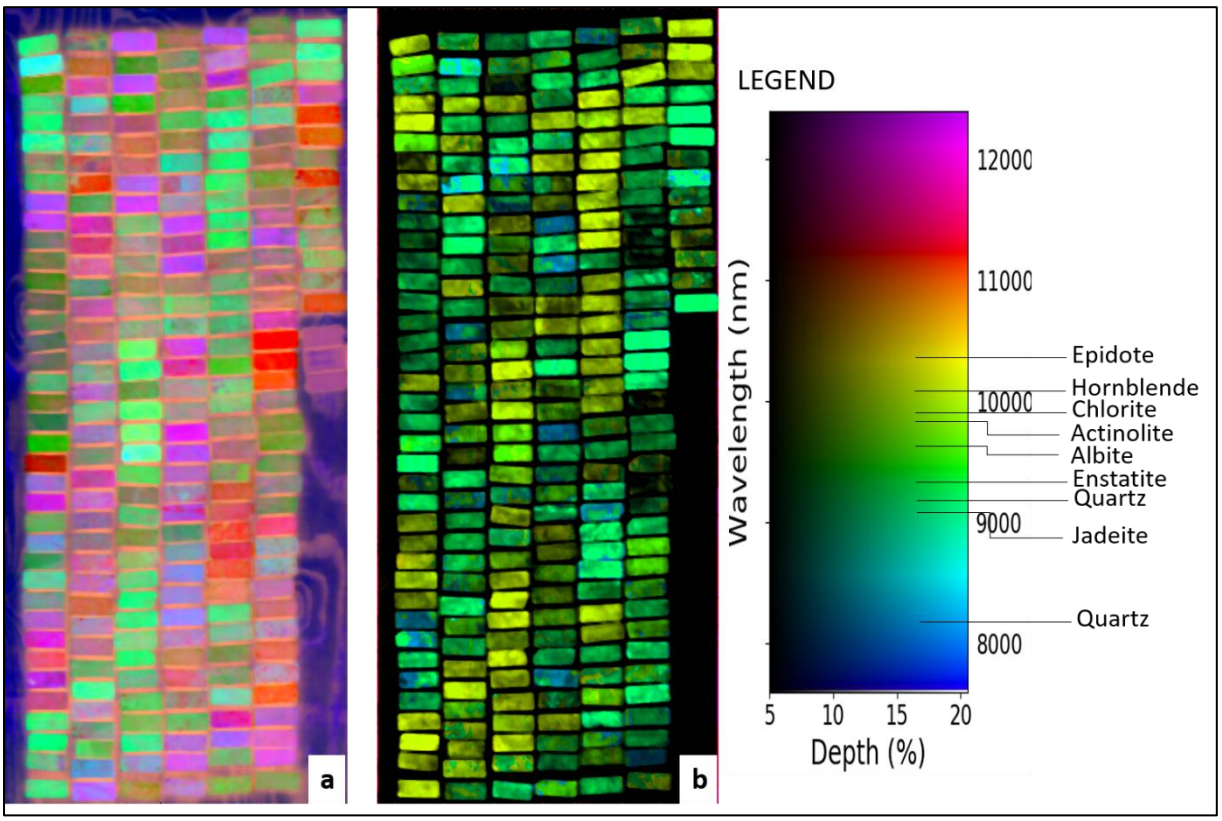

Figure 3-3: LWIR images (a) PCA in RGB colour composite (b)Wavelength mapping image showing different colour at a wavelength range of 7.6 – 12.4 μm highlighting all reststrahlen features

3.3. Spectral minerals identified from SWIR imaging spectrometry

The spectral analysis of SWIR images identified ten spectral minerals namely: Pyrophyllite, Illite, Muscovite Ca-rich mica (Margarite), Fe-rich Chlorite, Mg-rich Chlorite, intermediate (Mg-Fe) chlorite, Epidote, Prehnite and Actinolite (Table 3-1). The identified minerals are the result of detailed image and spectral

analysis of the scanned rock samples such as PCA, wavelength mapping, and SSEEu. The original scanned images and PCA images in colour composite, the interpolated minimum wavelength of first, second and third absorption features in colour composite and the wavelength map of the same sample were compared to study the spectral characteristics of the identified minerals. All spectra minerals identified in SWIR range (except margarite) were reported before in a previous study by Abweny et al. (2016) to be contained in the rock samples of the study area. The next sections discuss the spectral characteristics of each identified mineral.

Table 3-1: Summary of spectral minerals identified in SWIR

Wavelength range (μm)	**Mineral identified**	**Mineral group**	**Diagnostic absorption features (μm)**	**Mineral origin**
2.15 – 2.18	Pyrophyllite	Phyllosilicate	2.16, 2.31	Alteration product in metamorphic rock and hydrothermal deposits
2.18 – 2.23	Illite	Phyllosilicate	2.208, 2.34, 2.44	The altered product of muscovite and feldspars in the hydrothermal deposits and low-grade metamorphism
	Muscovite	Phyllosilicate	2.208, 2.34, 2.44	Alteration product of mafic mineral in igneous rocks, associated with hydrothermal deposits. Also, rock forming mineral
	Margarite	Phyllosilicate	2.197, 2.34, 2.26	Alteration product of muscovite and other aluminous minerals
2.35 – 2.27	Fe-Chlorite	Phyllosilicate	2.26, 2.34, 2.19	Alteration product of mafic mineral in igneous rocks, associated with hydrothermal deposits.
	Mg-Fe Chlorite (intermediate)	Phyllosilicate	2.34, 2.26, 2.19	
2.275 – 2.36	Mg-Chlorite	Phyllosilicate	2.32, 2.26, 2.39	
	Epidote	Epidote	2.34, 2.25, 1.55	Metamorphic mineral and Hydrothermal alteration
	Prehnite	Phyllosilicate	2.34, 2.25, 2.22	Igneous and metamorphic rocks
	Actinolite	Amphibolite	2.32, 2.399	Metamorphic rocks

3.3.1. Pyrophyllite

Pyrophyllite ($Al_2Si_4O_{10}(OH)_2$) is an early stage metamorphic mineral, member of phyllosilicate. It commonly occurs in metamorphic rocks and hydrothermal deposits. Spectrally it is found to have a first and second diagnostic absorption feature situated around 2.16 μm and 2.31 μm respectively, which fall within AlOH absorption range (Figure 3-4a).

From wavelength mapping, it is observed that pyrophyllite does not occur in many samples. Further zooming in to a wavelength map stretch at 2.15 – 2.18 μm highlighted abundant pyrophyllite in only two rock samples 179897 and 179898 (cyan colour in Figure 3-2). However, the same two samples are observed

to be highlighted by different colours in the PCA results (red and cyan colours in Figure 3-1). The colour difference in PCA is probably due to different intensity of silica alteration in these two rock samples since silica gives low absorption in SWIR range. The samples that contain pyrophyllite were collected in the Panorama Formation, and according to Smithies et al. (2007) the Panorama Formation is dominated with interbedded dacitic to rhyolitic lavas and volcaniclastic rocks, and all collected samples have been silicified. The samples have a silica content of 87.53 and 86.22 (Smithies et al., 2007) while the normal pure pyrophyllite mineral has 65.96 SiO_2 (Deer et al., 1992). Pyrophyllite is not a metamorphic mineral, it is the product of the intensive hydrothermal alteration in the Panorama Formation (Brown et al., 2006). Therefore, pyrophyllite samples were not considered in the determination of the metamorphic mineral assemblages.

3.3.2. Illite

Illite ($(Al,Mg,Fe)_2(Si,Al)_4O_{10}(OH)_2$) is a non-expanding, micaceous clay mineral of phyllosilicate group It is derived from alteration of smectite and considered as a constituent of many argillaceous sediments (Środoń, 2006). The structure of illite is similar to muscovite having two tetragonal silica sheets attached to a central octahedral sheet. Chemically, illite differs from muscovite by having more Si, Mg, Fe and water and less tetrahedral Al and K than muscovite.

Spectrally, illite can be identified by having a diagnostic single sharp AlOH absorption feature which varies in wavelength position from 2.180 – 2.228 μm. It also has two other secondary AlOH absorption features near 2.347 μm and 2.440 μm that may be due to the mixed spectra. The variation of the wavelength position of the main AlOH absorption is influenced by the Al proportion and Na/K ratio of the sericite composition in the minerals. According to Pontual et al., (1997), Na-rich sericite (paragonite) shifts the absorption feature to the shorter wavelength near 2.180 μm from normal potassic sericite at 2.200 μm, while Fe and Mg-rich sericites (phengites) substitution shifts the absorption feature to the longer wavelength position near 2.228 μm.

This diagnostic feature can be observed in all white mica minerals (illite, muscovite, phengite) and hence make it hard to distinguish them. However, illite can be differentiated from other white mica minerals such as muscovite by having deep water absorption feature around 1.912 μm which is not present in muscovites. Illite is highlighted by the green colour in sample 180223, 180225, 179740, 179899 and 180214 (Figure 3-2) from the wavelength mapping of 2.1 – 2.4 μm. The spectra of these samples were compared with USGS library spectra and good matches were obtained with muscovite and illite spectra. The presence of the water absorption feature near 1.912 μm was used to differentiate the illite from muscovite. (Figure 3-4c).

3.3.3. Muscovite

Muscovite ($KAl_2(AlSi_3O_{10})(F,OH)_2$) is a hydrated phyllosilicate mineral of aluminium and potassium mica. As the most common mica mineral, muscovite occurs in granites, pegmatites, schists and contact metamorphic rocks. Spectrally, muscovite has diagnostic absorption features at the same wavelength positions as illite. Muscovite was identified in sample 179871 (Figure 3-2) by using wavelength mapping and by spectra comparison found to have diagnostic absorption features at 2.208 μm and 2.346 μm for first and second absorption features respectively (Figure 3-4k).

3.3.4. Margarite

Margarite ($CaAl_2(Al_2Si_2)O_{10}(OH)_2$) is a calcium-rich member of a the mica group of phyllosilicate minerals. It occurs commonly in low to medium grade metamorphic rocks such as mica schists and glaucophane bearing rocks, as well as an alteration product of aluminous minerals. Margarite has never been reported before in the study area, maybe because of its tendency of forming alteration pseudomorphs with other aluminous minerals such as muscovite and paragonite which were reported in previous studies (e.g., Abweny et al., 2016; Smithies et al., 2007; Van Ruitenbeek et al., 2006). The wavelength mapping of 2.18 – 2.23 μm highlighted few samples containing margarite. The low abundances of margarite imply that it occurred in just a small area and its spatial distribution within the study area is unknown which may be another reason why it was not identified in the earlier studies.

Spectrally, margarite has a first and second deepest absorption features at 2.197 μm and 2.343 μm respectively due to AlOH absorption features, similar to muscovite and illite (Figure 3-4b). However, the

small absorption feature at 2.259 μm spectrally distinguishes margarite from other minerals in the mica group. Consequently, by comparison, the margarite spectrum looks very similar to the mixed spectrum of sericite and chlorite and ± epidote regarding overall shape and wavelength position of its absorption features. According to Pontual et al., (1997), the MgOH absorption features of the intermediate mixture of sericite and chlorite (similar to margarite spectrum) is typically dominated by sericite AlOH absorption. In this study, it was difficult to decide whether the mineral is margarite or the mixture of sericite and chlorite, but since the image spectra match better with margarite mineral than chlorite or any other phyllosilicate minerals, then the name margarite was assigned.

3.3.5. Chlorite

Chlorite belongs to the phyllosilicate minerals and can be described chemically by four endmembers based on the elemental substitution of the four elements: Mg, Fe, Ni, Mn in the silicate lattice. Chlorite has a wide range of temperature and pressure condition caused by having such a wide range of chemical composition. The compositional variation of chlorite causes it to be found in different environments. Examples of such environment are: low to medium grade metamorphic rocks, and in igneous rocks as an alteration product of mafic minerals like pyroxene, amphibole and biotite. Other environments include hydrothermal deposits associated with epidote, sericite, and sulphide minerals. Chlorite is a diagnostic species of lower greenschist facies (Haldar & Tišljar, 2014).

Spectrally, chlorite has two main diagnostic absorption features that are associated with FeOH and MgOH between 2.235 – 2.255 μm and 2.320 – 2.360 μm respectively. Typically, the intermediate composition of Fe-Mg chlorite is associated with mafic rocks, whereas ultramafic rocks may be associated more with Mg-rich chlorite. Generally, Fe- and Mg-rich chlorite are important in determining metamorphic grades. Árkai & Sadek Ghabrial (1997) indicated that chlorite crystallinity rich in Fe and Mg (with an increase of Al content) could be used to determine metamorphic grades from very low grade to greenschist facies of meta-igneous rocks. From the wavelength mapping of 2.1 – 2.4 μm, three types of chlorite, Fe-rich chlorite, Mg-rich chlorite and Mg-Fe chlorite (intermediate) could be identified using the wavelength position of their absorption features (Figure 3-4g).

Fe-rich chlorite $(Fe_5Al)(AlSi_3)O_{10}(OH)_8$ has a deep absorption feature around 2.26 μm that is associated with absorption by FeOH (Figure 3-4e). Mg-chlorite $(Mg_5Al)(AlSi_3)O_{10}(OH)_8$ was identified near 2.33 μm related to MgOH absorption (Figure 3-4d). Intermediate (Mg-Fe) chlorite looks similar to Fe-chlorite in spectral shape, the difference is that the intermediate chlorite has a deep feature around 2.34 μm related to MgOH absorption (Figure 3-4d). Intermediate (Mg-Fe) chlorite looks similar with Fe-chlorite in spectral shape, the difference is that, the intermediate chlorite has a deep feature around 2.34 μm related to MgOH absorption (Figure 3-4f). The effect of chlorite was observed in many samples due to variation of the wavelength position of the features associated with FeOH and MgOH absorptions (Figure 3-4g). These main absorption features appear to overlap with other minerals and hence makes hard to identify chlorite from other minerals. For example, spectra of chlorite and biotite have a consistent feature at FeOH absorption while at MgOH absorption the chlorite feature may be obscured by actinolite, epidote and carbonates. In this situation, the shape of the water absorption feature near 1.900 μm (Figure 3-4g) was used to distinguish chlorite from the mixtures.

3.3.6. Epidote

Epidote $(Ca_2Al_2(Fe^{3+};Al)(SiO_4)(Si_2O_7)O(OH))$ is a calcium aluminium iron silicate mineral with the varying characters based on the amount of iron present. It occurs in metamorphic rocks and in hydrothermal deposits as an alteration product of other rock forming minerals (Haldar & Tišljar, 2014). It is a common mineral in metamorphosed mafic to intermediate igneous rocks. Epidote has been used to identify grades of metamorphism based on the amount of Fe contents in epidote mineral. The Fe-rich epidote indicates low grade while the Fe-poor indicate the high grade of metamorphism (Grapes & Hoskin, 2004). Spectrally, epidote was identified by its diagnostic absorption features associated by FeOH and MgOH absorptions at 2.25 μm and 2.34 μm respectively (Figure 3-4n). Using wavelength mapping of 2.1 – 2.4 μm, epidote is observed to appear in many samples overlapping with chlorites absorptions around 2.33 – 2.34 μm. To differentiate epidote from the mixtures of chlorite and carbonates, a secondary diagnostic feature of epidote

near 1.540 μm was used. The wavelength mapping of 1.5 – 1.6 μm could be used to identify epidote from other mixtures.

3.3.7. Prehnite

Prehnite ($Ca_2Al(AlSi_3O_{10})(OH)_2$) is a member of phyllosilicate mineral formed as a result of low-grade metamorphism. It occurs as a hydrothermal mineral in veins and cavities in mafic volcanic rocks. Spectrally, prehnite was identified by its diagnostic feature at 2.34 μm due to MgOH absorption and the other two features situated at 2.22 μm and 2.25 μm associated with AlOH of sericite absorption (Figure 3-4h). The diagnostic absorption feature at 1.470 μm was used to distinguish prehnite from chlorite and epidote at MgOH absorption. During comparison between the library and image spectra of prehnite, a slightly spectral displacement was observed (Figure 3-4h). It was difficult to find out what caused displacement. Pumpellyite occurs together with prehnite, but it was not possible to spectrally identify pumpellyite in the study area. According to Abweny et al. (2016), the wavelength position of diagnostic absorption features of pumpellyite overlap with that of chlorite and hence can be obscured.

3.3.8. Actinolite

Actinolite ($Ca_2(Mg,Fe)_5SiO_{22}(OH)_2$) is an amphibole silicate mineral with more iron than magnesium. It occurs in low-grade regional metamorphism, contact metamorphism and hydrothermal alteration of pyroxene (Haldar & Tišljar, 2014). Spectral identification of actinolite is characterised by a prominent MgOH related absorption feature varying from 2.316 μm to 2.324 μm depending on the iron composition. Fe-rich actinolite shifts the absorption feature to a longer wavelength. The small shoulder feature situated near 2.300 μm is also typical of actinolite. Other diagnostic features used to differentiate actinolite from other minerals include 2.170 μm, which can be used to differentiate actinolite from talc, and the secondary MgOH feature situated around 2.39 μm. Actinolite and hornblende are two minerals that have similar spectral properties regarding spectral shapes and wavelength positions of their diagnostic absorption features. The previous study by Abweny et al., (2016) identified actinolite and hornblende using an ASD spectrometer (0.35 – 2.5 μm) based on the wavelength position of the two minerals but with no clear distinction between the two. It was not been possible to spectrally distinguish actinolite from hornblende in SWIR range. The image spectra matched with both actinolite and hornblende mineral spectra of the USGS library (Figure 3-4m). The similarity of the two minerals could be due to a large amount of the Fe^{3+} content in hornblende which shifts the wavelength position of MgOH absorptions from near 2.33 μm to the shorter wavelength similar to that of actinolite.

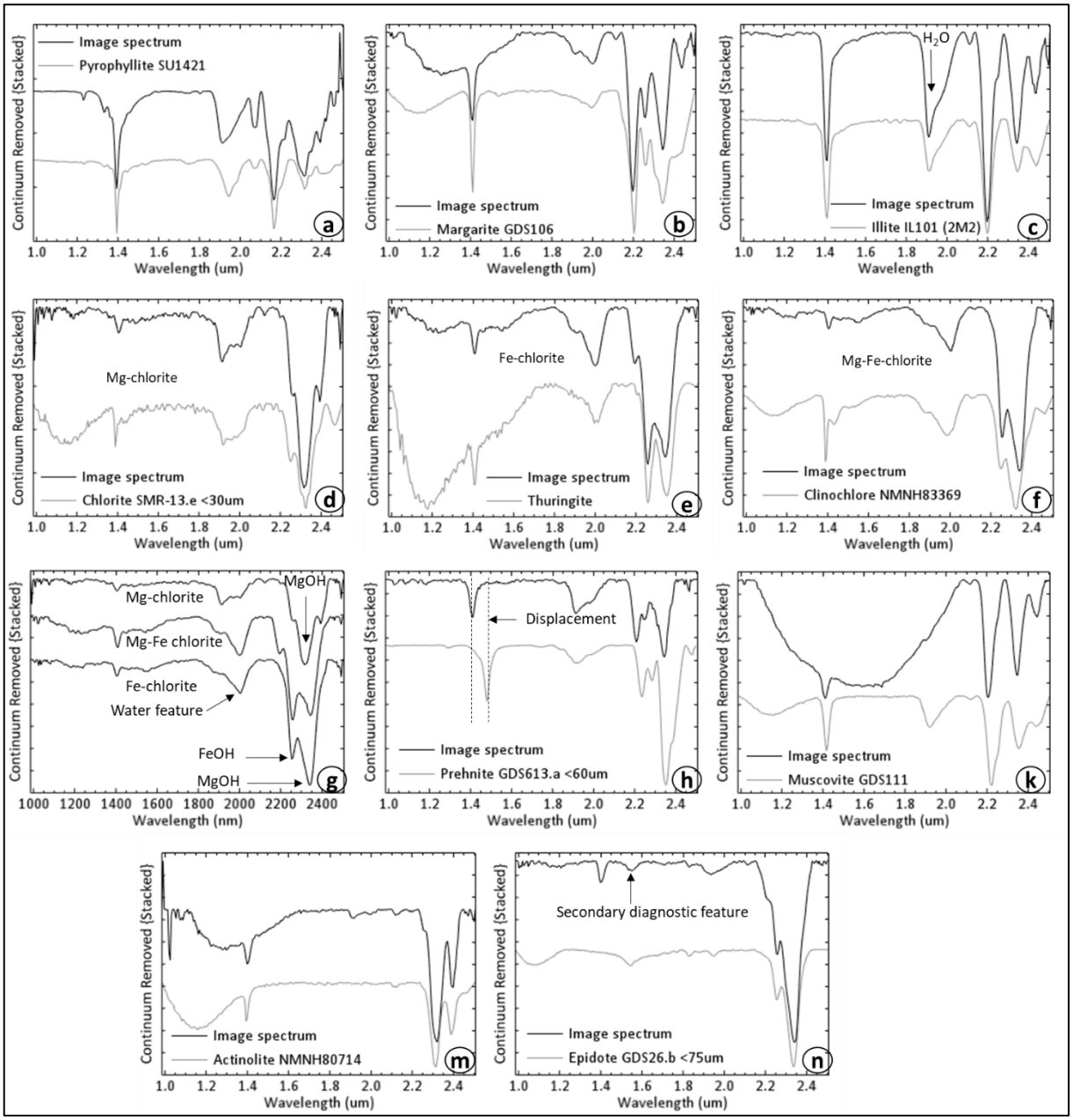

Figure 3-4: Image and library spectra comparison for mineral identification in SWIR range: a) Pyrophyllite b) Ca-rich mica (Margarite) c) Illite d) Mg-chlorite e) Fe-chlorite f) Intermediate (Mg-Fe) chlorite g) Compositional variation of chlorite from Fe-rich to Mg-rich chlorite water feature near 1.9 μm h)Prehnite k) Muscovite m) Actinolite n)Epidote.

3.4. Spectral minerals identified from LWIR imaging spectrometry

Contrary to SWIR images, mineral identification using the LWIR image was more challenging. The challenge is because there is limited information on wavelength positions of the emissivity minima of the minerals that can be identified in the LWIR range. According to Salisbury et al. (1988), the most prominent mineral features in the LWIR are found in the 8.0 – 14.0 μm wavelength region which is due to fundamental Si – O stretching vibration bands of the mineral components. In this study, mineral identification in LWIR image was successfully made by combining the results of PCA and wavelength mapping. The histogram of the minimum wavelength of 7.600 – 12.400 μm showed seven peaks representing frequency of the emissivity minima at different wavelength positions (Figure 3-5). Further wavelength mapping by stretching the wavelength of each feature and comparing the image spectra with library spectra enabled us to identify 12

different minerals (Table 3-2). These minerals are quartz, cordierite, jadeite, enstatite, chlorite, albite, hornblende, actinolite, oligoclase, epidote, muscovite and pyrophyllite as described in the next subsections.

3.4.1. Quartz

Quartz (SiO_2) is the third most abundant mineral in the Earth's continental crust and is the main constituent of granite rocks and other felsic igneous rocks. It is a common constituent in metamorphic rocks such as schists, gneiss and quartzite. It may also found in hydrothermal veins as chemical precipitates (Haldar & Tišljar, 2014). Spectrally, quartz was observed to have two emissivity minima situated at 8.23 μm and 9.22 μm (Figure 3-6a). The wavelength mapping stretch of 8.00 – 8.700 μm and 8.800 – 9.430 μm could be identified as quartz as highlighted from the histogram peak A and B of the wavelength minimum, and were observed to dominate in the samples analysed. The depth of the doublet features of quartz varied between the samples, from fewer samples having deep feature near 8.23 μm to more samples having deep feature near 9.22 μm. According to Salisbury et al. (1988), the depth variation of the doublet features together with slightly contrast variation could be influenced by the change of grain size of the rock samples. Also, mixed spectra could also be a reason. According to Fagbohun et al. (2015) the deep feature near 8.23 is due to a mixture of quartz with plagioclase and tourmaline while the mixture with other minerals causes a deep feature at 9.2 μm. In the study area, four samples from Panorama Formation have been reported to contain a high amount of silica. Other locations where samples contain silica include the Warralong greenstone belt and the Coonterunah Subgroup.

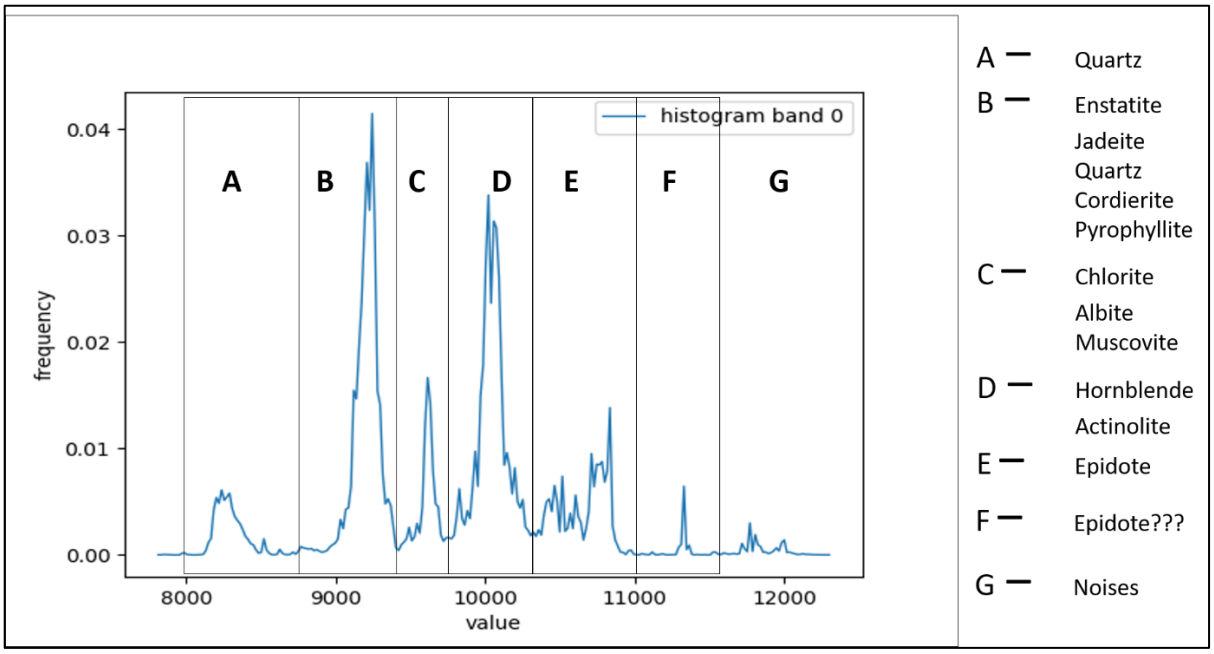

Figure 3-5: Histogram of the emissivity minima of 7.6 – 12.4 μm wavelength range

Table 3-2: Summary of spectral minerals identified in LWIR

Wavelength range (μm)	Mineral identified	Mineral group	Diagnostic features (μm)	Mineral origin
8.0 – 8.7	Quartz	Silica	8.23	Felsic (Igneous and metamorphic) rocks and hydrothermal alteration.
8.8 – 9.43	Quartz	Silica	9.22	
	Cordierite	Silica	9.27, 9.63, 11.34	Regional metamorphism of pelitic rocks
	Jadeite	Pyroxene	9.03, 9.18, 9.93	Metamorphic rocks of high P, low T
	Enstatite	Pyroxene	9.32, 10.26, 11.34	Igneous and metamorphic rocks
	Pyrophyllite	Phyllosilicate	9.08, 8.752, 10.4458	Alteration product in metamorphic rock and hydrothermal deposit
9.44 – 9.75	Chlorite	Phyllosilicate	9.9630, 10.8692, 8.752	Alteration product of mafic mineral in igneous rocks, associated with hydrothermal ore
	Muscovite	Phyllosilicate	9.6930, 9.0813	Granite, schists, gneiss and as a secondary alteration product of topaz feldspars, etc
	Albite	Plagioclase feldspar	9.65, 9.93, 8.38	Felsic rocks, alteration products
9.75 – 10.33	Hornblende	Amphibole	10.07, 9.32, 8.72	Igneous and metamorphic rocks
	Actinolite	Amphibole	9.93, 9.65, 10.87	Metamorphic rocks
	Oligoclase	Plagioclase feldspar	10.02, 9.65, 8.75	Igneous and metamorphic rocks
10.33 – 11.00	Epidote	Epidote	10.35, 10.12, 9.32	Metamorphic origin and Hydrothermal alteration

3.4.2. Cordierite

Cordierite ($(Mg, Fe)_2Al_4Si_5O_{18}$) is magnesium and iron rich crystalizes in orthorhombic systems. It usually occurs in contact or regional metamorphism of argillaceous rocks (Haldar & Tišljar, 2014). Cordierite was identified from the wavelength mapping of 8.800 – 9.430 μm peak B in Figure 3-5, having the deepest feature at 9.27 μm. (Figure 3-6b). Other diagnostic features which are situated at 9.63 μm and 11.34 μm shifted to shorter and longer wavelength respectively when compared to library spectra. The shift of wavelength position of the cordierite spectra indicates that it persists in mixtures with other minerals. The offset observed on the features around 10 μm (Figure 3-6b) are considered due to effect of applying heavy filters on the image during pre-processing stage. However, the spatial distribution of cordierite in the samples from wavelength mapping is not so significant as it was observed only in a few samples (e.g., sample 179779 and 179894 in Figure 3-3b) and it has never been reported in any of the previous studies in the study area. The limited observation of cordierite makes its occurrence in the study area uncertain, and hence the identified cordierite is probably a mixture of quartz with pyroxene.

3.4.3. Pyroxenes

Pyroxene is a rock forming inosilicate mineral occurs in igneous and metamorphic rocks. Spectrally, two endmembers of pyroxene; jadeite ($Na(Al,Fe^{3+})Si_2O_6$) and enstatite ($MgSiO_3$) were identified from wavelength mapping of 8.800 – 9.430 μm, peak B Figure 3-5. The wavelength position of the deepest emissivity minimum of jadeite varies between 9.036 μm and 9.18 μm which is probably due to a mixture of Al and Fe atoms. Other diagnostic features of jadeite are found at 9.93 μm and are shifted to a longer wavelength when compared to pure jadeite of the library spectra (Figure 3-6c). The diagnostic feature of enstatite ranges from 9.1284 μm to 9.5048 μm and additional diagnostic features are situated at 10.26 μm and 11.34 μm (Figure 3-6d). There is a slight shift in the wavelength position of the enstatite spectra features which is probably due to mixtures. The presence of pyroxenes in the study area was reported in komatiites rocks especially in Euro Basalts, Charteris Basalt and Sulphur Spring (Smithies et al., 2007).

3.4.4. Plagioclase feldspars

Plagioclase is the series of tectosilicate minerals within the feldspar group forming the major constituent mineral in the Earth's crust. It is an important mineral in petrology for the identifying composition, origin and evolution of the igneous rocks. The series of plagioclase ranges from albite ($NaAlSi_3O_8$) to anorthite ($CaAl,Si_4O_8$) endmembers, where sodium and calcium replace each other in the structure of the mineral, and other endmembers such as oligoclase, andesine, etc., can be formed depending on the compositional fraction of these two elements (Haldar & Tišljar, 2014). Spectrally, two plagioclase species were identified from wavelength mapping (peak C&D in Figure 3-5). The deepest emissivity minimum of albite at 9.65 μm and that of oligoclase at 10.02 μm match with library spectra (Figure 3-6e&f). The spectral variation between feldspars observed by the random shift of the wavelength positions of the emissivity minima, which is caused by either noises or mixed spectra, makes it difficult to identify other feldspar endmembers. Plagioclase was reported in the study area mainly in Mt Ada Basalt, Duffer Formation and Panorama Formation (Smithies et al., 2007).

3.4.5. Amphiboles

Amphibole is a group of inosilicate minerals occurs in igneous or metamorphic rocks and form monoclinic series of different types. Two common endmembers of amphibolite are hornblende and actinolite. Hornblende $(Ca,Na)_{2–3}(Mg,Fe,Al)_5(Al,Si)_8O_{22}(OH,F)_2$ is an important constituent of igneous and amphibolite rock formed by metamorphism of basalt while actinolite ($Ca_2(MgFe^{2+})_5Si_8O_{22}(OH)_2$) is a common constituent of greenschist (Haldar & Tišljar, 2014). Both hornblende and actinolite were spectrally identified by wavelength mapping of an emissivity minimum of peak D (Figure 3-5). Hornblende has diagnostic emissivity features at 10.07 μm, 9.32 μm, 8.72 μm for first, second and third deepest features respectively (Figure 3-6g), while actinolite is found to have features at 9.93 μm, 9.65 μm, 10.87 μm for first, second and third deepest features respectively (Figure 3-6h). During comparison of the image and library spectra in LWIR, it was difficult to differentiate hornblende from the actinolite due to the inconsistency of spectra libraries. For example, in USGS spectral library version 6a, the image spectrum which was identified as actinolite from the wavelength position of the diagnostic features mentioned above, when it is compared with library spectra made from *nicolet_4024* identify the image spectrum as actinolite but when matched with *nicolet_3841* identify it as hornblende. The same image spectrum, when compared with JHU library identify it as hornblende and with ASU library, actinolite. However, this study assigned the name of hornblende whenever this kind of confusion happened. Samples of hornblende and actinolite identified in LWIR image are the same as actinolite samples identified in SWIR images, but in SWIR it is difficult to differentiate the two minerals (Figure 3-3b).

3.4.6. Epidote

Epidote in the LWIR range was identified from the wavelength mapping (peak E in Figure 3-5). It has the deepest feature at 10.35 μm and other diagnostic features at 11.3 μm and 9.32 μm, with an additional subtle feature at 11.6 μm (Figure 3-6k). Epidote was also identified in the same samples it was identified in the SWIR images (Figure 3-3b and 3-2). The variation of wavelength position of the diagnostic features for the

samples that were identified as epidote indicate that epidote persists in the mixture with other minerals such as quartz, plagioclase and pyroxenes.

3.4.7. Muscovite

Spectrally, muscovite was identified from the wavelength mapping of 9.44 – 9.75 μm as represented by histogram peak C of the wavelength minimum (Figure 3-5). Two diagnostic features of muscovite of almost the same depth were observed at 9.693 μm and 9.0813 μm. The wavelength positions of these features are slightly shifted to a longer wavelength when compared to the library spectra. The shift of wavelength position may be due to a variation of potassium and aluminium in its chemical structure. As it was noted in SWIR, to differentiate muscovite and illite in LWIR is also more challenge. However, the two minerals can be differentiated by the wavelength position of their diagnostic emissivity feature. Muscovite has the deepest feature at a shorter wavelength as compared to illite feature. When the two minerals persisted in the mixtures, their depths vary proportionally (Figure 3-6m) and then become difficult to differentiate.

3.4.8. Chlorite

Chlorite was identified from the wavelength mapping by a feature of 9.44 – 9.75 μm (peak C in Figure 3-5). The diagnostic emissivity feature around 9.693 μm together with other two small features near 10.8692 μm and 8.752 μm were used for the identification of chlorite. The chlorite spectra from LWIR image were not matching well with library spectra, which is probably due to the mixture with other minerals (Figure 3-6n). The shift of wavelength position to the shorter wavelength may be due to the substitution of iron or aluminium in the position of magnesium.

3.4.9. Pyrophyllite

Pyrophyllite was identified from the wavelength mapping range of 8.8 – 9.43 μm, as defined by peak B in Figure 3-5. The deepest feature of pyrophyllite near 9.08 μm vary with 8.752 μm of the pure pyrophyllite spectra from the library (Figure 3-6p). The depth variation of the spectral features of pyrophyllite is due to a mixture of quartz and feldspar minerals. The small feature near 10.46 μm was also used as a diagnostic feature of pyrophyllite.

3.5. Mineral identification using conventional methods

3.5.1. Identified minerals using XRD analysis

This study has identified a total of 17 different minerals from XRD measurements. These minerals which include quartz, epidote, plagioclase (albite, oligoclase), amphiboles (actinolite, hornblende, katophorite), pyroxenes (enstatite, jadeite, diopside), white mica (muscovite, illite), chlorite, pyrophyllite, prehnite, cordierite and magnetite, were identified in 20 selected rock samples from 237 representing different rock composition. As it was explained earlier, Figure 3-7 below shows how minerals were identified based on peak matching. The calculated semi abundances of minerals were observed to vary between the samples depending on the rock type such as mafic/ultramafic, intermediate and felsic rock. In mafic/ultramafic rocks the minerals like epidote, plagioclase and amphiboles were most abundant. For the intermediate rocks, quartz and plagioclase were most abundant whereas felsic rocks were observed to have mostly abundant of white mica and quartz. Table 3-4 below includes detailed XRD results and observations of each measured sample.

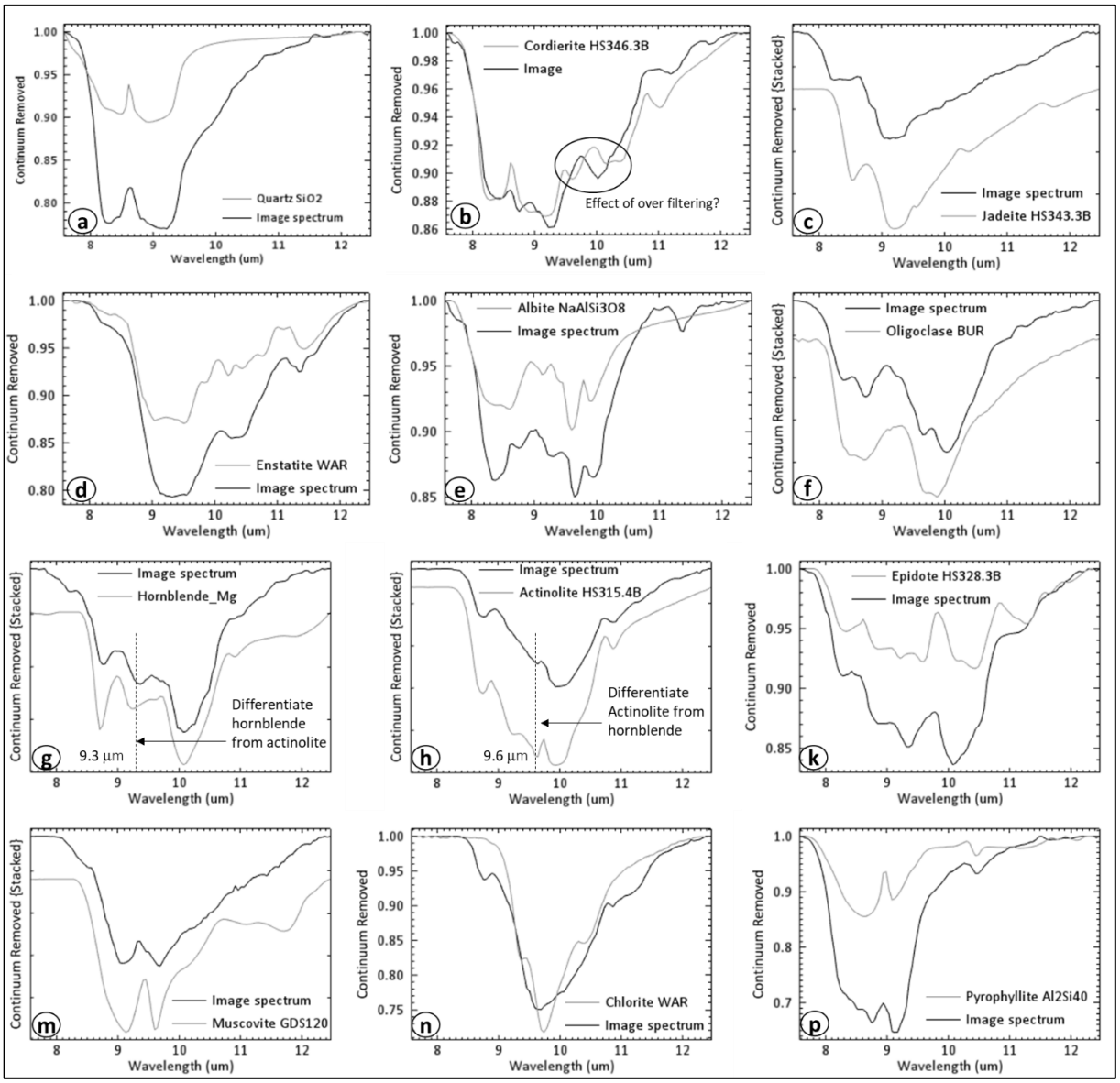

Figure 3-6: Image and library spectra comparison for mineral identification in LWIR range: a) Quartz b) Cordierite c) Jadeite d) Enstatite e) Albite f) Oligoclase g) Hornblende h) Actinolite k) Epidote m) Muscovite n) Chlorite p) Pyrophyllite.

3.5.2. Identified minerals in thin sections study

Minerals identified by optical microscope from all 13 thin sections include chlorite, quartz, muscovite, pyroxenes, plagioclase, hornblende, k-feldspars and actinolite. A detailed description of each identified mineral and the sample where a mineral was identified can be found in Table 3-3 below. However, most of the samples are altered, which makes identification of minerals in thin section under a microscope more difficult (Figure 3-8).

The interpretation of the quantified chemical composition from JEOL EDS method was made with the help of an online open mineral database from Hudson Institute of Mineralogy (www.mindat.org), and the following minerals were identified from all 5 thin sections selected for the JEOL EDS measurements: calcite, chlorite, albite, quartz, k-feldspars, ilmenite, apatite, titanite, pyroxene, magnetite, epidote, hornblende, olivine and barite (Figure 3-9, Table 3-3: Detailed thin section descriptions for the identified minerals under the optical microscope. The chemical composition has been calculated norming all the oxides to 100 so that it is not possible to determine any water occurring in the minerals.

The minerals identified in optical microscopic and JEOL EDS were compared with that identified in SWIR. The samples selected for thin section were not included in the LWIR sample scanning which is why the comparison is only for SWIR. As can be seen in Table 3-3, all observed samples were intensively altered which make it difficult to identify minerals under an optical microscope. In this case, JEOL EDS has been useful in identifying minerals as it provides a percentage of the elemental compositions of the sample. The challenge of the JEOL EDS method is in combining the measured elements in order to identify a mineral (Figure 3-9). When there is more than one mineral sharing the same elements, it is difficult to decide. When compared with SWIR, there was consistency in mineral identification except for silicate minerals like quartz, plagioclase, pyroxene, etc. which have no response in SWIR. Chlorite and epidote were identified in both JEOL EDS and SWIR but it was difficult to identify epidote using the optical microscope due to alteration of minerals.

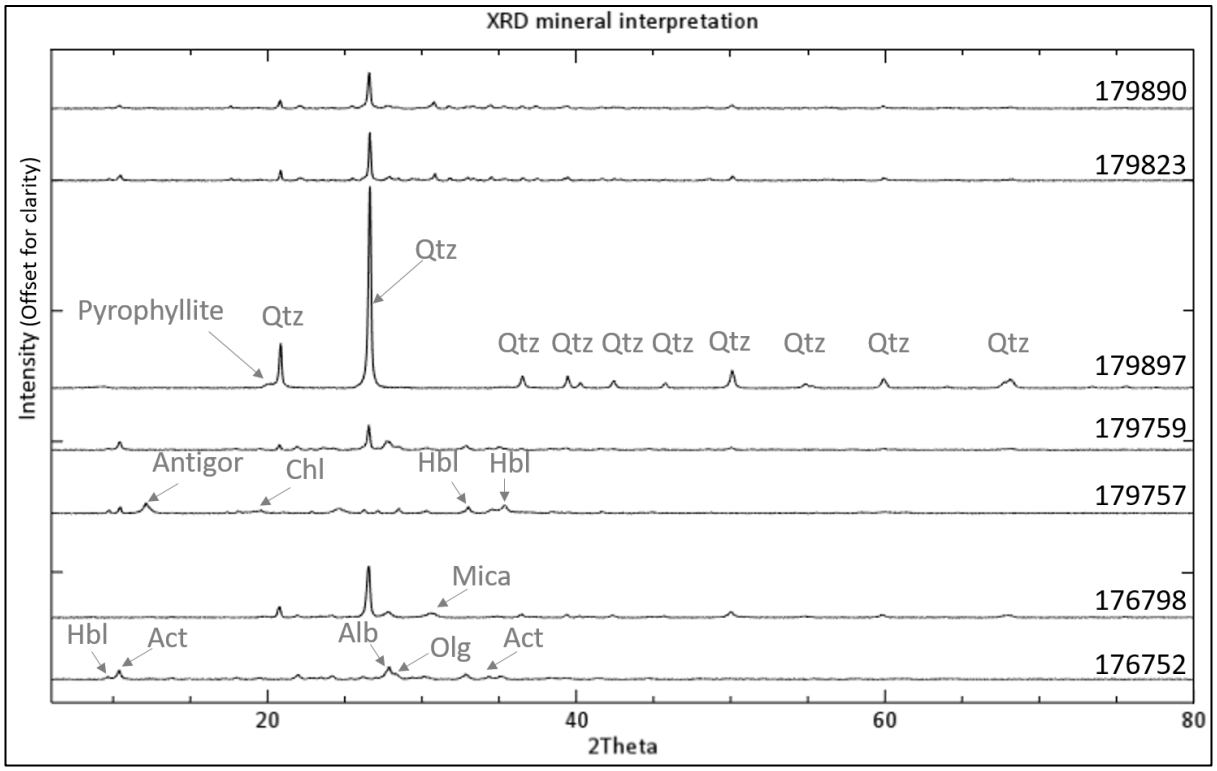

Figure 3-7: Mineral identified from the peak of the XRD patterns: Qtz=Quartz, Chl=chlorite, Alb=Albite, Olg=Oligoclase, Act=Actinolite, Hbl=Hornblende, Antigor=Antigorite.

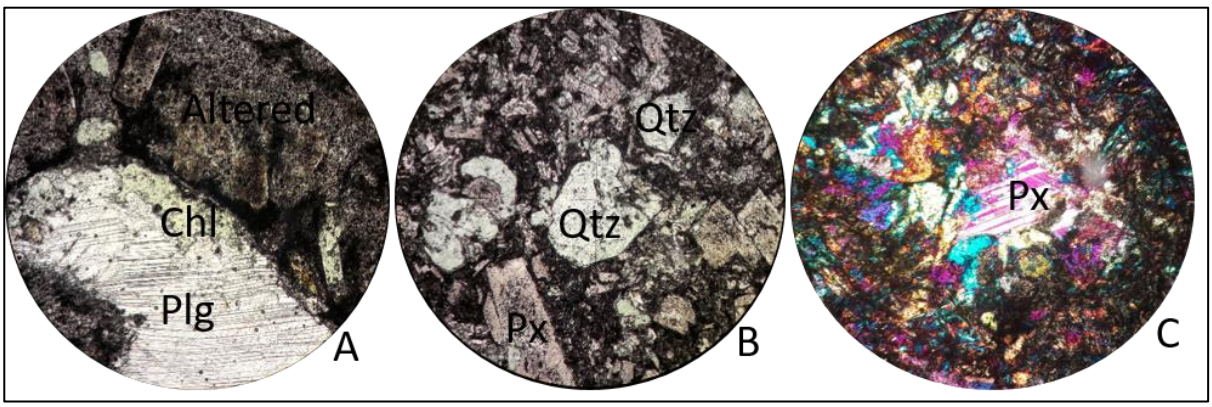

Figure 3-8: Observation of minerals under optical microscope: Chl=chlorite, Plg=plagioclase, Qtz=quartz, Px=pyroxene

Table 3-3: Detailed thin section descriptions for the identified minerals under the optical microscope

General		Thin section interpretation			Mineral identified (SWIR)
Sample	Rock Type	Observation under an optical microscope	Mineral identified		
			Microscope	JEOL EDS	
179704	Andesite	The laths (phenocrysts) of probably plagioclase due to twining are moderate to strongly altered to sericite? Clear intergrowth/twining of pyroxene (clinopyroxene). Rarely patches of chlorite may be after plagioclase/pyroxene. Few grains of individual disseminated quartz.	Plagioclase Pyroxene Chlorite Quartz		Epidote Mg-Fe-chlorite
179708	Dacite	Euhedral crystals of chlorite showing high relief. Moderately altered biotite to chlorite. Rounded quartz, disseminated	Chlorite Biotite Pyroxene Quartz		Epidote Mg-Fe-chlorite
179711	Dacite	Patches of disseminated chlorite. Strongly altered laths showing twining like clinopyroxene? An altered fine-grained matrix of groundmass containing rock fragments	Chlorite Pyroxene?		Epidote Mg-chlorite
179715	Basalt	Patches of chlorite dominated. Euhedral crystals of quartz. Altered sheets/flakes of mica?	Chlorite Quartz Mica?		Epidote Mg-chlorite
179716	Dacite	Large crystal (laths) of altered plagioclase to sericite? Showing twining. Patches of chlorite. Pyroxene altered chlorite/carbonate?	Plagioclase Chlorite Biotite Pyroxene Quartz	Olivine Quartz Epidote Albite	Epidote
179717	Basalt	Altered coarse-grained lithic fragments in the groundmass of fine-grained matrix. Occasional altered flaky/sheets of mica (Muscovite?). Intensively altered laths of plagioclase	Muscovite Chlorite Plagioclase		Epidote Mg-Fe chlorite Mg-chlorite
179718	Andesite	Mafic minerals (pyroxene, hornblende, Olivine) intensively altered to chlorite and sericite/carbonate? In the fine grain groundmass	Pyroxene? Hornblende Chlorite Olivine?		Epidote

General		Thin section interpretation			Mineral identified (SWIR)
Sample	Rock Type	Observation under an optical microscope	Mineral identified		
			Microscope	JEOL EDS	
179720	Andesite	Patches of chlorite after plagioclase? Strongly altered phenocrysts of mafic mineral showing twining (pyroxene?) in the fine-grained matrix.	Chlorite pyroxene		Epidote Mg-chlorite
179722	Andesite	Abundant patches of chlorite. Moderate altered twinned laths of pyroxene. Rarely disseminated crystals of mica (muscovite?) showing basal cleavage. Intensively altered minerals in the fine-grained groundmass	Chlorite Pyroxene Mica	Epidote Iron Quartz Titanite Chlorite	Epidote Mg-chlorite
179724	Rhyolite	Strongly altered phenocryst in the fine-grained matrix groundmass.	Hornblende Chlorite		Margarite?
179725	Basalt	Altered coarse-grained lithic fragments in the groundmass of fine-grained matrix. Intensively altered laths of plagioclase to chlorite.	Plagioclase Quartz Chlorite Pyroxene	Titanite Calcite Chlorite Albite Quartz Barite Estatite Hyperthene	Fe-chlorite Mg-Fe chlorite Epidote
179726	Rhyolite	Few grains of individual disseminated quartz. Chlorite patches after pyroxene. Strongly altered phenocrysts in the fine-grained matrix groundmass. Fragments of altered K-feldspar (microcline?)	Quartz Chlorite Muscovite Pyroxene	Fe-ilmenite Apatite Hornblende K-feldspars	Margarite?
179766	Basalt	Chlorite patches after pyroxene? Actinolite altered showing needle-like	Chlorite? Actinolite? Pyroxene?	Chlorite Calcite Albite Hornblende	Mg-chlorite

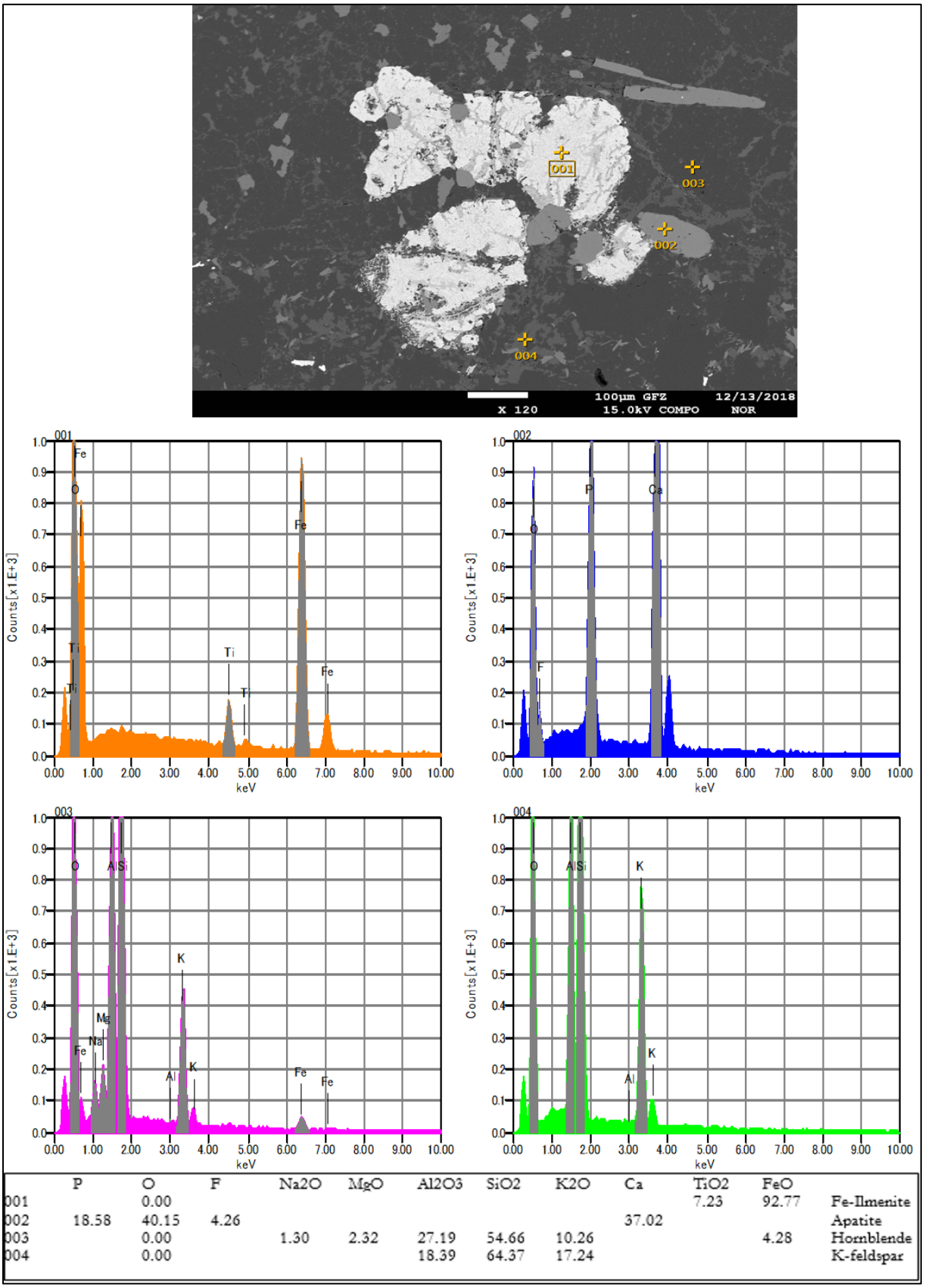

	P	O	F	Na2O	MgO	Al2O3	SiO2	K2O	Ca	TiO2	FeO	
001		0.00								7.23	92.77	Fe-Ilmenite
002	18.58	40.15	4.26						37.02			Apatite
003		0.00		1.30	2.32	27.19	54.66	10.26			4.28	Hornblende
004		0.00				18.39	64.37	17.24				K-feldspar

Figure 3-9: Mineral identification using JEOL EDS System (sample/slide 179726). Top image: minerals in the slides as observed by the instrument. Middle graphs: chemical composition of the measured slide at every location (spot) as shown in the image above. Down: table containing concentration of the measured elements with the interpreted minerals. Interpretation for the remaining 4 samples are found in Appendix 4 of this report.

3.6. Mineral classes

To obtain a mineral map, first, the decision trees of both SWIR and LWIR images were constructed based on the minerals identified. For SWIR images, the decision tree constructed by Van Ruitenbeek et al. (2017) was adopted in this study and edited to accommodate minerals with shifted absorption features due to mixtures. Wavelength maps of 2100 – 2400nm having six bands of the 1st, 2nd and 3rd deepest absorption features with their corresponding depth bands were used as input to the decision tree. The depth band of the deepest absorption features was used once at the beginning of the decision tree to mask out the background values of the samples while most of the minerals were classified using wavelength position of the 1st and 2nd deepest absorption features. Wavelength position of the 3rd deepest absorption features was used only once to differentiate illite and muscovite from calcium-rich mica (margarite) which have the same wavelength position of the 1st and 2nd absorption features. Also, a wavelength range of the deepest absorption features of 1530 – 1570 nm (epidote feature) was also used to differentiate epidote from chlorite. The resulting image is a mineral map showing mineral classes with epidote and chlorite being dominant minerals as they appear in many samples. Generally, all identified SWIR minerals were classified by the decision tree, and those samples with a dark colour (unclassified) were the ones that contained either noisy spectra or minerals that cannot be identified in SWIR range.

For the LWIR images, the approach of using wavelengths used in constructing a decision tree in SWIR was also applied with the addition of the two wavelength positions: second and third features, created from the band depths information. The depth bands ratio of 1st feature to that of the 2nd feature found to be applicable in differentiating chlorite, actinolite and oligoclase from other minerals. Similarly, the depths band ratio of the 1st and 2nd features and that of the 2nd and 3rd features have also been used to differentiate chlorite further from other minerals having overlapping features. However, one of the challenges observed during the determination of mineral classes in LWIR using decision tree is that most of the spectra contained too many features which do not relate to the diagnostic features of the mineral. These features caused difficulties in defining the wavelength position of the particular mineral class. To solve this problem, the small features were also incorporated during decision tree construction by using "AND" and "OR" Boolean operators. The boolean expressions used to construct decision trees for both, SWIR and LWIR are found in Appendix 1 of this report.

The resulted classified image shows that quartz, plagioclase, amphibole and epidote are the most abundant minerals as they appear in most of the samples. The unclassified areas in the samples may be due to the samples containing non-detectable LWIR minerals, or due to over-filtering which may remove some spectral information. The decision tree mineral class images of both, SWIR and LWIR, are found in Appendix 2 of this report.

3.7. Spectral mineral abundances

Mineral abundances were determined by creating a region of interest (ROI) from each classified sample. The fraction of the pixels highlighted by each mineral in a particular sample was calculated from both SWIR and LWIR classes. Table 3-4 below shows the percentage of the mineral coverage of the identified minerals from SWIR, LWIR and XRD calculated from the 20 selected samples for comparison. The results show there is a consistency in mineral identified from both the SWIR, LWIR and XRD but the methods differ in mineral abundances. The variation in mineral abundances may depend on which mineral is more detectable to which method even in small amounts. For example, chlorite is more detectable in SWIR than in the other methods and can even be quantitatively be subdivided into three types namely: Mg-rich, Fe-rich and intermediate (Mg-Fe rich) chlorite. Furthermore, the abundance of the pyrophyllite value in sample 179897 is higher in SWIR and LWIR but less in XRD. However, in XRD, this sample shows quartz as an abundant mineral. Observations from the hand specimen show this sample is highly silicified and hence rich in quartz. Therefore, the high amount of pyrophyllite as indicated by SWIR and LWIR implies that pyrophyllite is detected more easily by these two methods than XRD, and vice-versa for the quartz. The abundances for all rock samples in both SWIR and LWIR are found in Appendix 3 of this report.

.

Table 3-4: Spectral mineral analysis (quantification, observation and interpretation) for 20 selected rock samples

No	Sample no.	Rock type	Quantified Spectra minerals (%)		XRD analysis	Observation
			SWIR	LWIR		SWIR, LWIR and XRD
1	179897	Rhyolite	Pyrophyllite 96 Unclassified 4	Pyrophyllite 81 Quartz 3 Unclassified 16	Quartz 81 Pyrophyllite 19	• Quartz is the most dominant mineral in the sample as detected in XRD. • Pyrophyllite is present in small fraction but detected easily in both SWIR and LWIR. • Quarz and Pyrophyllite spectra look similar spectra shape in LWIR
2	179890	Basalt	Epidote 89 Mg-Chlorite 0.8 Mg-Fe chlorite 0.2 Unclassified 10	Epidote 20 Quartz 8 Albite 1 Hornblende 1 Chlorite 1 Actinolite 0.3 Unclassified 69	Epidote 26 Quartz 22 Clinozoisite 17 Albite 16 Fluoro-ferri-magnesiokatophorite 12 Actinolite 8	• Epidote is dominated in the sample and showed consistency abundances in LWIR and XRD. • Epidote has the deepest feature around 9.2µm instead of 10.4µ in LWIR due to a mixture of Quartz, plagioclase and amphiboles • LWIR and XRD showed consistency in mineral identification
3	179896	Dacite	Prehnite 72 Epidote 25 Illite/Musc 0.4 Margarite 0.2 Unclassified 2	Quartz 57 Plagioclase 11 Epidote 9 Illite/Musc 4 Unclassified 19	Quartz 37 Albite 27 Epidote 18 Phengite 12 Prehnite 6	• Quartz and plagioclase are the most abundant minerals. • SWIR spectra showed mixed spectra of epidote and prehnite. • The abundance of epidote in SWIR is because of the absorption feature around 1.55µm used to map it.
4	176768	Basalt	Mg-Chlorite 45 Actn/Honb 26 Epidote 3 Unclasified 27	Actinolite 61 Plagioclase 21 Hornblende 1 Epidote 0.2 Unclassified 16	Albite 30 Enstatite 26 Magnesiohornblende 21 Actinolite 17 Chlorite 5	• Magnesium rich hornblende dominate in both SWIR and LWIR images. • Hornblende/Actinolite spectra in LWIR is mixed with plagioclase (Oligoclase). • Pyroxene has less responses in LWIR than in XRD as compared to Amphiboles and plagioclase.
5	176798	Basalt	Margarite 93 Illite/musc 0.2 Unclassified 6	Quartz 71 Illite 7 Plagioclase 5	Clay fraction 38 Albite 18 Enstatite 18	• Mica (calcium rich?) is highly detectable in SWIR and XRD and is dominant mineral in this sample.

No	Sample no.	Rock type	Quantified Spectra minerals (%)		XRD analysis	Observation
			SWIR	LWIR		SWIR, LWIR and XRD
				Epidote 1 Unclassified 16	Quartz 17 Muscovite 6 Chlorite 4	• Quartz and plagioclase are most detectable in LWIR as compared to Mica.
6	179899	Rhyolite	Clay fraction 97 Unclassified 3	Quartz 38 Plagioclase 26 Illite/Musc 10 Cordierite 6 Chlorite 1 Unclassified 19	Clay fraction 57 Quartz 27 Albite 15	• Correlation in the identification of Illite/muscovite (white Mica) from all methods despite the abundances. • The difference in abundances depends on which mineral is detectable to which method, i.e. Mica and Quartz are more detectable to SWIR and LWIR respectively.
7	179871	Rhyolite	Illite/musc 72 Prehnite 5 Margarite 1 Unclassified 21	Quartz 52 Illite/Musc 20 Plagioclase 9 Unclassified 18	Muscovite 42 Quartz 31 Albite 27	• Same as no 6.
8	176754	Basalt	Fe-Chlorite 81 Unclassified 19	Quartz 87 Illite/Musc 1 Epidote 1 Unclassified 11	Quartz 73 Calcite 14 Chamosite 14	• Fe-rich chlorite is most detectable in SWIR and is dominant mineral in this sample. • Quartz is most detectable in LWIR and XRD. • The whole sample shows two dominant minerals, Fe-Chlorite in SWIR and quartz in LWIR. • No spectrum related to calcite was observed in both SWIR and LWIR.
9	176753	Basalt	Epidote 45 Mg-Chlorite 29 Mg-Fe Chlorite 3 Unclassified 23	Plagioclase 43 Actinolite 20 Pyroxene 9 Epidote 2 Staurolite 0.3 Unclassified 26	Albite 41 Cordierite 18 Quartz 13 Actinolite 11 Epidote 9 Chlorite 7	• The spectra in SWIR are more of chlorite and epidote mixtures and seems to dominate in the whole sample. • Spectra in LWIR are the mixtures of quartz and plagioclase. • It is difficult to differentiate pyroxene and cordierite in the mixed spectra of LWIR. Therefore, cordierite can probably be pyroxene.
10	176776	No data	Epidote 31 Mg-Chlorite 20 Mg-Fe Chlorite 14 Prehnite 6	Quartz 31 Plagioclase 11 Illite/Musc 5 Pyroxene 1	Albite 47 Quartz 38 Epidote 9 Muscovite 6	• Chlorite with minor epidote and prehnite observed in SWIR spectra.

No	Sample no.	Rock type	Quantified Spectra minerals (%)		XRD analysis	Observation
			SWIR	LWIR		SWIR, LWIR and XRD
			Unclassified 29	Actinolite 1 Epidote 1 Unclassified 50		• White Micas were not identified in SWIR probably due to the presence of chlorite which is more detectable in SWIR than white micas.
11	176730	No data	Mg-Chlorite 41 Actin/hornb 1 Epidote 0.1 Unclassified 58	Chlorite 48 Plagioclase 10 Actinolite 3 Epidote 02	Actinolite 31 Antigorite-T 27 Hornblende 25 Chlorite 11 Magnesioferrite 6	• SWIR image is too dark, and the spectra are too noisy; hence the SWIR interpretation of this sample is uncertain. • LWIR shows chlorite is dominated the whole sample.
12	176740	No data	Mg-Chlorite 40 Epidote 9 Mg-Fe Chlorite 1 Fe-Chlorite 0.2 Unclassified 50	Pyroxene 19 Plagioclase 15 Epidote 7 Quartz 2 Chlorite 2	Albite 31 Diopside 22 Epidote 16 Jadeite 13 Quartz 12 Chlorite 6	• Pyroxene is more detectable in LWIR than plagioclase while it's vice versa in XRD. Therefore, it is difficult to determine which one is abundant. • Spectra in SWIR are too noisy; hence the interpreted minerals are uncertain. • Difficult to differentiate pyroxene with mixed epidote spectra.
13	176749	No data	Mg-Chlorite 38 Actinolite 22 Epidote 0.1 Unclassified 40	Quartz 34 Pyroxene 13 Epidote 2 Chlorite 2 Plagioclase 1 Unclassified 46	Oligoclase 34 Enstatite 34 Epidote 16 Fluoromagnesiok aphorite 8 Quartz 8	• No good match was obtained in SWIR spectra. • Pyroxene spectra of LWIR dominated the whole sample.
14	176752	Basalt	Mg-Chlorite 64 Epidote 6 Actinolite 0.2 Unclassified 30	Plagioclase 69 Actinolite 18 Epidote 1 Unclassified 12	Albite 30 Oligoclase 28 Enstatite 17 Actinolite 13 Potas.chlorohasti ngsite 11	• Amphiboles and plagioclase are the most dominant spectra in both SWIR and LWIR respectively. • Actinolite and some types of chlorite appear to have the same wavelength positions of absorption features, hence may confuse classification in the decision tree.
15	180211	Basalt	Epidote 57 Mg-Fe Chlorite 24 Mg-Chlorite 11	Plagioclase 66 Quartz 4 Actinolite 0.4	Albite 43 Oligoclase 42 Epidote 8	• Plagioclase is the most dominant mineral in this sample and quartz are very low. • SWIR image showed mixed spectra of epidote and chlorite.

No	Sample no.	Rock type	Quantified Spectra minerals (%)		XRD analysis	Observation
			SWIR	LWIR		SWIR, LWIR and XRD
			Fe-Chlorite 0.3 Unclassified 7	Epidote 0.2 Chlorite 0.2	Quartz 7	
16	179759	Komatiite	Mg-Chlorite 5 Mg-Fe Chlorite 2 Epidote 1 Unclassified 92	Quartz 23 Plagioclase 21 Epidote 7 Cordierite 4 Actinolite 3 Illite/Musc 1 Pyroxene 0.2 Unclassified 41	Albite 30 Hornblende 19 Potassic-chlorohastingsite 16 Actinolite 16 Quartz 12	• No spectral match in SWIR, hence all classified minerals are uncertain • LWIR spectra are completely mixed up with more than two minerals, probably quartz plagioclase and epidote. Hence it is difficult to determine the wavelength position of the mineral features. • Interpretation relies more on XRD results where plagioclase and amphiboles dominate.
17	179757	Komatiite	Mg-Chlorite 57 Actin/hornb 13 Unclassified 30	Chlorite 74 Plagioclase 4 Actinolite 1 Unclassified 20	Antigorite-Talc 29 Hornblende 23 Actinolite 21 Enstatite 14 Chlorite 13	• No spectral match in SWIR hence all classified minerals are uncertain • In LWIR image, chlorite spectra observed throughout the sample, hence other classified minerals are uncertain. • Interpretation relies on LWIR and XRD results. • The sample is rich in hornblende as per XRD results • Chlorite may be abundant in the sample but is less detectable in XRD.
18	179821	Basalt	Mg-Chlorite 66 Epidote 20 Unclassified 14	Hornblende 65 Epidote 11 Actinolite 1 Unclassified 23	Actinolite 33 Hornblende 31 Epidote 22 Enstatite 14	• Both SWIR and LWIR images showed actinolite/hornblende spectra throughout the sample • The sample is rich in hornblende as per XRD results • The other minerals may be present in a small amount or due to overlapping features.
19	179823	Basalt	Epidote 87 Mg-Chlorite 8 Mg-Fe Chlorite 1 Unclassified 4	Epidote 15 Quartz 5 Illite/Musc 4 Plagioclase 2 Cordierite 2 Actinolite 1 Unclassified 71	Quartz 24 Epidote 21 Clinozoisite 19 Actinolite 14 Enstatite 13 Cordierite 9	• Epidote is dominant minerals as it outstands high in both SWIR and LWIR. • The difference in the abundance of epidote is due to the presence of the other detectable minerals in LWIR. • Quartz is more detectable in XRD than epidote.

No	Sample no.	Rock type	Quantified Spectra minerals (%)		XRD analysis	Observation
			SWIR	LWIR		SWIR, LWIR and XRD
20	179799	Basalt	Epidote 76 Mg-Chlorite 16 Mg-Fe Chlorite 1 Unclassified 7	Plagioclase 41 Actinolite 18 Epidote 3 Unclassified 38	Oligoclase 34 Albite 33 Epidote 18 Amphiboles 9 Chlorite 5	• A mixture of chlorite and epidote in SWIR observed throughout the sample. • Plagioclase is the most abundant mineral in the sample as classified by LWIR and XRD.

4. DATA INTEGRATION AND DISCUSSION

This chapter discusses the results of the mineral identification methods presented in chapter three. The similarities and differences of the mineral identification results, based on the type of method used, are discussed in detail. Furthermore, the results from spectroscopy, XRD and thin section are integrated to define metamorphic mineral assemblages. For the assessment of the dominant control of metamorphic mineral assemblages, spectroscopic results are integrated with geochemical data of the same rock sample provided by Smithies et al. (2007). The metamorphic facies are then interpreted from the spectrally determined metamorphic mineral assemblages and the assessed influence of metamorphic mineral assemblages. The relationship between metamorphic grade and wavelength position of Mg-OH absorption is also discussed. Finally, the results of this study are compared with the previous study by Abweny et al. (2016). A total of 202 rock samples out of 237 processed in this research were found in the geochemical database of Smithies et al. (2007). Among the 202 samples, 12 rock samples were reported by Abweny et al. (2016) as the hydrothermally altered sample. These hydrothermally altered samples (assemblage P in Appendix 3) were excluded from analysis in this study because they were not of the interest of the study.

4.1. Mineral identification methods

The previous study by Abweny et al. (2016) demonstrated the effectiveness of the use of an ASD spectrometer in identifying metamorphic minerals from rocks of varying lithological composition. In this study, minerals such as epidote, actinolite, hornblende, illite, muscovite, pyrophyllite and chlorite of varying composition were identified. However, the ASD data acquisition technique (by using a point measurement) made it difficult to accurately estimate mineral compositions in the rock sample. In this study hyperspectral images of rock samples acquired from both SWIR and LWIR wavelength range were used to estimate the composition and abundances of minerals present in the samples. For validation, an XRD and petrographic study of thin sections were used.

The results from hyperspectral imaging techniques such as SWIR and LWIR show similarity in mineral identified. Most of the minerals identified in SWIR could also be identified in LWIR except for two minerals, margarite and prehnite which could not be identified in LWIR. Similarly, when compared with XRD and thin section results, we found to have a correlation in mineral identification among the four methods. However, the difference of the four methods namely; SWIR, LWIR, XRD and thin section was in the number of minerals identified by each method per sample. As it has been shown in Table 3-4 above, the number of minerals identified by LWIR is relatively higher than SWIR in all rock samples. This difference can be explained by looking at the techniques used by the two methods on identifying minerals. The identification of minerals by SWIR is due to vibration of the molecular bonds such as OH, Al-OH, Fe-OH, Mg-OH and CO^{-}, while LWIR is due to the stretching vibration of Si – O (reststrahlen bands) and the CO^{-} bond. The Si – O bond exists in a large number of minerals and hence could be a reason of why minerals in SWIR range can also have a feature in LWIR range. The number of minerals identified by XRD is more similar to that identified by LWIR. Although the samples used to make thin sections were not included in LWIR samples scan, their identified minerals related more to that identified by LWIR and XRD.

In addition, this study has found that there is a difference in mineral abundances in each sample if compared between the three methods: SWIR, LWIR and XRD (Table 3-4). The difference in mineral abundances among the three methods is firstly, due to the difference in spatial resolution of SWIR (256 μm) and LWIR (400 μm) images, and secondly, depends on the ability of the method to detect a particular mineral. For example, sample number 179890 in Table 3-4 shows epidote which can be more easily detected in SWIR than in LWIR and XRD. Similarly, the data of sample number 176768 indicate that Mg-chlorite is more detectable in SWIR, actinolite in LWIR and albite in XRD. Furthermore, the data of sample 179897 in Table 3-4 showed that the pyrophyllite mineral gives higher abundances in SWIR but lower abundances in LWIR and XRD. From visual observation with hand lens, sample 179897 is described as strongly silicified fine grained felsic rock, and that is the reason why LWIR and XRD gave a high abundance of quartz. Quartz

has a very low response in SWIR range when compared to pyrophyllite. Therefore, determination of mineral abundances in a rock sample depends on which mineral has a higher response to a particular method.

To extend the findings on the difference of mineral abundances, the number of crystal lattices of a mineral was accounted for. A crystal lattice refers to the arrangement of atoms or group of atoms in the structure of a mineral. The mineral abundance from the four methods mentioned in the previous paragraph is strongly influenced by the crystal structure of a particular mineral. When compared with SWIR, XRD works well for the minerals with high crystallinity. In sample 176740 in Table 3-4 for instance, chlorite abundance is higher in SWIR than in XRD. This implies that chlorite in this sample is less crystalline. In petrographic study, one of the criteria used to identify minerals under an optical microscope is by looking at the crystal form of the minerals. Therefore, the influence of crystal lattice in XRD and thin section is higher than in SWIR and LWIR.

The difference in the number of identified minerals and the mineral abundances may give information on the strength and weakness of each method. As it was discussed above, both SWIR and LWIR are effective on the fundamental vibration of the molecular bonds in a particular mineral but differ in the types of bonds. SWIR was observed to be more effective on the minerals having a metal-OH bond in their molecular structure such as chlorite, epidote, prehnite, etc., while LWIR is more effective on silicate minerals having a Si – O bond such as albite, oligoclase, quartz and pyroxenes. In XRD it depends on the crystallinity of the mineral, which is contrary to SWIR method which is not affected by the crystal structure of the minerals. An optical microscope can be used to identify a wide range of minerals, but it is difficult to use in the case of strongly altered minerals and amorphous minerals.

4.2. Interpretation of metamorphic mineral assemblages

Metamorphic mineral assemblages of each sample were obtained from the calculated mineral abundances of SWIR and LWIR by picking minerals with high percentage values. Mathematically, it was difficult to combine SWIR and LWIR and calculate mineral abundances due to their different spatial resolution. The combination was made relatively by comparing mineral abundances from SWIR and LWIR for each sample. The abundant minerals in each sample were grouped to form an assemblage. The defined mineral assemblages were further compared with results of XRD and petrographic study as well as visual observation of each sample for validation.

From the integration of all these methods, 12 metamorphic mineral assemblages were defined from 190 classified rock samples (Table 4-1). Some rock samples are dominated by one type of mineral, hence were assigned as the assemblage of that particular mineral. Assemblage E and F are good examples of the assemblages containing only one type of mineral which is Mg-chlorite and epidote respectively. Plagioclase (albite/oligoclase) and quartz are observed to occur in most of the samples. In places where a plus or minus sign (±) was given, it implies the later mineral(s) was observed in small abundance. While the assemblage G was assigned to samples abundant in plagioclase and quartz. Appendix 3 shows a combination of SWIR and LWIR abundances and the defined metamorphic mineral assemblages for each rock sample.

Table 4-1: Quantified metamorphic mineral assemblages

No	Code	Measured metamorphic mineral assemblages (with number of samples in brackets)
1	A	Mg-chlorite, Hornblende (9)
2	B	Mg-chlorite, Epidote, Hornblende ± Plagioclase (8)
3	C	Mg-chlorite, Actinolite ± Hornblende, Plagioclase (23)
4	D	Mg-chlorite, Epidote, Actinolite ± Plagioclase (26)
5	E	Mg-chlorite ± Plagioclase, Quartz (7)
6	F	Epidote ± Plagioclase, Quartz (18)
7	G	Plagioclase, Quartz (7)
8	H	Fe-chlorite ± Plagioclase, Quartz, Mg-chlorite (23)
9	K	Mg-chlorite, Epidote ± Plagioclase, Quartz (39)
10	L	Epidote, Mg-Fe chlorite ± Plagioclase, Quartz (10)
11	M	Mg-chlorite, Epidote, Pyroxenes ± Plagioclase, Quartz (12)
12	N	Prehnite, Epidote ± Plagioclase, Quartz (8)

4.3. Assessing dominant control of metamorphic mineral assemblages

For the assessment of the dominant control of metamorphic mineral assemblages, geochemical data produced by Smithies et al., (2007) was used to compare to the spectrally determined mineral assemblages. The lithological composition of the volcanic rocks represented by the index of the major elements expressed as oxides and spectral mineral abundances represented by the wavelength position of the Mg-OH absorption of single ASD spectra were plotted on an XY scatter plot (Figure 4-1). The scatter plot was adopted from the study of Abweny et al. (2016) who found that it is possible to discriminate metamorphic mineral assemblages by relating the wavelength position against the lithological index. Abweny et al. (2016) found that the wavelength positions of the main MgOH absorption features of the minerals measured by ASD have relation to metamorphic mineral assemblages. He used MgOH absorptions because lithologically, the rock samples from the study area are dominated by mafic composition with less intermediate and felsic units. MgOH absorption feature present in all samples contrary to AlOH and FeOH absorption which were found in a few samples. The quantified metamorphic mineral assemblages in Table 4-1 above were plotted in the scatter plot (Figure 4-1), and the related assemblages were assigned the same colour. For example, assemblage K, D and M were assigned one colour because Mg-chlorite and epidote intersect in all three assemblages. Similarly, assemblage A, B and C because of the intersection of Mg-chlorite and hornblende, while the remaining assemblages were given individual colours.

From Figure 4-1, as described below, that there are more variations in the mineral assemblages along the wavelength position than along the lithological index. For example, assemblage A, B and C as coloured red which is rich in hornblende dominate at a wavelength range of 2315 – 2330 nm represented by wavelength region A1. The wavelength range A2 (2330 – 2345 nm) is dominated by the assemblages K, D, M (yellow) and E, F (green), while the wavelength range A3 (2345 – 2360 nm) is mostly dominated by Fe–chlorite. Assemblage L comprising Mg-Fe chlorite (intermediate chlorite) and epidote is observed around the wavelength range of 2340 – 2350 nm, which is in contact with Mg-chlorite in the wavelength region A2 and Fe-chlorite in wavelength region A3. Assemblage N, mainly prehnite and epidote is between the wavelength region A2 and A3, which is the same as assemblage L but restricted only in one area. Mg-chlorite and epidote for assemblage E and F respectively dominated in wavelength region A2 with less in A1, and none in A3. Although plagioclase and quartz in assemblage G appeared in many samples and is distributed everywhere within the plot area, assemblage G still shows to vary along Mg-OH absorptions as they are more in wavelength region A2, and less in A1 and A3. Pyroxene, as assigned in assemblage M with Mg-chlorite and epidote, observed to exist in two wavelength regions, A1 and A2 but none in A3. The variation of mineral assemblages along the wavelength position of the Mg-OH absorption feature is temperature and pressure (P-T) dependant (and thus relates to the metamorphic grade). Variation of chlorite along the wavelength position of the main Mg-OH absorption features from Mg-chlorite in wavelength region A1 and A2 to Fe-chlorite in wavelength region A3 indicates that the formation of chlorite is also P-T dependent.

Along the lithological index in Figure 4-1, there is no significant variation of the metamorphic mineral assemblages. The little variation of the mineralogy along the lithological index depends on the chemistry of the rock type (and thus related to the protolith). For example, prehnite (assemblage N) which is found only in dacitic rock is due to the chemical composition of the dacite which is of intermediate composition, with a high content of silica. On the other hand, minerals like chlorite and epidote are due to the mafic composition of the rock such as magnesium and iron and hence are dominant mainly in mafic rocks. Furthermore, the assemblage A, B and C occur only in basalt – komatiite rocks which are of mafic-ultramafic composition. So, all this means that along the lithological index the mineral variation is due to the nature of the precursor rock. However, this variation is not so significant because some mineral assemblages can occur in a wide range of rock units, for example, assemblage K, F, L and H in Figure 4-1 occurred in three different rock unit namely; dacite, andesite and basalt/komatiite basalt, which cause difficult to assess variation of mineral assemblages because there are no changes in mineral assemblages in these three rock units along lithological index.

To further assess how metamorphic mineral assemblages vary with lithology types, a total alkali-silica (TAS) diagram was used to relate the measured spectral mineral assemblages to the proportions of combined alkalis (Na_2O+K_2O) and silica (SiO_2) contents. The TAS diagram was found to be useful in classifying low grade metamorphosed volcanic rocks because of the finely crystalized volcanic rocks which make it difficult to classify them by their mineralogy. Another reason is, in low-grade metamorphism, element mobility is

limited, therefore, the oxides of the major elements are used in classifying different rock units of the low-grade metamorphic volcanics (Ghatak et al. 2012; Sabine et al. 1985). The results in Figure 4-2 below shows the random distribution of the mineral assemblages with TAS contents. The mineral assemblages plot on the different lithological units based on the chemical composition of the rock similar to that of lithological index versus Mg-OH absorption in Figure 4-1. The difference is, there are no apparent patterns of the mineral assemblages in the TAS diagram.

In a comparison of the two figures (Figure 4-1 and Figure 4-2), it is seen that the mineral assemblages vary with wavelength position of the main Mg-OH absorptions in Figure 4-1 rather than lithological types of the precursor rock, while in Figure 4-2, the assemblages were plotted in the protolith of which they belong. The variation of mineral assemblages along the spectral parameters is P-T dependence and along the lithological index is depending on the chemistry of the precursor rock. Therefore, from these two figures, it can be concluded that the metamorphic mineral assemblages are dominantly controlled by metamorphic grade.

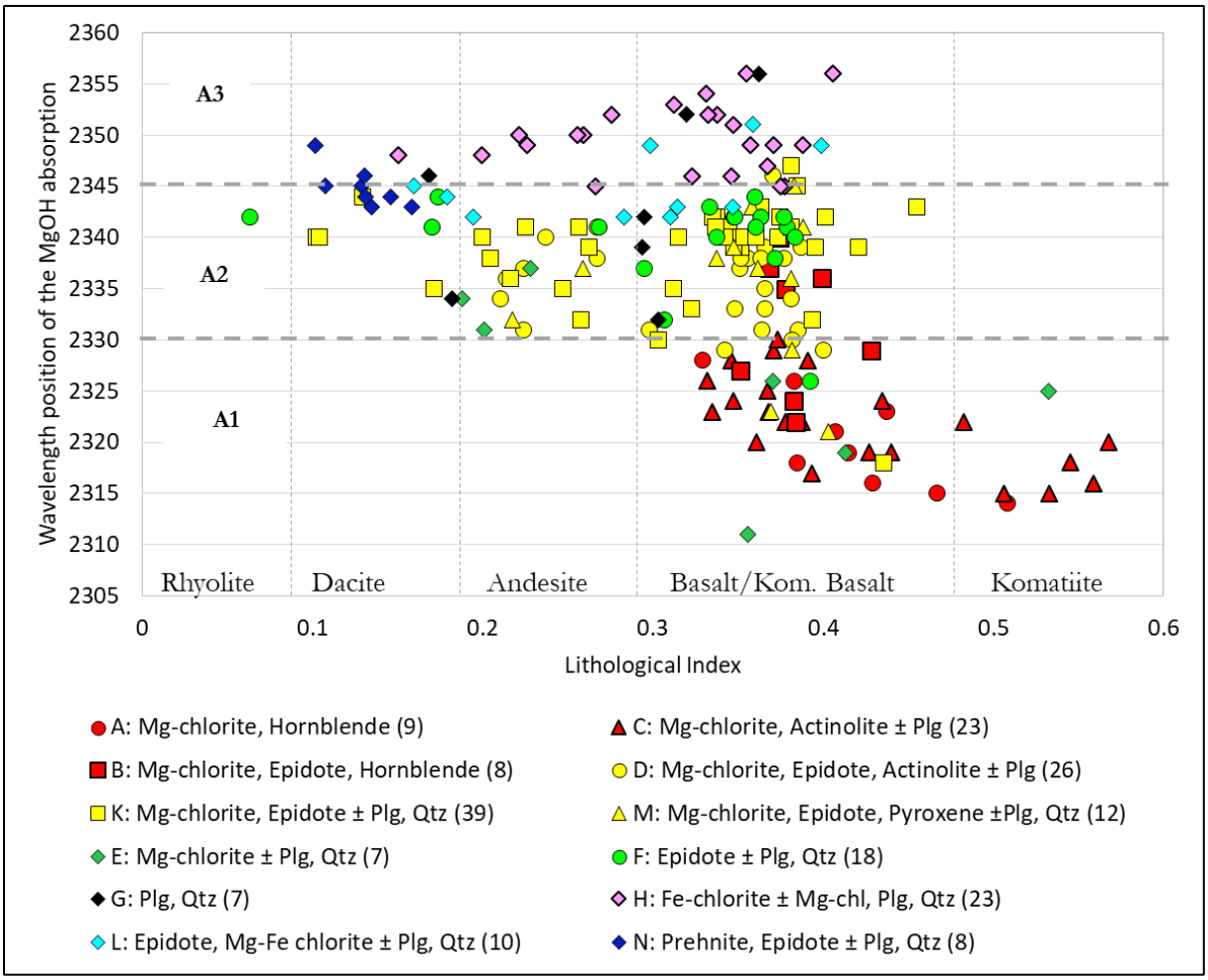

Figure 4-1: Scatter plot of samples showing the relationship between the lithological indexes the major elements expressed as oxides and the quantified spectral mineral assemblages presented as wavelength position of the main Mg-OH absorption features near 2335 nm measured by ASD. (Adopted from Abweny et al., 2016). Numbers at the end of each assemblage indicate number of samples in particular assemblage. A1, A2 and A3 are the wavelenth ranges for the major variation of the spectral mineral assemblages.

$$Lithological\ index = \frac{TiO2 + MgO + FeO + CaO}{TiO2 + MgO + FeO + CaO + K2O + SiO2}$$

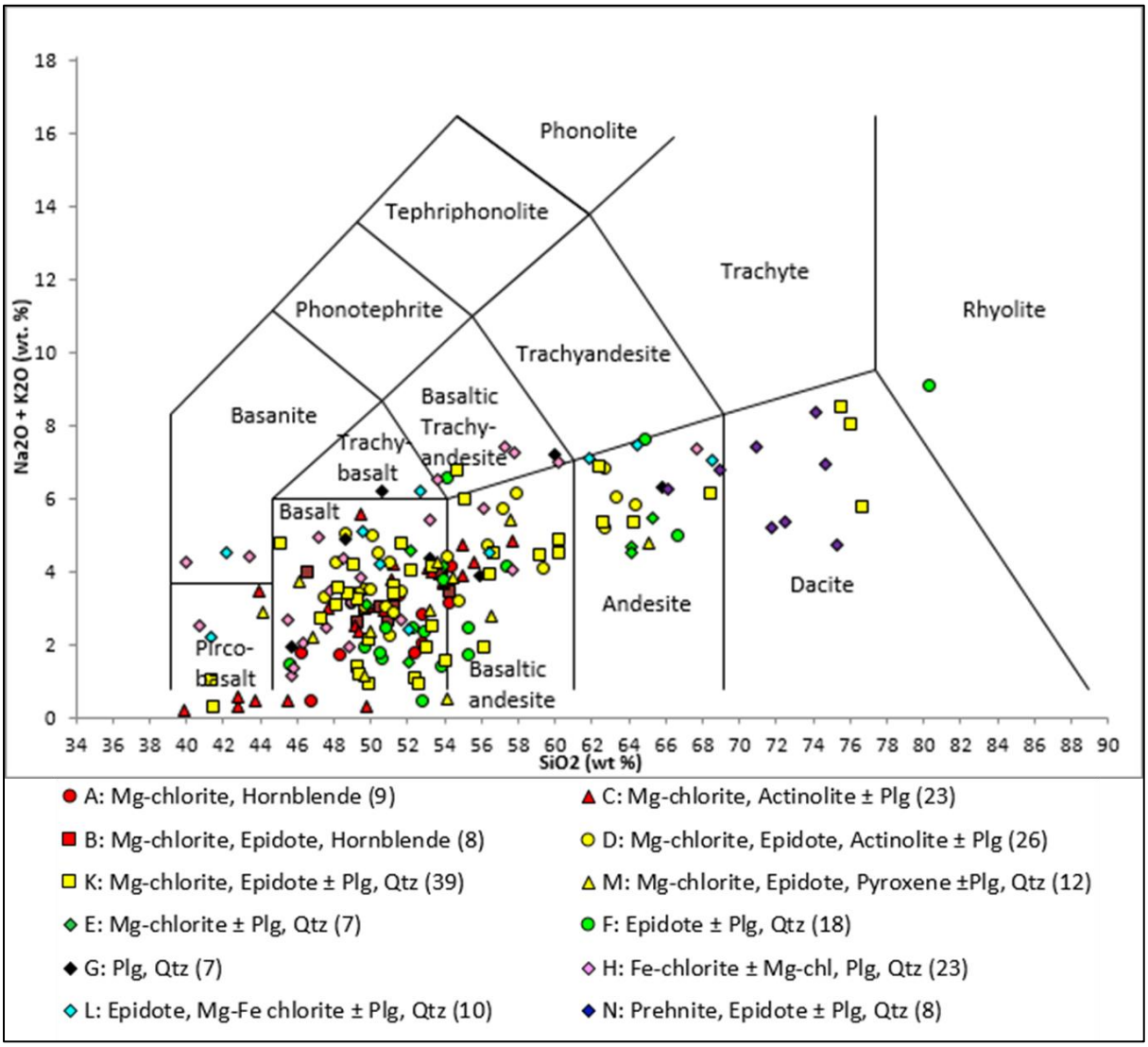

Figure 4-2: Total Alkali-Silica (TAS) diagram of the rock samples showing the relationship of the metamorphic mineral assemblages and different lithology.

4.4. Spatial variation of metamorphic mineral assemblages

As it was stated earlier, metamorphism in the study area increases with depth in the greenstone stratigraphic sequences and towards granitoid complexes. According to Van Kranendonk et al., (2002), the greenstone stratigraphy is bounded by sheared intrusive contacts with granitic complexes and unconformably overlying supercrustal rocks of the Fortescue Group and younger cover. Metamorphic grade of the greenstone rocks is characterised by the lower amphibolite facies from granitoid complexes to greenschist facies and prehnite-pumpellyite facies, to the very low metamorphic grade of the Fortescue Groups.

To verify the variation of the spectrally quantified mineral assemblages with metamorphic grade, each interpreted assemblage was overlain on the geological map of the study area by using the geographical location of the rock samples. The information such as geographical coordinates of the sample comes from, the name of the metamorphic belt, rock unit and rock name as described by Smithies et al. (2007) were used to compare the spectrally determined mineral assemblages spatially.

The results from Figure 4-3 below show there is a correlation between the spectrally determined mineral assemblages and the existing metamorphic grades of the study area. The assemblages A, B and C plots close to the contact with granitoid complexes, indicating lower amphibolite facies The three assemblages are rich in hornblende and the lower amphibolite facies, according to Smithies et al. (2007), is characterised by

hornblende. The rest of the assemblages (D to N) are observed to plot towards younger formation in which metamorphic grade decreases. The East Strelley Belt containing the Coonterunah and Euro Basalt Subgroups in Figure 4-4 have been zoomed in to illustrate the spatial variation of the spectral mineral assemblages within the metamorphic grade of the study area. The East Strelley Belt represents other tectonic units such as Marble Bar Belt, Mount Elsie Belt, Warralong Belt, Northwest Kelly Belt, McPhee Belt and Kelly Belt within the study area.

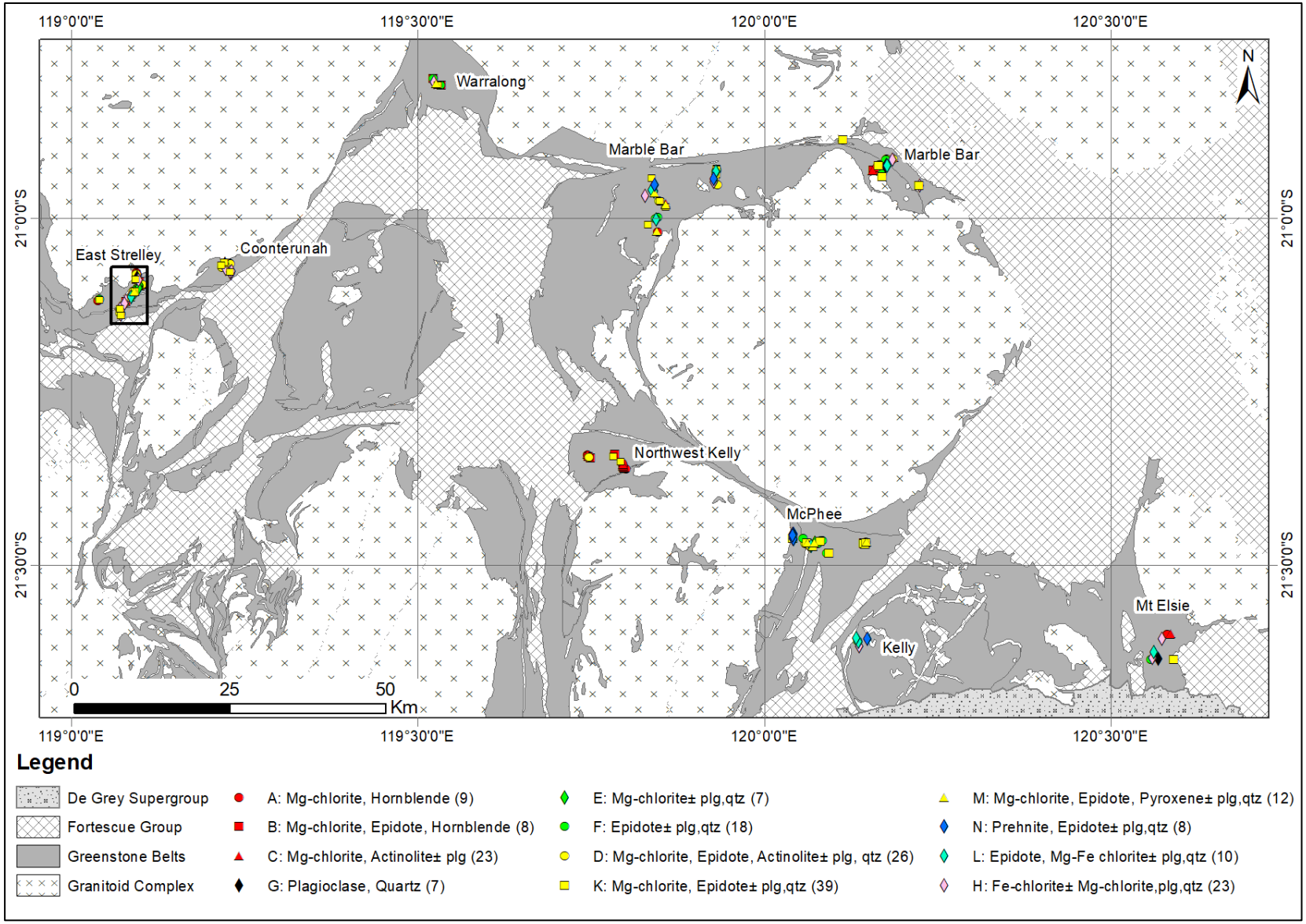

Figure 4-3: Generalized geological map of EP showing variation of metamorphic mineral assemblages (Data source: Geological Survey of Western Australia, 2019)

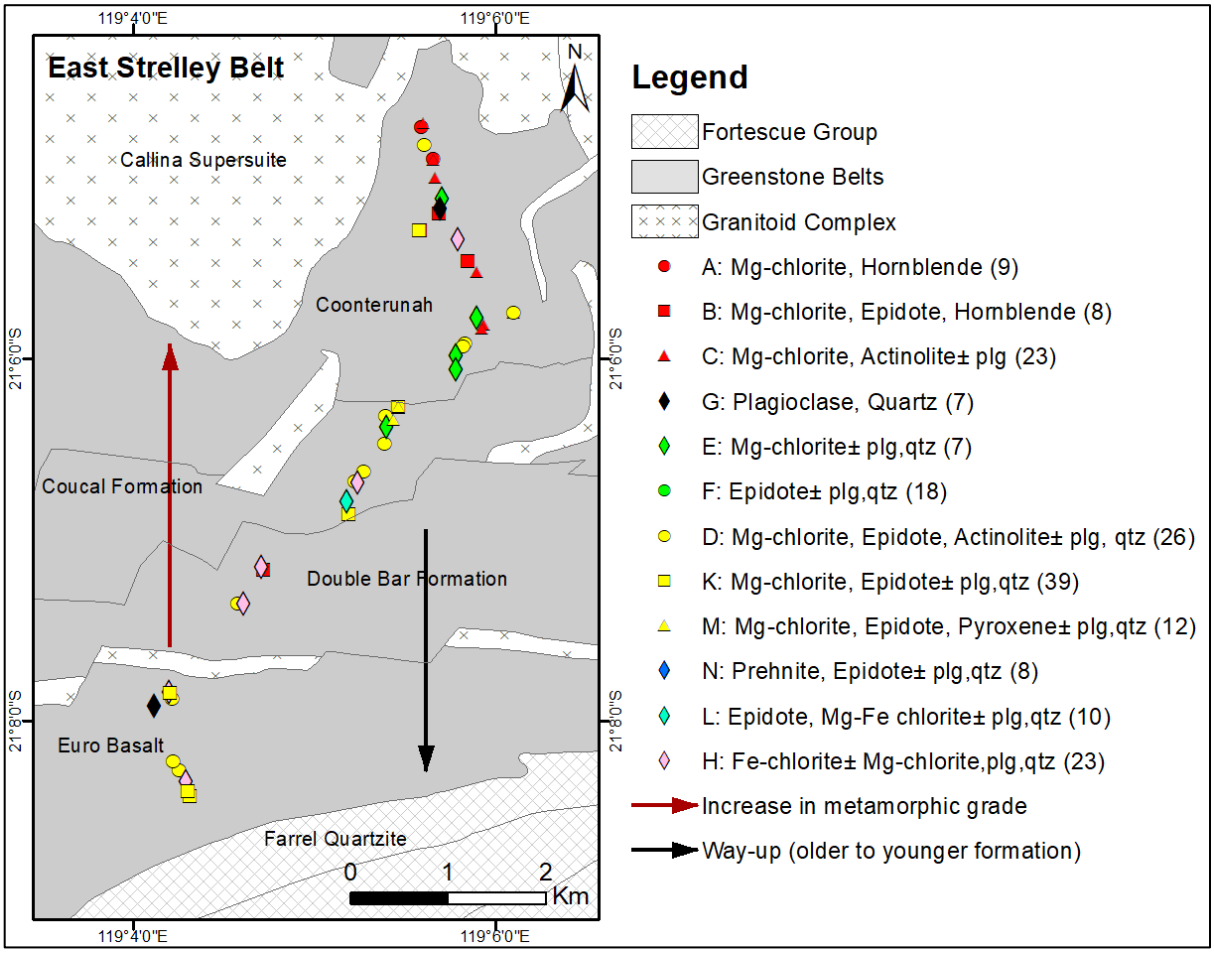

Figure 4-4: Zoomed geological map of East Strelley Belt showing variation of metamorphic mineral assemblages

4.5. Interpreting metamorphic grades and facies from spectral mineral assemblages

According to Bucher & Graps, (2011), in mafic rocks of metabasalts, the characteristic mineral assemblages of greenschist facies are plagioclase + chlorite + actinolite + epidote, and for amphibolite facies include plagioclase + hornblende ± biotite ± epidote (Figure 4-5). The grade of metamorphism increases from low-grade greenschist to intermediate grade amphibolite facies. Since most of the samples in this study are of mafic composition, the interpretation of metamorphic facies was made by comparing the spectral mineral assemblages defined above with the assemblages of Bucher & Graps, (2011).

Furthermore, we firstly, observed that spectral mineral assemblages vary with wavelength position of MgOH absorption features. And secondly, we observed that the spectral mineral assemblages vary with P-T across the stratigraphic sequence, from lower amphibolite facies associated with hornblende through greenschist facies to very low P-T of prehnite-pumpellyite facies. From the combination of these two observations, the relationship between the wavelength position of the MgOH absorption and the metamorphic facies was established based on the mineral abundances. The abundances of mineral assemblages from both SWIR and LWIR were plotted in the bar graph to quantitatively compare the mineral assemblages with the metamorphic facies (Figure 4-6). It is observed that assemblage A, B and C in wavelength region A1 relate more to the lower amphibolite facies. Since it was difficult to differentiate actinolite and hornblende in SWIR range as it was stated earlier, it is most probably that all actinolites in wavelength region A1 are hornblendes rich in magnesium. The XRD results for the samples selected from this region (e.g. sample 179823, 179757 and 176768) from the table above show hornblende as the dominant mineral. The presence of hornblende as a dominant mineral in the assemblage of hornblende, Mg-chlorite, actinolite and plagioclase place the wavelength region A1 into the lower amphibolite facies or greenschist-amphibolite

transition which is comparable to that of Bucher & Graps (2011). The lower amphibolite facies is formed at relatively low to intermediate P-T (metamorphic grade).

The assemblage D, E, F, H and M in wavelength region A2 relate more to the greenschist facies. Although assemblage G is observed almost everywhere but is dominating more in a region A2 of greenschist facies. The assemblages in wavelength region A3 are not clear whether they belong to greenschist or prehnite-pumpellyite facies. However, wavelength region A3 can be used to discriminate Fe-chlorite from Mg-chlorite with intermediate chlorite (Mg-Fe chlorite) in between as transition zone. This chlorite variation could be P-T dependence and hence there must be a P-T difference between wavelength region A2 and A3.

In addition, as mentioned earlier, Árkai & Sadek Ghabrial (1997) found that chlorite crystallinity can be used to estimate the metamorphic grade of low temperature meta-igneous rocks. The Fe-Mg bearing mineral is dominant in chlorite for most of the rock samples used in this research, similarly to the samples used by Árkai & Sadek Ghabrial (1997). And, it is observed in Figure 4-1 that Fe-chlorite is in almost same wavelength region (A3) as prehnite which formed in a very low temperature and hence is an indicator of very low-grade. From this relationship of Fe-chlorite and prehnite to occur at same wavelength region, this is evidence that Fe-chlorite is formed at a lower temperature when compared to Mg-chlorite. Therefore, Figure 4-6 summarizes the relationship between metamorphic grades and the wavelength position of the MgOH absorption.

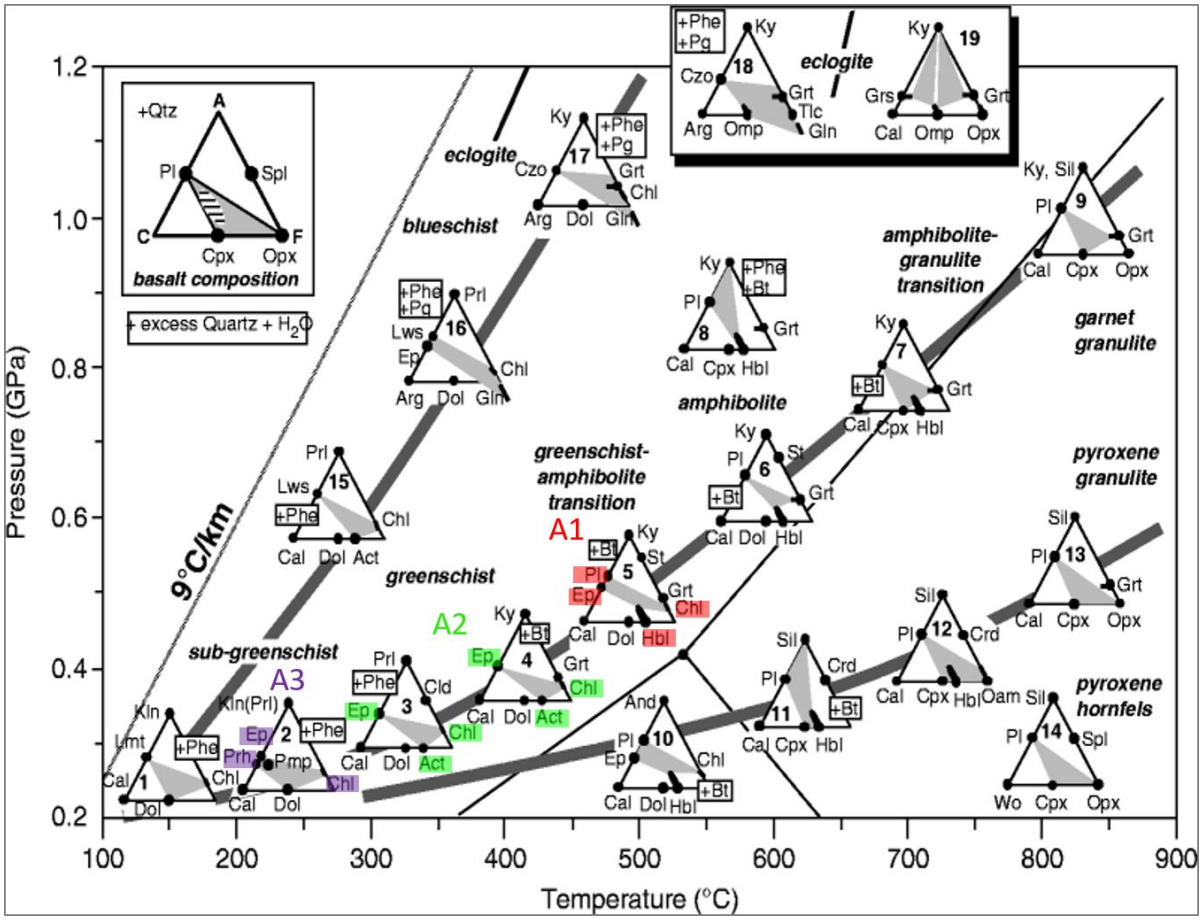

Figure 4-5: Metamorphism of mafic rocks (metabasalts) represented by ACF diagrams (after Bucher & Graps, 2011). The spectral mineral assemblages A, B and C in wavelength region A1 (red color) are comparable to that in triangle 5 which is lower amphibolite facies. Assemblages in triangle 3 ad 4 are comparable to spectral mineral assemblages D, E, F, K and M in wavelength region A2 (green colour) which is related to greenschist facies. And, assemblages in triangle 2 is comparable to spectral mineral assemblage N and most probably H in wavelength region A3 (purple colour) which is related to prehnite-pumpellyite facies.

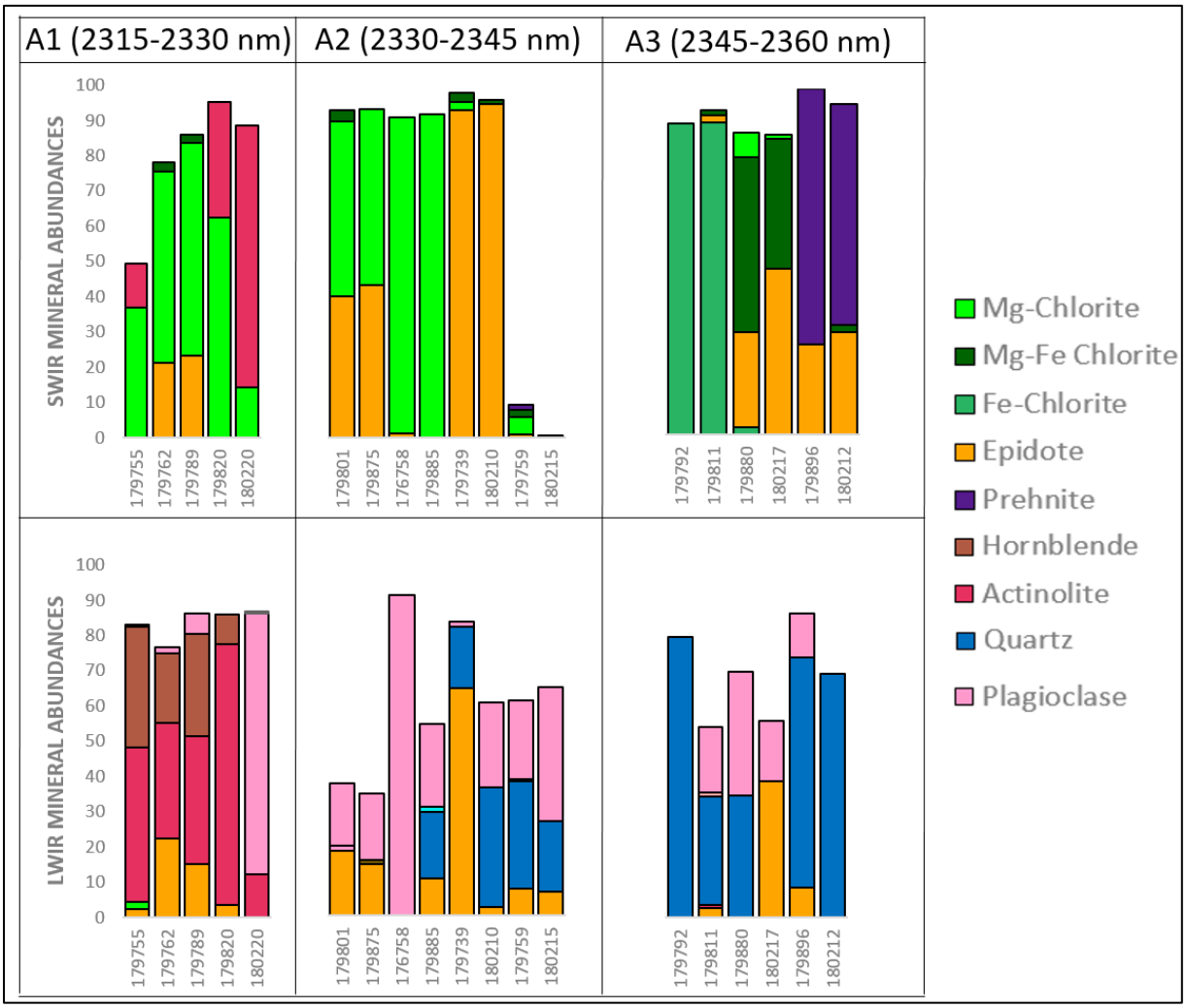

Figure 4-6: Bar graphs of spectral mineral assemblages as per wavelength ranges (A1, A2 and A3) from combination of SWIR and LWIR spectral mineral abundances.

4.6. Comparison of the spectral determined results with previous studies

As it has been stated earlier, Abweny et al. (2016) studied the same rock samples using an ASD Fieldspec3 and concluded that the metamorphic mineral assemblages are dominantly influenced by metamorphic grade. In his study, Abweny et al. (2016) used four dominant spectrally identified minerals namely actinolite, epidote, hornblende and chlorite of varying composition (Mg-chlorite, Fe-chlorite and intermediate chlorite) to conclude on metamorphic grade. On assessing the dominant control of metamorphic mineral assemblages, Abweny et al. (2016) defined four zones of mineral assemblages based on the mineral he identified. From high to low grade, he defined zone of (1) hornblende + Mg-chlorite, (2) intermediate chlorite + actinolite + hornblende, (3) intermediate chlorite + epidote and (4) Fe-chlorite. He also defines a subzone between zone 1 and 2 which he called the "transition zone".

In this study, 12 mineral assemblages were defined from all 237 rock samples which were subsequently grouped into three wavelength regions. The three wavelength regions summarize Abweny's interpreted zones, where wavelength region A1 is equivalent to zone 1 in Abwey's study, region A2 combines zone 2 and 3 while region A3 is same as zone 4 of Abweny et al. (2016). The difference in these two studies regarding their results is in the number of identified mineral assemblages. In this study, results consist of 12 sets of spectral mineral assemblages in contrast to the 4 spectral mineral assemblages (zones) from Abweny et al. (2016)'s study. This big difference is due to the method used by this study which is the combination of SWIR and LWIR hyperspectral imaging.

The use of SWIR and LWIR hyperspectral images in this study has advantages over the ASD point measurement method as used in the previous study by Abweny et al. (2016). The combination of SWIR and LWIR has enhanced the detection of a large number of minerals as compared to ASD. The two wavelength ranges of HI could be used to detect different types of minerals and make the number of identified minerals per sample larger than the ASD measurements of the previous study which is restricted only to SWIR. The minerals identified from SWIR when combined with LWIR provide better estimates of mineral composition of the rock sample.

Besides, the SWIR and LWIR combination has enabled a better characterization of the endmembers when compared to the ASD measurements. One of the uncertainties found in the study of Abweny et al. (2016) is the interpretation of mixed spectra from a single point measurement. For example, in the previous study, it was difficult to differentiate chlorite and actinolite. In this study, the minerals were well characterized whereby thousands and hundreds of pixels from each surface of the sample in SWIR and LWIR respectively were analysed and interpreted.

Furthermore, from an objective method of determining mineral classes, the decision tree, the abundances of minerals were quantitatively estimated from both SWIR and LWIR mineral classes. In the previous study by Abweny et al. (2016), the mineral abundances were calculated from the depth of the diagnostic absorption feature of a mineral. This approach is difficult especially in mixed spectra were the coexisting minerals might have the same spectral features. In this study, the mineral abundances were obtained from the pixel counts of a particular mineral for each rock sample.

In addition, the analysis of SWIR and LWIR images can give the texture of the rock. Texture is important in studying rocks and minerals as it shows the relationship of microstructure between the materials (minerals) of which rock is composed. For example, crystalline texture (broadest textural classes) includes phaneritic, foliated, etc. Texture is quantified from the distribution of the pixel count of a particular mineral in the sample. The study about texture was not the part of this research, but most of the classified samples showed different textures which is worth to study in future. No textural information was discussed from the previous study.

Generally, there is a better reproducibility of the results when compared to the previous study by Abweny et al. (2016). However, this study has indicated that there is a benefit of gaining new insights on studying the metamorphic grade by using HI of SWIR and LWIR. Therefore, the results of this study provide compelling evidence about the ability of SWIR and LWIR hyperspectral imaging on determining the metamorphic grade and assessing the dominant control of metamorphic mineral assemblages.

5. CONCLUSION AND RECOMMENDATION

5.1. Conclusion

This study has proven that the combination of short- and long-wave infrared hyperspectral imaging is a useful method for determining the metamorphic grade and assess the dominant control of metamorphic mineral assemblages when looking at low grade metamorphic volcanic rocks. Different rock samples of varying composition from felsic to ultramafic rocks collected from several greenstone Belts of low grade metamorphic volcanic rocks in East Pilbara, located on the Pilbara Craton, Western Australia were measured using imaging spectrometers of both SWIR and LWIR.

The XRD and petrographic results were integrated with the spectroscopic results to validate the identified minerals before defining mineral assemblages. A decision tree was successfully used to determine mineral classes of each sample and mineral abundances were determined by counting pixels of each mineral class from the created regions of interest of each sample. Combining the dominant mineral abundances from both SWIR and LWIR datasets for each sample has provided additional information, and in this way, 12 sets of different mineral assemblages were determined.

To assess the dominant control of the metamorphic mineral assemblages, a scatter plot of the wavelength position of the MgOH absorption feature near 2335 nm measured by ASD versus the lithological index of oxides of the major elements of the rock samples as adopted from the study Abweny et al. (2016) of was used to plot the measured spectral mineral assemblages of each sample. The results showed that there is a variation of mineral assemblages along both directions; along the wavelength position of the main MgOH absorptions and the lithological index. The variation of assemblages along spectral parameters is related to change of the P – T condition (which determines the metamorphic grade) while the variation along the lithological index is due to chemical composition of the precursor rock. We consider the variation of assemblages along the spectral parameter to be the one that dominantly controls the metamorphic mineral assemblages.

From the variation of mineral assemblages, metamorphic facies were interpreted, and the relationship between spectral parameters and metamorphic grades were also established. To interpret metamorphic facies the measured spectral mineral assemblages were compared with those of Bucher & Grapes (2011) obtained from metabasalts. From the comparison, it was found that assemblages A, B and C relate more to lower amphibolite facies; assemblages D, E, F, H and M relate more to greenschist facies; and assemblages H and N related more to prehnite-pumpellyite facies. The wavelength ranges of each facies were determined and observed to vary along the spectral parameter. Metamorphism decreases towards longer wavelength of the main MgOH absorptions. Lower amphibolite facies dominate at the wavelength range of 2315 – 2330 nm, greenschist facies observed to dominate at the wavelength range of 2330 – 2345 nm greenschist facies and prehnite-pumpellyite facies at 2345 – 2360 nm.

Compared to the previous study of Abweny et al. (2016), this study has produced new results that give new insights in the study of metamorphic rocks. This study has also demonstrated the advantages of the method used over the previous study, basically on mineral identification, mineral quantification and the ability to separate the mixed spectra. Most notably, this is the first study to our knowledge to investigate the effectiveness of the combination of imaging spectrometry in SWIR and LWIR on the determination of metamorphic grades.

In summing up, the combined use of hyperspectral SWIR and LWIR image data for quantifying mineral abundances has provided comprehensive information about metamorphic mineral assemblages of the rock samples collected in the study area. Such information was then used to accurately assess the metamorphic grades and to determine the dominant control of metamorphic mineral assemblages, which is important in the classification of low grade metamorphosed volcanic rocks that represent different rock types. This study is relevant for regional geological mapping and successful exploration of metamorphic mineral deposits hosted in the greenstone belts. As a key result, this study has demonstrated a new approach of the use of hyperspectral imaging by geologists and researchers working in tectonism and ore exploration of metamorphic mineral deposits of Pilbara Craton, Western Australia and related terranes across the globe.

5.2. Recommendations

The results obtained from this study lead to the following recommendations:

- Integration of imaging spectrometry and major elements of lithogeochemistry are found to be useful in determining different metamorphic grades in the low-grade metamorphic volcanic rocks of the Pilbara Craton, Western Australia. It would be interesting to test a similar approach on rocks of higher grades and other locations.
- Further study on the formation of different chlorite compositions is recommended, especially of Fe-chlorite and Mg-chlorite. The study should focus on whether there is temperature variation on the formation of the two species (Fe&Mg) of chlorite.
- During mineral identification, especially when comparing the spectra of the image with the library using spectral analyst tool in ENVI software, the user is recommended to consistently use one form of spectral profile display. The two choices are normal, and continuum removed spectral profile display. When mixing these two, the spectral analyst tool may give different results, which can lead to wrong interpretations. This study has consistently used continuum removed spectral display during mineral identification.
- The use of a decision tree in determining mineral classes works better in SWIR than in LWIR datasets because of the lower noise levels in the SWIR data. The decision tree applies for data with a high signal to noise ratio. For noisy data, the user must be careful to investigate that in the specified wavelength range there are no features detected that are actually due to noise. The LWIR data of this study contained high levels of noise, and hence it was difficult to set decision tree expressions for determining mineral classes. Therefore, a further study on the applicability of a decision tree in noisy data is recommended.
- When XRD is used together with SWIR & LWIR imaging spectrometry on the same datasets, the term data integration is recommended to be used rather than validation. This is because the techniques used by all three methods, XRD, SWIR and LWIR in mineral identification are almost the same. However, the general knowledge of the samples being analysed is highly recommended.
- XRD should not be seen as a validation method when is used along with SWIR and LWIR on the same datasets. This is because each method detects particular types of minerals depending on the technique of the method such as, metal – OH, Si – O and two theta diffraction angle of the mineral for SWIR, LWIR and XRD respectively.

LIST OF REFERENCES

Abweny, M. S., van Ruitenbeek, F. J. A., de Smeth, B., Woldai, T., van der Meer, F. D., Cudahy, T., … Thuss, B. (2016). Short-Wavelength Infrared (SWIR) spectroscopy of low-grade metamorphic volcanic rocks of the Pilbara Craton. *Journal of African Earth Sciences*, *117*, 124–134. https://doi.org/10.1016/j.jafrearsci.2016.01.024

Acosta, I. C. C. (2017). *Mapping Epithermal alteration mineralogy with high spatial resolution hyperspectral imaging of rock samples*. MSc thesis, University of Twente(ITC), Enschede, The Netherland.

Aitkenhead, M. J. (2008). A co-evolving decision tree classification method. *Expert Systems with Applications*, *34*(1), 18–25. https://doi.org/10.1016/j.eswa.2006.08.008

Akkaş, E., Akin, L., Evren Çubukçu, H., & Artuner, H. (2015). Application of Decision Tree Algorithm for classification and identification of natural minerals using SEM-EDS. *Computers and Geosciences*, *80*, 38–48. https://doi.org/10.1016/j.cageo.2015.03.015

Appaji, A. M., & Kumararaman, S. (2013). XRD, FTIR and EDS spectroscopic analysis of elements and minerals present in the rock crystals of Velimalai Hills (Western Ghats), Tamil Nadu, India. *International Journal of Applied Engineering Research*, *8*(5), 553–564. Retrieved from www.ijerd.com

Árkai, P., & Sadek Ghabrial, D. (1997). Chlorite crystallinity as an indicator of metamorphic grade of low-temperature meta-igneous rocks: a case study from the Bükk Mountains, Northeast Hungary. *Clay Minerals*, *32*(02), 205–222. https://doi.org/10.1180/claymin.1997.032.2.04

Bakker, W. H. (2012). *HypPy User Manual. ITC - University of Twente*. Enschede. Retrieved from https://blog.utwente.nl/bakker/hyppy/

Barley, M. E., Sylvester, G. C., Groves, D. I., Borley, G. D., & Rogers, N. (1984). Archaean calc-alkaline volcanism in the Pilbara Block, Western Australia. *Precambrian Research*, *24*(3–4), 285–319. https://doi.org/10.1016/0301-9268(84)90062-7

Blewett, R., & Huston, D. L. (1999). *Deformation and gold mineralisation of the Archaean Pilbara. Agso Research Newsletter*. WA.

Brown, A. J., Cudahy, T. J., & Walter, M. R. (2006). Hydrothermal alteration at the Panorama Formation, North Pole Dome, Pilbara Craton, Western Australia. *Precambrian Research*, *151*, 211–223. https://doi.org/10.1016/j.precamres.2006.08.014

Bucher, K., & Grapes, R. (2011). Metamorphic Grade. In *Petrogenesis of Metamorphic Rocks* (pp. 119–187). Berlin, Heidelberg: Springer Berlin Heidelberg. https://doi.org/10.1007/978-3-540-74169-5_4

Bucher, K., & Graps. (2011). Metamorphism of Mafic Rocks. In *Petrogenesis of Metamorphic Rocks* (pp. 279–327). Berlin, Heidelberg: Springer Berlin Heidelberg. https://doi.org/10.1007/978-3-540-74169-5

Clark, R. N., King, T. V. V., Klejwa, M., Swayze, G. A., & Vergo, N. (1990). High spectral resolution reflectance spectroscopy of minerals. *Journal of Geophysical Research*, *95*(B8), 12653. https://doi.org/10.1029/JB095iB08p12653

Davaabayar, B. (2018). *Evaluating effects of spatial resolution on estimation of mineral abundances using proximal imaging spectroscopy*. University of Twente (ITC).

Deer, W. A., Howie, R. A., & Zussman, J. (1992). *An Introduction to the Rock-Forming Minerals*. (F. R. S. Deer W. A., R. A. Howie, & J. Zussman, Eds.). London: Geological Society of London. Retrieved from https://doi.org/10.1180/DHZ

Duke, E. F. (1994). Near infrared spectra of muscovite, Tschermak substitution, and metamorphic reaction progress: implications for remote sensing. *Geology*, *22*(7), 621–624. https://doi.org/10.1130/0091-7613(1994)022<0621:NISOMT>2.3.CO;2

EXELIS. (2014). ENVI Classic Tutorial: Decision Tree Classification. U.S: Visual Information Solution. Retrieved from http://www.harrisgeospatial.com/portals/0/pdfs/envi/Decision_Tree.pdf

Fagbohun, B. J., Hecker, C. A., & van Ruitenbeek, F. (2015). *Combining Dominant Spectral Features in Airborne Swir and Tir Imagery for Mineralogical Mapping*. University of Twente (ITC). Retrieved from https://webapps.itc.utwente.nl/librarywww/papers_2015/msc/aes/fagbohun.pdf

Geological Survey of Western Australia. (2019). DMIRS Data and Software Centre. Retrieved February 25, 2019, from https://dasc.dmp.wa.gov.au/dasc/

Ghatak, A., Basu, A. R., & Wakabayashi, J. (2012). Elemental mobility in subduction metamorphism: insight from metamorphic rocks of the Franciscan Complex and the Feather River ultramafic belt, California. *International Geology Review*, *54*(6), 654–685. https://doi.org/10.1080/00206814.2011.567087

Gifkins, C., Herrmann, W., & Large, R. (2005). *Altered volcanic rocks : a guide to description and interpretation*. Australia: Centre for Ore Deposit Research, University of Tasmania, Australia. Retrieved from https://trove.nla.gov.au/work/7978107?q&versionId=46617206

Grapes, R. H., & Hoskin, P. W. O. (2004). Epidote Group Minerals in Low–Medium Pressure Metamorphic Terranes. *Reviews in Mineralogy and Geochemistry*, *56*(1), 301–345. Retrieved from http://dx.doi.org/10.2138/gsrmg.56.1.301

Groves, D. ., Goldfarb, R. ., Gebre-Mariam, M., Hagemann, S. ., & Robert, F. (1998). Orogenic gold deposits: A proposed classification in the context of their crustal distribution and relationship to other gold deposit types. *Ore Geology Reviews*, *13*(1–5), 7–27. https://doi.org/10.1016/S0169-1368(97)00012-7

Gupta, B., Uttarakhand, P., & Rawat, I. A. (2017). Analysis of Various Decision Tree Algorithms for Classification in Data Mining. *International Journal of Computer Applications*, *163*(8), 975–8887. Retrieved from https://pdfs.semanticscholar.org/fd39/e1fa85e5b3fd2b0d000230f6f8bc9dc694ae.pdf

Haldar, S. K., & Tišljar, J. (2014). Basic Mineralogy. In *Introduction to Mineralogy and Petrology* (pp. 39–79). Elsevier. https://doi.org/10.1016/B978-0-12-408133-8.00002-X

Hallberg, J. A., & Glikson, A. Y. (1981). Archaean Granite–Greenstone Terranes of Western Australia. In *Developments in Precambrian Geology* (Vol. 2, pp. 33–103). Elsevier. https://doi.org/10.1016/S0166-2635(08)70196-8

Hewson, R. D., Cudahy, T. J., Hausknecht, P., Jurza, P., Connor, P., & Whitbourn, L. B. (2001). Hyperspectral Thermal Infrared Line Profiling for Mapping Surface Mineralogy. In *Fifth International Airborne Remote Conference* (pp. 17–20). San Francisco, CA: Fifth International Airborne Remote Conference. Retrieved from http://citeseerx.ist.psu.edu/viewdoc/download?doi=10.1.1.575.7378&rep=rep1&type=pdf

Hudson Institute of Mineralogy. (n.d.). Mindat.org - Mines, Minerals and More. Retrieved December 27, 2018, from https://www.mindat.org/

Kamona, A. F. (1994). Mineralization types in the Mozambique Belt of eastern Zambia. *Journal of African Earth Sciences*, *19*(3), 237–243. https://doi.org/10.1016/0899-5362(94)90063-9

Kamps, O. M., Ruitenbeek, F. J. A. Van, & Mason, P. R. D. (2018). Near-Infrared Spectroscopy of Hydrothermal versus Low-Grade Metamorphic Chlorites, 1–12. https://doi.org/10.3390/min8060259

Kiyokawa, S., Taira, A., Byrne, T., Bowring, S., & Sano, Y. (2002). Structural evolution of the middle Archean coastal Pilbara terrane, Western Australia. *Tectonics*, *21*(5). https://doi.org/10.1029/2001TC001296

Kuenzer, C., & Dech, S. (2013). Theoretical Background of Thermal Infrared Remote Sensing. In *Thermal Infrared Remote Sensing SE - 1* (Vol. 17, pp. 1–26). https://doi.org/10.1007/978-94-007-6639-6_1

Kuosmanen, V., Arkimaa, H., Tiainen, M., & Bärs, R. (2015). *Hyperspectral close-range LWIR imaging spectrometry-3 case studies* (Vol. 58). Retrieved from http://tupa.gtk.fi/julkaisu/specialpaper/sp_058_pages_117_144.pdf

Lavina, B., Dera, P., & Downs, R. T. (2014). Modern X-ray Diffraction Methods in Mineralogy and Geosciences. *Reviews in Mineralogy and Geochemistry*, *78*(1), 1–31. https://doi.org/10.2138/rmg.2014.78.1

Lehto, T., & Gonçalves, R. (2002). Mineral resources potential in Mozambique GTK Consortium Geological Surveys in Mozambique. *Tapio Lehto & Hannu Mäkitie Geological Survey of Finland, Special Paper*, *48*, 307–321. Retrieved from http://tupa.gtk.fi/julkaisu/specialpaper/sp_048_pages_307_321.pdf

Longhi, I., Sgavetti, M., Chiari, R., & Mazzoli, C. (2001). Spectral analysis and classification of metamorphic rocks from laboratory reflectance spectra in the 0.4-2.5 μ interval: A tool for hyperspectral data interpretation. *International Journal of Remote Sensing*, *22*(18), 3763–3782. https://doi.org/10.1080/01431160010006980

Longhi, Mazzoli, & Sgavetti. (2000). Determination of metamorphic grade in siliceous muscovite-bearing rocks in Madagascar using reflectance spectroscopy. *Terra Nova*, *12*(1), 21–27. https://doi.org/10.1046/j.1365-3121.2000.00264.x

Mathieu, M., Roy, R., Launeau, P., Cathelineau, M., & Quirt, D. (2017). Alteration mapping on drill cores using a HySpex SWIR-320m hyperspectral camera: Application to the exploration of an unconformity-related uranium deposit (Saskatchewan, Canada). *Journal of Geochemical Exploration*, *172*, 71–88. https://doi.org/10.1016/J.GEXPLO.2016.09.008

Olivier, B. (2006). *The geology and petrology of the Merelani Tanzanite deposit, NE Tanzania*. PhD thesis, Stellenbosch University.

Pontual, S., Merry, N., & Gamson, P. (1997). Spectral Analysis Guides for Mineral Exploration: Vol 1 - Spectral Interpretation Field Manual. *AusSpec International Pty.*, *1*, 92.

Raith, M. M., Raase, P., & Reinhardt, J. (2012). *Guide to Thin Section Microscopy*. *Geochimica et Cosmochimica Acta* (Vol. 64). University of Bonn. https://doi.org/10.1016/j.gca.2017.06.026

Richards, J. A. (1993). *Remote Sensing Digital Image Analysis*. *Remote Sensing Digital Image Analysis* (4th Ed.). Berlin, Heidelberg: Springer Berlin Heidelberg. https://doi.org/10.1007/978-3-642-88087-2

Rogge, D., Bachmann, M., Rivard, B., & Feng, J. (2012). Spatial sub-sampling using local endmembers for adapting OSP and SSEE for large-scale hyperspectral surveys. *IEEE Journal of Selected Topics in Applied Earth Observations and Remote Sensing*, *5*(1), 183–195. https://doi.org/10.1109/JSTARS.2011.2168513

Rogge, D. M., Rivard, B., Zhang, J., Sanchez, A., Harris, J., & Feng, J. (2007). Integration of spatial-spectral information for the improved extraction of endmembers. *Remote Sensing of Environment*, *110*(3), 287–303. https://doi.org/10.1016/j.rse.2007.02.019

Sabine, P. A., Harrison, R. K., & Lawson, R. I. (Robert I. (1985). *Classification of volcanic rocks of the British Isles on the total alkali oxide-silica diagram, and the significance of alteration* (4th ed.). London: H.M.S.O. Retrieved from https://catalogue.nla.gov.au/Record/2084929

Salisbury, J. W., Walter, L. S., & D'Aria, D. (1988). *Mid-Infrared (2.5 to 13.5 ym) Spectra of Igneous Rocks*. *U.S, Geological SurveyGeological Survey*. https://doi.org/10.1029/JB094iB07p09192

Smithies, R. H., Champion, D., Van Kranendonk, M., & Hickman, A. (2007). *Geochemistry of volcanic units of the northern Pilbara Craton*. *Geological Survey of Western Australia, Report 104*.

Środoń, J. (2006). Chemistry of Illite/Smectite and End-Member Illite. *Clays and Clay Minerals*, *34*(4), 368–378. https://doi.org/10.1346/ccmn.1986.0340403

Terabayashi, M., Masada, Y., & Ozawa, H. (2003). Archean ocean-floor metamorphism in the North Pole area, Pilbara Craton, Western Australia. *Precambrian Research*, *127*(1–3), 167–180. https://doi.org/10.1016/S0301-9268(03)00186-4

Van Der Meer, F., & de Jong, S. M. (2002). *Imaging Spectrometry*. (F. D. van der Meer & S. M. De Jong, Eds.), *LibTuDelftNet* (Vol. 4). Dordrecht: Springer Netherlands. https://doi.org/10.1007/978-0-306-47578-8

Van Der Meer, F., Jong, S., & Bakker, W. (2006). Imaging Spectrometry: Basic Analytical Techniques. In F. D. van der Meer & S. M. de Jong (Eds.), *Imaging Spectrometry* (pp. 17–61). Enschede, NL: Springer Netherlands. https://doi.org/10.1007/0-306-47578-2_2

Van Kranendonk, M. J. (2010). *The Geology of Coongan 1:100 000 sheet: Western Australia Geological Survey*. (S.

White, Ed.), *1:100 000 Geological Series Explanatory Notes*. Western Australia: Geological Survey of Western Australia.

Van Kranendonk, M. J., Hickman, A. H., Smithies, R. H., & Nelson, D. R. (2002). Geology and tectonic evolution of the Archean North Pilbara Terrain, Pilbara Craton, Western Australia. *Economic Geology*, *97*(4), 695–732. https://doi.org/10.2113/gsecongeo.97.4.695

Van Kranendonk, M. J., Hugh Smithies, R., Hickman, A. H., & Champion, D. C. (2007). Review: secular tectonic evolution of Archean continental crust: interplay between horizontal and vertical processes in the formation of the Pilbara Craton, Australia. *Terra Nova*, *19*(1), 1–38. https://doi.org/10.1111/j.1365-3121.2006.00723.x

Van Ruitenbeek, F., Bakker, W. H., Van Der Werff, H. M. A., Zegers, T. E., Oosthoek, J. H. P., Omer, Z. A., … Van Der Meer, F. D. (2014). Mapping the wavelength position of deepest absorption features to explore mineral diversity in hyperspectral images. *Planetary and Space Science*, *101*, 108–117. https://doi.org/10.1016/j.pss.2014.06.009

Van Ruitenbeek, F. J. A., Cudahy, T. J., van der Meer, F. D., & Hale, M. (2012). Characterization of the hydrothermal systems associated with Archean VMS-mineralization at Panorama, Western Australia, using hyperspectral, geochemical and geothermometric data. *Ore Geology Reviews*, *45*, 33–46. https://doi.org/10.1016/j.oregeorev.2011.07.001

Van Ruitenbeek, F. J. A., Debba, P., Van der Meer, F. D., Cudahy, T., Van der Meijde, M., & Hale, M. (2006). Mapping white micas and their absorption wavelengths using hyperspectral band ratios. *Remote Sensing of Environment*, *102*(3–4), 211–222. https://doi.org/10.1016/J.RSE.2006.02.012

van Ruitenbeek, F. J. A., Werff, H. M. A. van der, Bakker, W., Meer, F. D. van der, Hecker, C. A., & Hein, K. A. A. (2017). Rapid classification of infra-red hyperspectral imagery of rocks with decision trees and wavelength images. Enschede, NL: Earth Systems Analysis, ITC. Retrieved from https://research.utwente.nl/en/publications/rapid-classification-of-infra-red-hyperspectral-imagery-of-rocks-

Visual Information Solutions, I. (1988). *ENVI Version 4.5 April, 2008 Edition Getting Started with ENVI 20GST45DOC*. Retrieved from www.apache.org/

White, R. W. (2003). Prograde Metamorphic Assemblage Evolution during Partial Melting of Metasedimentary Rocks at Low Pressures: Migmatites from Mt Stafford, Central Australia. *Journal of Petrology*, *44*(11), 1937–1960. https://doi.org/10.1093/petrology/egg065

Witt, W. K., Hickman, A. H., Townsend, D., & Preston, W. A. (1998). Mineral potential of the Archaean Pilbara and Yilgarn Cratons, Western Australia. *AGSO Journal of Australian Geology & Geophysics*, *17*(3), 201–221. Retrieved from https://d28rz98at9flks.cloudfront.net/81516/Jou1998_v17_n3_p201.pdf

LIST OF APPENDICES

Input images: minimum wavelength image of 1500-1700 nm and 2100-2400 nm

b1: Wavelength position of the deepest absorption featute for the range of 2100 – 2400 nm
b2: Depth of deepest absorption featute for the range of 2100 – 2400 nm
b3: Wavelength position of the 2nd deepest feature for the range of 2100 – 2400 nm
b5: Wavelength position of the 3rd deepest absorption feature for the range of 2100 – 2400 nm
b11: Wavelength position of the deepest absoption feature for the range of 1530 – 1570 nm

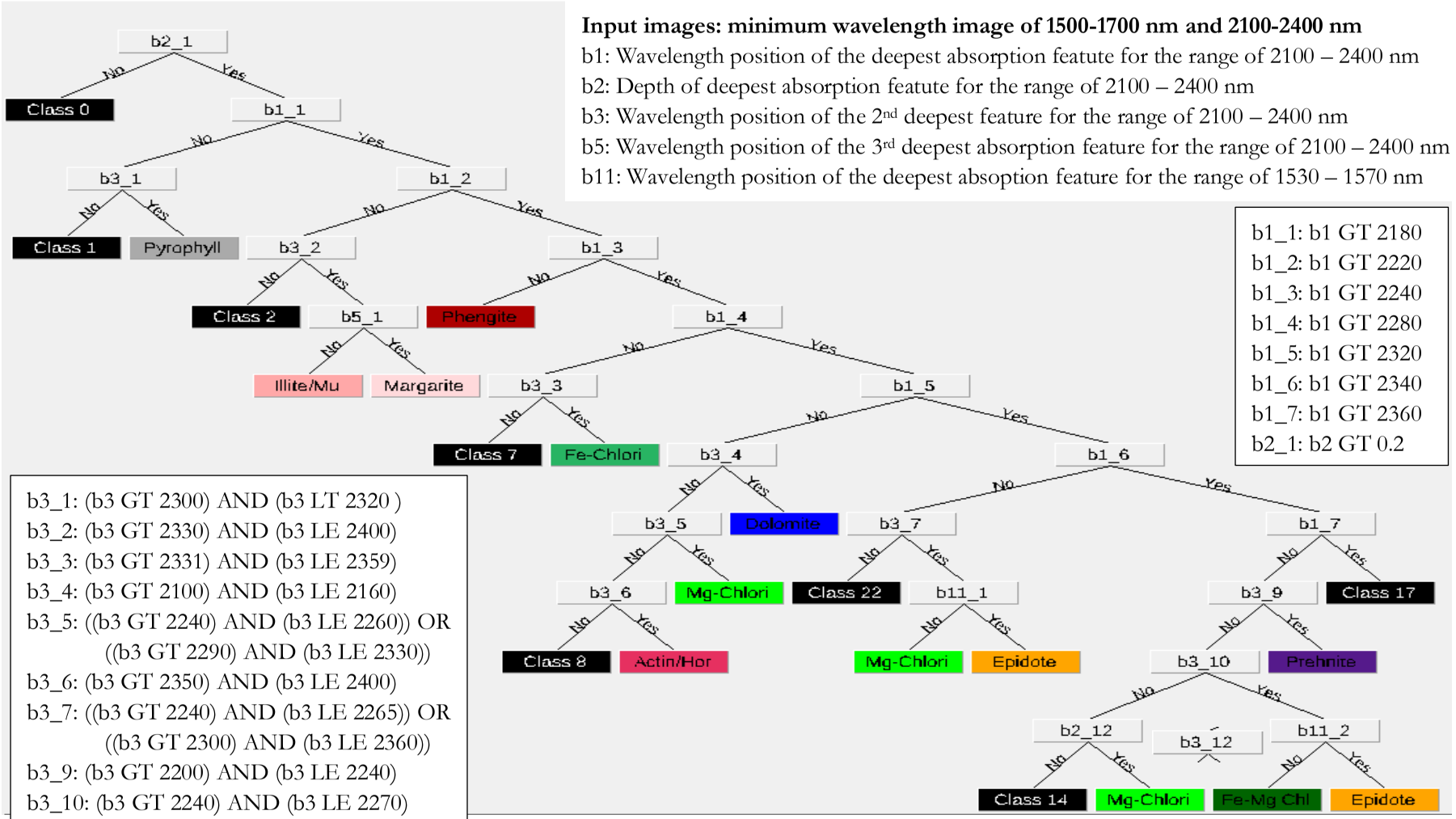

b1_1: b1 GT 2180
b1_2: b1 GT 2220
b1_3: b1 GT 2240
b1_4: b1 GT 2280
b1_5: b1 GT 2320
b1_6: b1 GT 2340
b1_7: b1 GT 2360
b2_1: b2 GT 0.2

b3_1: (b3 GT 2300) AND (b3 LT 2320)
b3_2: (b3 GT 2330) AND (b3 LE 2400)
b3_3: (b3 GT 2331) AND (b3 LE 2359)
b3_4: (b3 GT 2100) AND (b3 LE 2160)
b3_5: ((b3 GT 2240) AND (b3 LE 2260)) OR ((b3 GT 2290) AND (b3 LE 2330))
b3_6: (b3 GT 2350) AND (b3 LE 2400)
b3_7: ((b3 GT 2240) AND (b3 LE 2265)) OR ((b3 GT 2300) AND (b3 LE 2360))
b3_9: (b3 GT 2200) AND (b3 LE 2240)
b3_10: (b3 GT 2240) AND (b3 LE 2270)
b3_12: (b3 GT 2300) AND (b3 LE 2350)
b5_1: (b5 GT 2240) AND (b5 LE 2270)
b11_1: (b11 GT 1530) AND (b11 LT 1570)
b11_2: (b11 GT 1530) AND (b11 LT 1570)

Decision tree expression used to determine mineral classes in SWIR images

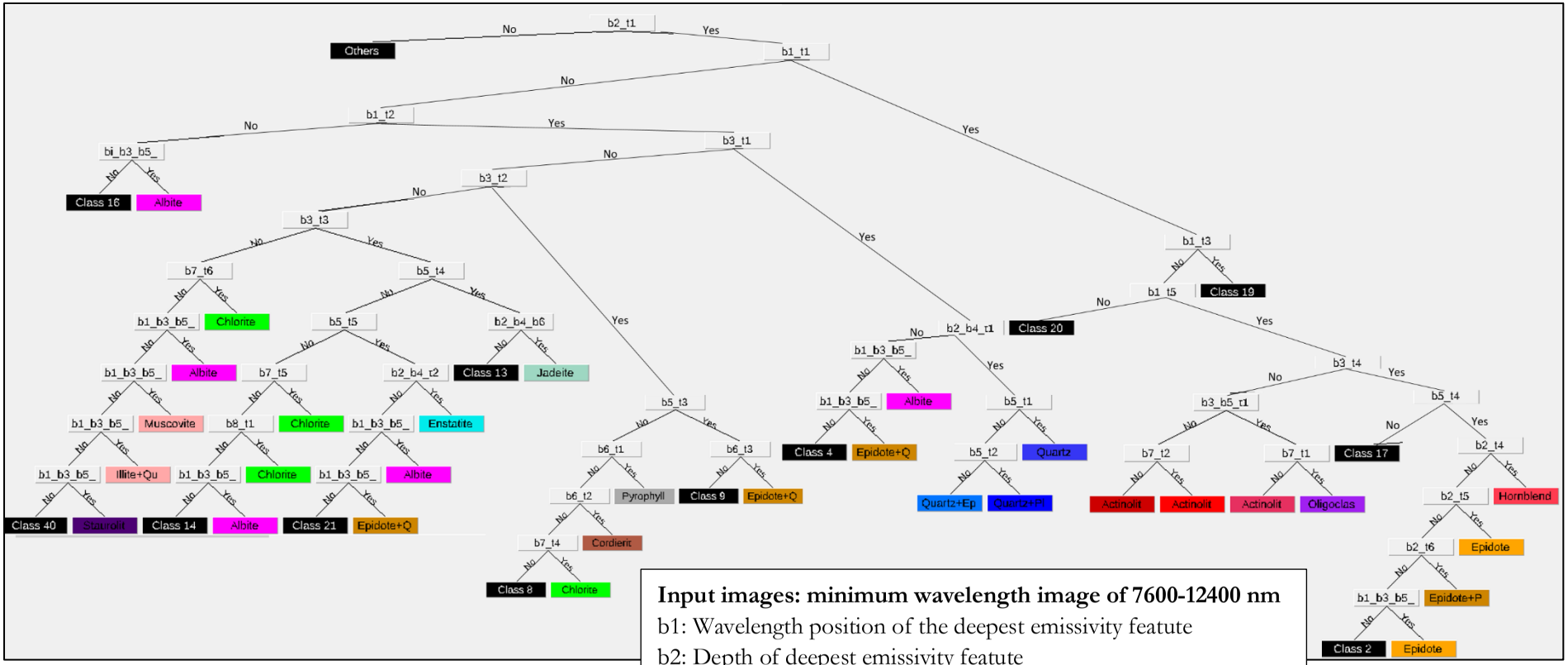

Input images: minimum wavelength image of 7600-12400 nm

b1: Wavelength position of the deepest emissivity featute
b2: Depth of deepest emissivity featute
b3: Wavelength position of the 2nd deepest emissivity feature
b4: Depth of the 2nd deepest emissivity feature
b5: Wavelength position of the 3rd deepest emissivity feature
b6: Depth of the 3rd deepest emissivity feature
b7: Ratio of b2/b4
b8: Ratio of (b2-b4)/(b4-b6)

Decision tree expression used to determine mineral classes in LWIR image

Decision tree expresions for LWIR:

b2_t1: b2 GT 0.045

b1_t1: b1 GT 9900

b1_t2: ((b1 GT 8100) AND (b1 LT 8350)) OR ((b1 GT 9100) AND (b1 LT 9400)) OR ((b1 GT 9000) AND (b1 LT 9900))

b1_t3: b1 GT 10500

b1_t5: ((b1 GT 9830) AND (b1 LT 10500)) OR ((b1 GT 9100) AND (b1 LT 9600))

bi_b3_b5_t3: (((b1 GT 9500) AND (b1 LT 9740)) OR ((b1 GT 8200) AND (b1 LT 8500)) OR ((b1 GT 9050) AND (b1 LT 9350))) AND (((b3 GT 9550) AND (b3 LT 9740)) OR ((b3 GT 8200) AND (b3 LT 8500)) OR ((b3 GT 9100) AND (b3 LT 9300)) OR ((b3 GT 9780) AND (b3 LT 10000))) AND (((b5 GT 9100) AND (b5 LT 9300)) OR ((b5 GT 9800) AND (b5 LT 10100)) OR ((b5 GT 8200) AND (b5 LT 8500)) OR ((b5 GT 8650) AND (b5 LT 8940)))

b3_t1: ((b3 GT 8100) AND (b3 LT 8350)) OR ((b3 GT 9100) AND (b3 LT 9400))

b3_t2: (b3 GT 8600) AND (b3 LT 8850)

b3_t3: ((b3 GT 9550) AND (b3 LT 9700)) OR ((b3 GT 9050) AND (b3 LT 9250)) OR ((b3 GT 9800) AND (b3 LT 10600))

b2_b4_t1: (b2 GT 0.12) AND (b4 GT 0.10)

b3_t4: (b3 GT 9100) AND (b3 LT 9600) OR ((b3 GT 9830) AND (b3 LT 10500))

b5_t4: ((b5 GT 8650) AND (b5 LT 8940)) OR ((b5 GT 9100) AND (b5 LT 9600))

b2_t4: b7 GT 1.3

b2_t5: (b2 GT 0.08) AND (b2 LT 0.17)

b2_t6: (b2 GT 0.05) AND (b2 LT 0.08)

b1_b3_b5_t7: ((b1 GT 9900) AND (b1 LT 10400)) AND ((b3 GT 9100) AND (b3 LT 9450)) AND ((b5 GT 8650) AND (b5 LT 8940))

b3_b5_t1: ((b3 GT 9500) AND (b3 LT 10200)) AND ((b5 GT 8100) AND (b5 LT 8980))

b7_t1: b7 LT 1.25

b7_t2: b7 GT 1.6

b5_t1: b5 GT 11100

b5_t2: (b5 GT 8200) AND (b5 LT 9700)

b1_b3_b5_t4: (((b1 GT 9500) AND (b1 LT 9740)) OR ((b1 GT 8200) AND (b1 LT 8500)) OR ((b1 GT 9050) AND (b1 LT 9350))) AND (((b3 GT 9550) AND (b3 LT 9740)) OR ((b3 GT 8200) AND (b3 LT 8500)) OR ((b3 GT 9100) AND (b3 LT 9300)) OR ((b3 GT 9780) AND (b3 LT 10000))) AND (((b5 GT 9100) AND (b5 LT 9300)) OR ((b5 GT 9800) AND (b5 LT 10100)) OR ((b5 GT 8200) AND (b5 LT 8500)) OR ((b5 GT 8650) AND (b5 LT 8940)))

b1_b3_b5_t6: (((b1 GT 8750) AND (b1 LT 9500)) OR ((b1 GT 7950) AND (b1 LT 8550))) AND (((b3 GT 8750) AND (b3 LT 9500)) OR ((b3 GT 7950) AND (b3 LT 8550)) OR ((b3 GT 9780) AND (b3 LT 10500))) AND (((b5 GT 9780) AND (b5 LT 10500)) OR ((b5 GT 8750) AND (b5 LT 9500)) OR ((b5 GT 7950) AND (b5 LT 8550))) AND (b2 GT 0.05) AND (b4 GT 0.05) AND (b6 GT 0.03)

b5_t3: (b5 GT 9900) AND (b5 LT 10200)

b6_t3: b6 GT 0.07

b6_t1: b6 GT 0.2

b6_t2: (b6 GT 0.125) AND (b6 LT 0.2)

b7_t4: b7 GT 1.5

b5_t4: ((b5 GT 9750) AND (b5 LT 9950)) OR ((b5 GT 9500) AND (b5 LT 9700))

b2_b4_b6: ((b2 GT 0.08) AND (b4 GT 0.07) AND (b6 GT 0.06)) AND ((b1 GT 8900) AND (b1 LT 9400))

b5_t5: ((b5 GT 10200) AND (b5 LT 10600)) OR ((b5 GT 9000) AND (b5 LT 9300))
b2_b4_t2: (b2 GT 0.2) AND (b4 GT 0.18)
b1_b3_b5_t5: ((b1 GT 9450) AND (b1 LT 9750)) AND ((b3 GT 9750) AND (b3 LT 10000)) AND ((b5 GT 9100) AND (b5 LT 9450))
b1_b3_b5_t7: (((b1 GT 9000) AND (b1 LT 9400)) AND ((b3 GT 9900) AND (b3 LT 10500)) AND (((b5 GT 9900) AND (b5 LT 10500)) OR ((b5 GT 8000) AND (b5 LT 8650))))
b7_t5: b7 GT 1.5
b8_t1: b8 LT 0.4
b1_b3_b5_t2: (((b1 GT 9500) AND (b1 LT 9740)) OR ((b1 GT 8200) AND (b1 LT 8500)) OR ((b1 GT 9050) AND (b1 LT 9350))) AND (((b3 GT 9550) AND (b3 LT 9740)) OR ((b3 GT 8200) AND (b3 LT 8500)) OR ((b3 GT 9100) AND (b3 LT 9300)) OR ((b3 GT 9780) AND (b3 LT 10000))) AND (((b5 GT 9100) AND (b5 LT 9300)) OR ((b5 GT 9800) AND (b5 LT 10100)) OR ((b5 GT 8200) AND (b5 LT 8500)) OR ((b5 GT 8650) AND (b5 LT 8940)))
b7_t6: b7 GT 1.5
b1_b3_b5_t1: (((b1 GT 9500) AND (b1 LT 9740)) OR ((b1 GT 8200) AND (b1 LT 8500)) OR ((b1 GT 9050) AND (b1 LT 9350))) AND (((b3 GT 9550) AND (b3 LT 9740)) OR ((b3 GT 8200) AND (b3 LT 8500)) OR ((b3 GT 9100) AND (b3 LT 9300)) OR ((b3 GT 9780) AND (b3 LT 10000))) AND (((b5 GT 9100) AND (b5 LT 9300)) OR ((b5 GT 9800) AND (b5 LT 10100)) OR ((b5 GT 8200) AND (b5 LT 8500)) OR ((b5 GT 8650) AND (b5 LT 8940)))
b1_b3_b5_t3: ((b1 GT 9150) AND (b1 LT 9350)) AND ((b3 GT 8850) AND (b3 LT 9150)) AND ((b5 GT 8200) AND (b5 LT 8600))
b1_b3_b5_t4: ((b1 GT 9150) AND (b1 LT 9350)) AND ((b3 GT 8300) AND (b3 LT 8600)) AND ((b5 GT 10000) AND (b5 LT 12000))
b1_b3_b5_t6: (((b1 GT 9100) AND (b1 LT 9400)) AND ((b3 GT 9550) AND (b3 LT 9900)) AND (((b5 GT 8000) AND (b5 LT 8400)) OR ((b5 GT 9550) AND (b5 LT 9690))))

Appendix 2: Decision tree mineral classes from SWIR and LWIR images

a) SWIR mineral classes

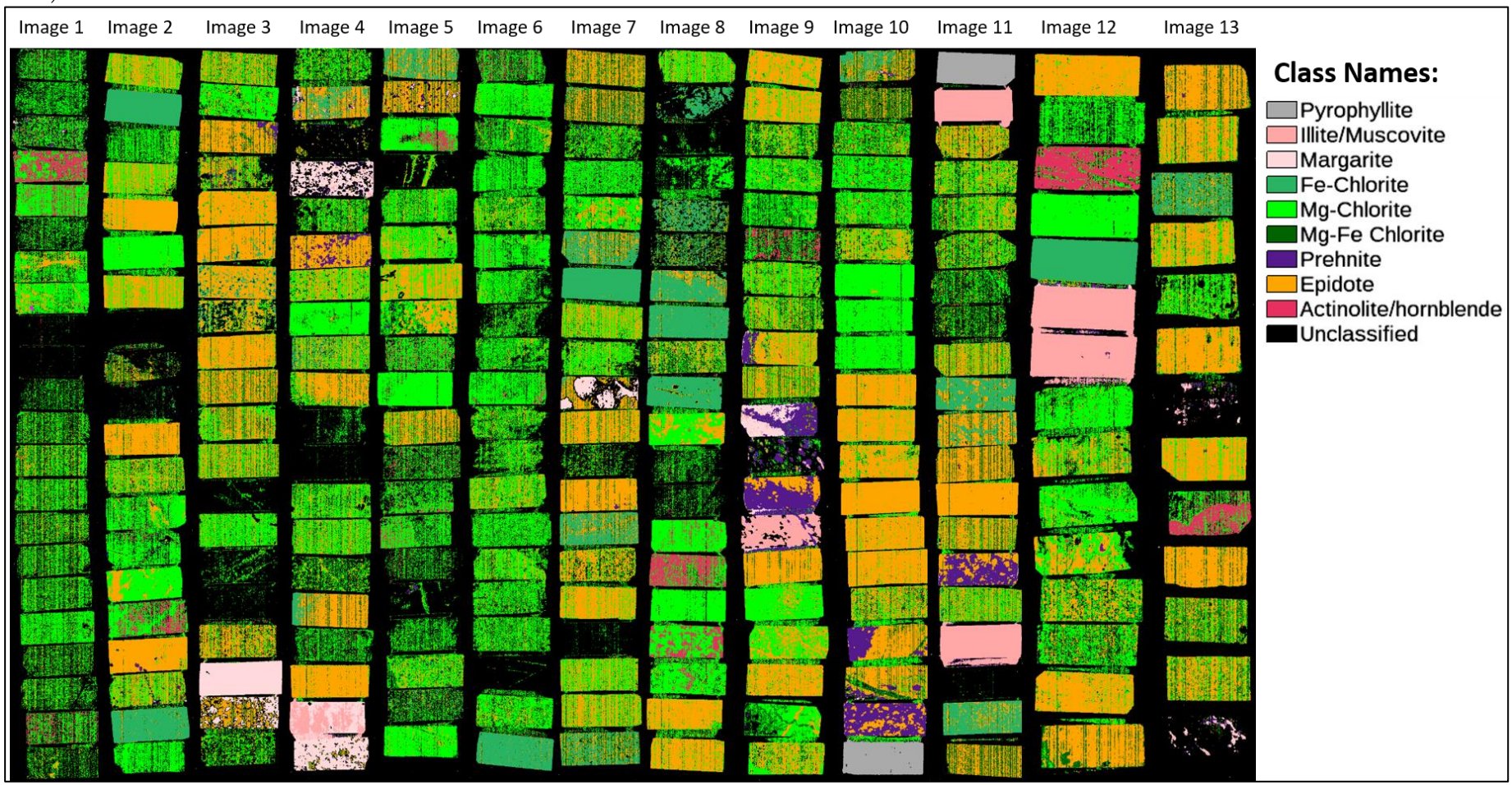

SWIR Sample numbers.

Background: SWIR hyperspectral images displayed in RGB (R= 1309.4600 nm, B= 1782.5400 nm, G= 2118.9099 nm)

b) LWIR mineral classes

LWIR Sample numbers.

Background: LWIR hyperspectral emissivity image displayed in RGB (R= 8563.7900 nm, B= 10163.5000 nm, G= 11857.2002 nm)

Appendix 3: Interpreted metamorphic mineral assemblages from mineral abundances

Sample no.	SWIR mineral abundances (%)										LWIR mineral abundances (%)													Interpreted metamorphic mineral assemblages by qualitatively combining SWIR and LWIR mineral abundances	Assemblage code
	Epidote	Mg-Chlorite	Fe-Chlorite	Mg-Fe Chlorite	Actinolite/Hbl	Prehnite	Illite/Muscov	Margarite	Pyrophyllite	Unclassified	Epidote	Chlorite	Actinolite	Hornblende	Quartz	Jadeite	Enstatite	Oligoclase	Albite	Illite/Muscov	Pyrophyllite	Cordierite	Unclassified		
179752		92			2					6	1		29	48									21	Mg-chlorite, Hornblende	A
179755		37			13					50	2	2	44	34	1								17	Mg-chlorite, Hornblende	A
179807		39								60	15		47	24				1					13	Mg-chlorite, Hornblende+ Epidote	A
179814	32	61								6	16		10	59									15	Hornblende, Mg-chlorite +Epidote	A
179818		30			58					12	2		25	50									24	Hornblende, Mg-chlorite	A
179819		93								7	9		35	16				3					38	Hornblende, Mg-chlorite	A
179821	3	73			8					16	6		1	78									16	Hornblende, Mg-chlorite	A
179828	4	60			1					35	18		9	42		2			3				24	Hornblende, Mg-chlorite	A
179728	1	90								9	1		74	8									16	Mg-chlorite, Epidote, Hornblende	A
180221		94								6	6		64	13									16	Mg-chlorite, Actinolite, Hornblende	A
179731		12			1					87	45		10	18									27	Epidote, Hornblende, Mg-chlorite	B
179760	1	40			1					57	20		26	18				4					32	Mg-chlorite, Epidote, Hornblende	B
179762	21	54		3						22	22		33	20				2					23	Epidote, Hornblende, Mg-chlorite	B
179789	23	60		2						14	15		36	29				6					14	Mg-chlorite, Hornblende, Epidote	B
179824	75	11		4						11	67		4	10									19	Epidote, Mg-chlorite, Hornblende	B
179825	62	12								25	29		17	35				1					19	Hornblende, Epidote, Mg-chlorite	B
179827	13	67			2					19	22		4	18									56	Mg-chlorite, Epidote, Hornblende	B
179738		45			5					50	46		5	5									44	Epidote, Mg-chlorite, Hornblende	B
179764	6	84								10	6		72	10									11	Mg-chlorite, Epidote, Hornblende	B
176767	19	68								14	12		57	2				4					26	Mg-chlorite, Epidote, Actinolite +Hornblende	B
176785	4	56			1					40	3		59					7					30	Mg-chlorite, Actinolite	C
176786	1	56			2					40	13		35	2				14	3				33	Mg-chlorite, Actinolite	C
179751		59			18					23	3	15	7		16			6	1				51	Mg-chlorite, Actinolite	C
179756		48			9					43		73			1				9				16	Mg-chlorite, Actinolite	C
179757		57			13					30		83							4				13	Mg-chlorite , Actinolite	C
179765		68								31			91					3					5	Mg-chlorite, Actinolite	C
179767		46			17					37	3		62	2				1					33	Mg-chlorite, Actinolite	C

Sample no.	SWIR mineral abundances (%)										LWIR mineral abundances (%)												Interpreted metamorphic mineral assemblages by qualitatively combining SWIR and LWIR mineral abundances	Assemblage code
	Epidote	Mg-Chlorite	Fe-Chlorite	Mg-Fe Chlorite	Actinolite/Hbl	Prehnite	Illite/Muscov	Margarite	Pyrophyllite	Unclassified	Epidote	Chlorite	Actinolite	Hornblende	Quartz	Jadeite	Enstatite	Oligoclase	Albite	Illite/Muscov	Pyrophyllite	Cordierite	Unclassified		
179768	4	77								19	2		71	12									15	Mg-chlorite, Actinolite + Hornblende	C
179770	2	77			4					17	19		56	7	1			3					15	Mg-chlorite, Actinolite, +Hornblende	C
179815		25			3					71	2	17	37					1					44	Mg-chlorite, Actinolite	C
179816		17			3					80	12	1	34	1				24					28	Mg-chlorite, Actinolite + Plagioclase	C
179817		83			11					6	5		63	10									22	Mg-chlorite, Actinolite + Hornblende	C
179820		62			33					5	4		74	8									14	Mg-chlorite, Actinolite +Hornblende	C
179829		35			24					41	10		23	4				54	1				8	Mg-chlorite, Actinolite	C
176752		72								28	1		14					77					8	Mg-chlorite, Actinolite, Plagioclase	C
176765	1	65		1	4					30	4		75	3				5					13	Mg-chlorite, Actinolite +Hornblende	C
176766		68								31	1		73	10									16	Mg-chlorite, Actinolite +Hornblende	C
176768		48			27					26			71					25					4	Mg-chlorite, Actinolite, Plagioclase	C
179886		93								7	1		24	6				55					15	Mg-chlorite, Actinolite, Hornblende + Plagioclase	C
180219		67			1					32			29					60					11	Mg-chlorite, Actinolite + Plagioclase	C
180220		14			74					11			12					74	1				13	Mg-chlorite, Actinolite + Plagioclase	C
176789	5	68			2					25	18		49	6				7					21	Mg-chlorite, Epidote, Actinolite	D
179727	40	42		4						14	43		32					1					25	Epidote, Mg-chlorite, Actinolite	D
179749	60	30								10	7		27					31	3				32	Epidote, Mg-chlorite, Actinolite	D
179750	39	36		10		2				12	11		38			2		8	4				37	Epidote, Mg-chlorite, Actinolite	D
179753	52	12		23						13	20		30		2			1					47	Epidote, Actinolite, Mg-chlorite	D
179769	7	50			3					39	14	4	36	1				22					24	Mg-chlorite, Actinolite, Epidote + Plagioclase	D
179771	5	58			1					36	45		30	1	7			1					15	Mg-chlorite, Actinolite, Epidote	D
179772	3	31			1					66	3		68	5				5					19	Mg-chlorite, Actinolite, Epidote +Hornblende	D
179778	19	57								24	24		40	5				6					25	Mg-chlorite, Actinolite, Epidote	D
179780	8	62								30	13		62	11									14	Mg-chlorite, Actinolite, Epidote +Hornblende	D
179782		1								98	6	1	19	1	29	1		9	3	7			25	Actinolite+Quartz, Plagioclase	D
179783	13	62								25	1		28					56	2				14	Epidote, Mg-chlorite, Actinolite + Plagioclase	D
179794	18	54		5						23	1		10		1	2			41				44	Epidote, Mg-chlorite, Actinolite + Plagioclase	D
179798	50	20		3						27	40		12					1					47	Epidote, Mg-chlorite, Actinolite	D

Sample no.	SWIR mineral abundances (%)										LWIR mineral abundances (%)													Interpreted metamorphic mineral assemblages by qualitatively combining SWIR and LWIR mineral abundances	Assemblage code
	Epidote	Mg-Chlorite	Fe-Chlorite	Mg-Fe Chlorite	Actinolite/Hbl	Prehnite	Illite/Muscov	Margarite	Pyrophyllite	Unclassified	Epidote	Chlorite	Actinolite	Hornblende	Quartz	Jadeite	Enstatite	Oligoclase	Albite	Illite/Muscov	Pyrophyllite	Cordierite	Unclassified		
179799	75	16		1						8	3		16					52					29	Epidote, Mg-chlorite, Actinolite + Plagioclase	D
179801	40	50		3						7	18		39					2	18				23	Epidote, Mg-chlorite, Actinolite + Plagioclase	D
179826	65	18		1						16	46		16	1				3					34	Epidote, Mg-chlorite, Actinolite	D
179864	23	50		1						25	6		11		3	8			35				37	Mg-chlorite, Epidote, Actinolite + Plagioclase	D
176753	44	29		3						24	2		19			10		16	31				22	Epidote, Mg-chlorite, Actinolite, Plagioclase	D
176755	44	44								11			12					79					9	Epidote, Mg-chlorite, Actinolite, Plagioclase	D
176759	67	30								3	13		37										49	Epidote, Mg-chlorite, Actinolite	D
179874	12	76								12	4		12					71					13	Mg-chlorite, Epidote, Actinolite + Plagioclase	D
179875	43	50								7	14		36	1				19					29	Epidote, Mg-chlorite, Actinolite + Plagioclase	D
179881	18	52								30	2	6	16			1			17				57	Mg-chlorite, Epidote, Actinolite + Plagioclase	D
180204	7	40								53	7		17						21				55	Mg-chlorite, Actinolite, Epidote	D
179758		28			5					67		24	3					1	11				61	Mg-chlorite	E
179766		68																						Mg-chlorite	E
179773		78			5					17	1				30	5			4	4		15	41	Mg-chlorite + Quartz, Cordierite	E
179774	12	46		1						41	1				43				11	16		9	20	Mg-chlorite + Quartz	E
179779	6	54								40			1		13			1	11	9		24	42	Mg-chlorite + Quartz, Cordierite	E
176758	1	90								9			4					91					5	Mg-chlorite, Plagioclase	E
179885		92								8	10				19	1			23			2	44	Epidote, Mg-chlorite + Plagioclase, Quartz	E
176777	91	7		2						1	68												32	Epidote	F
176781	88	7		5						0	81			2									18	Epidote	F
179716	82	5		5						7														Epidote	F
179718	77	17								6														Epidote	F
179732		1								99	27		5			2			4				63	Epidote	F
179739	93	2		3						2	64				18				1				17	Epidote	F
179806		5			1					94	25				10	6			31	1			27	Epidote +Plagioclase, Quartz	F
176756	86	4								10	40		1			2			1				55	Epidote	F
176763	86	2		5						6	4				79				8				10	Epidote + Quartz	F
176769	84	2		1		1				12	20		2		10				5	1		15	48	Epidote	F

Sample no.	SWIR mineral abundances (%)										LWIR mineral abundances (%)													Interpreted metamorphic mineral assemblages by qualitatively combining SWIR and LWIR mineral abundances	Assemblage code
	Epidote	Mg-Chlorite	Fe-Chlorite	Mg-Fe Chlorite	Actinolite/Hbl	Prehnite	Illite/Muscov	Margarite	Pyrophyllite	Unclassified	Epidote	Chlorite	Actinolite	Hornblende	Quartz	Jadeite	Enstatite	Oligoclase	Albite	Illite/Muscov	Pyrophyllite	Cordierite	Unclassified		
179873	72	2		7						19	2				17	1			26	12		1	42	Epidote+Plagioclase, Quartz	F
179887	91	5		2						2	11	9			10				4				65	Epidote	F
179888	88	8		1						3	7	2			16	1			17	11			47	Epidote +Plagioclase, Quartz	F
179890	90	1								9	19	1			9				1				70	Epidote+ Quartz	F
179891	83	6		1						10	37				2	1			16	7			38	Epidote + Plagioclase	F
179892	82	4		2						11	58				1	3			7				32	Epidote	F
180210	95			1						4	2				34				24	11		1	28	Epidote +Plagioclase, Quartz	F
180218	90	4								6	44								2				55	Epidote	F
179709	3	1		4		1				91	4				13	1			48	4			31	Plagioclase, Quartz	G
179745	5	9								86			1					1	59	1			39	Plagioclase	G
179759	1	5		2		1				91	8		2		30			1	22	1		5	31	Plagioclase, Quartz	G
179800		3								97			6					10	60				24	Plagioclase	G
176760										100	4				18				24				54	Plagioclase, Quartz	G
176762		1	2	1						95					91					3			6	Quartz ± Epidote, Fe-chlorite	G
180215		1								99	7				20				38	1			34	Plagioclase, Quartz	G
176799	1	35	2		4					58	1				10	1			51	1			36	Mg-chlorite, Fe-chlorite + Plagioclase	H
179705	45		29	9		3		4		10					47	3			28	1			20	Epidote, Fe-chlorite, Plagioclase +Quartz	H
179725	18	1	62	17						3														Fe-chlorite, Mg-Fe chlorite + Epidote	H
179737	64		14	14						8		1	3					10	42				45	Epidote, Fe-chlorite+ plagioclase	H
179742	33		47	11						9	1				50				29				20	Fe-chlorite, Epidote +Plagioclase, Quartz	H
179763	5	27	7	3	3					55	1	1			56				3				40	Mg-chlorite, Fe-chlorite + Quartz	H
179784	3		73	2						22	2				88				7				3	Fe-chlorite + Quartz	H
179790	26	1	51	12						10	18				52				2				27	Fe-chlorite, Epidote + Quartz	H
179792			90							10					82					5		1	11	Fe-chlorite + Quartz	H
179797	24		61	11						5	5				44				20	13		1	17	Fe-chlorite, Epidote + Plagioclase, Quartz	H
179803	23	3	42	22						11	5				5	26			29	1			32	Fe-chlorite, Epidote + Plagioclase, pyroxene	H
179808	9		46	12						33					8	16			55	1			21	Fe-chlorite + Plagioclase, pyroxene	H
179809	11	1	25	20						43	15				1	8			36	2			38	Fe-chlorite, Epidote, + Plagioclase, pyroxene	H

Sample no.	SWIR mineral abundances (%)										LWIR mineral abundances (%)													Interpreted metamorphic mineral assemblages by qualitatively combining SWIR and LWIR mineral abundances	Assemblage code
	Epidote	Mg-Chlorite	Fe-Chlorite	Mg-Fe Chlorite	Actinolite/Hbl	Prehnite	Illite/Muscov	Margarite	Pyrophyllite	Unclassified	Epidote	Chlorite	Actinolite	Hornblende	Quartz	Jadeite	Enstatite	Oligoclase	Albite	Illite/Muscov	Pyrophyllite	Cordierite	Unclassified		
179810	17		68	4						10					40				38				23	Fe-chlorite, Epidote + Plagioclase, Quartz	H
179811	2		90	1						6	3		1		32			1	19				44	Fe-chlorite + Plagioclase, Quartz	H
179813	3	1	84	2						10	1				61				1	1			36	Fe-chlorite+Quartz	H
176754			82							18	1				89				1	1			7	Mg-chlorite, Fe-chlorite+ Quartz	H
176771	3		80	2						15					92					1			6	Fe-chlorite + Quartz	H
179879	33	3	29	21						12	2				87					2			9	Epidote, Fe-chlorite + Quartz	H
180207	18		72	5						5					1				82				17	Fe-chlorite, Epidote + Plagioclase	H
180208	55		21	13						10		3			12	1			51				34	Epidote, Fe-chlorite, Plagioclase +Quartz	H
180216	19		68	3						9	17				5	1			12	1			63	Fe-chlorite, Epidote	H
180222			86							14					98					1			1	Fe-chlorite + Quartz	H
176783	47	32		18		1				3	8				43				34	1			15	Epidote, Mg-chlorite + Quartz	K
176787	47	34		19						0	22		1		1	5			15				56	Epidote, Mg-chlorite, plagioclase	K
176788	14	74		5						7	13		1		21	7			32	2			24	Mg-chlorite, Epidote + plagioclase	K
179711	70	13		10						7														Epidote, Mg-chlorite	K
179714	12	44		5						39	1		1		23	1			29				46	Epidote, Mg-chlorite	K
179715	12	49		3						36														Epidote, Mg-chlorite	K
179720	63	21		6						10														Epidote, Mg-chlorite	K
179722	54	21		21						4														Epidote, Mg-chlorite	K
179730	65	16		11						8	35		2	1	5	5			2	1			48	Epidote, Mg-chlorite	K
179733	18	58	1	2						22	4		1		25	4			23				37	Mg-chlorite, Epidote + plagioclase	K
179734	25	54		9						12	14				2	2			11				70	Epidote, Mg-chlorite + plagioclase	K
179746	13	64								22	50		6			4			5				34	Epidote, Mg-chlorite	K
179748	29	60								10	6				25	2			11	7			48	Mg-chlorite, Epidote +Plagioclase, Quartz	K
179761	19	53		8		2				18	3		2		32	4			5	1		3	49	Mg-chlorite, Epidote	K
179776	3	68			1					28	10				11	5			21	2		3	49	Mg-chlorite, Epidote +Plagioclase, Quartz	K
179787	10	48		1						40	14		1		1	4			57	1			22	Epidote, Mg-chlorite, plagioclase	K
179795	8	53								4	20	1			66				1				13	Epidote, Mg-chlorite + Quartz	K
179796	5	14	3	6						0	22				2				53	4			19	Epidote, Mg-chlorite, plagioclase	K

Sample no.	SWIR mineral abundances (%)										LWIR mineral abundances (%)													Interpreted metamorphic mineral assemblages by qualitatively combining SWIR and LWIR mineral abundances	Assemblage code
	Epidote	Mg-Chlorite	Fe-Chlorite	Mg-Fe Chlorite	Actinolite/Hbl	Prehnite	Illite/Muscov	Margarite	Pyrophyllite	Unclassified	Epidote	Chlorite	Actinolite	Hornblende	Quartz	Jadeite	Enstatite	Oligoclase	Albite	Illite/Muscov	Pyrophyllite	Cordierite	Unclassified		
179802	55	32		10						3			8					16	50				26	Epidote, Mg-chlorite, plagioclase	K
179805	28	54		1						17	3				16				11	9		6	54	Epidote, Mg-chlorite, plagioclase+Quartz	K
179812	30	32	8	2						28	1				1	3			4				50	Epidote, Mg-chlorite	K
179822	26	46								27	81			1									17	Epidote, Mg-chlorite	K
179823	85	10		1						4	19				6				2	5		2	65	Epidote, Mg-chlorite	K
179865	32	40		4						24	2				26	2			21	17			32	Mg-chlorite, Epidote+ Plagioclase, Quartz	K
176764	34	38		6						23	7				78				6	5			4	Mg-chlorite, Epidote +Quartz	K
176770	34	30		14		2				20					10				70				21	Epidote, Mg-chlorite, plagioclase	K
176772	46	38		8						8					74				5	11		1	10	Epidote, Mg-chlorite + Quartz	K
176773	6	59			1					34	41		1		3	8			19				28	Epidote, Mg-chlorite, Plagioclase	K
179867	61	18		2		10				9	57			5									38	Epidote, Mg-chlorite+ Prehnite	K
179868	50	22		20						7					51				3	24		2	20	Epidote, Mg-chlorite + Plagioclase, Quartz	K
179876	81	11		2						6	13				5	9			3				70	Epidote, Mg-chlorite + Pyroxene	K
179878	52	35		1		2				12		4	9					12	54				21	Epidote, Mg-chlorite+ Plagioclase	K
179883	46	38								15	52	1			1				2				44	Epidote, Mg-chlorite	K
179889	79	15		1						5	10				26	1			1				61	Epidote, Mg-chlorite + Quartz	K
179893	45	30		3						22	41					1			6				52	Epidote, Mg-chlorite	K
179900	54	21		1						24	28												71	Epidote, Mg-chlorite	K
180201	34	48								18	32				6	5			9				49	Epidote, Mg-chlorite	K
180203	22	39								39	44					1			2				52	Epidote, Mg-chlorite	K
180213	39	38	2	14						7					44	8			24	1			22	Epidote, Mg-chlorite, Plagioclase +Quartz	K
176782	64	9		26						1	4				57				13	12			15	Epidote, Mg-Fe chlorite + Quartz	L
179704	80	1		11						7														Epidote, Mg-Fe chlorite	L
179708	75		1	18						6														Epidote, Mg-Fe chlorite	L
179717	31	24		33						12														Epidote, Mg-Fe chlorite, Mg-chlorite	L
179785	51	5		25						19	1				83				1	7		1	7	Epidote, Mg-Fe chlorite + Quartz	L
176761	13	2	3	18						63					92					1			6	Mg-Fe chlorite, Epidote + Quartz	L
179880	28	7	2	50						12					36				36				28	Mg-Fe chlorite, Epidote+ Plagioclase, Quartz	L

Sample no.	SWIR mineral abundances (%)										LWIR mineral abundances (%)													Interpreted metamorphic mineral assemblages by qualitatively combining SWIR and LWIR mineral abundances	Assemblage code
	Epidote	Mg-Chlorite	Fe-Chlorite	Mg-Fe Chlorite	Actinolite/Hbl	Prehnite	Illite/Muscov	Margarite	Pyrophyllite	Unclassified	Epidote	Chlorite	Actinolite	Hornblende	Quartz	Jadeite	Enstatite	Oligoclase	Albite	Illite/Muscov	Pyrophyllite	Cordierite	Unclassified		
180209	61			21						17	1				34				35				29	Epidote +Plagioclase, Quartz	L
180211	58	11		24						8					5				72				23	Epdote, Mg-Fe clorite, Plagioclase	L
180217	48	1		38						13	40								18				42	Epidote, Mg-Fe chlorite + Plagioclase	L
176784	13	70								16	21		1		6	12			23			1	35	Mg-chlorite, Epidote, Pyroxebe + Plagioclase	M
179701	12	53		6	1					28	2				40	10			18	4			25	Mg-chlorite, Epidote, Pyroxene + Quartz	M
179702	12	50		1						37	2				39	15			19	5			19	Mg-chlorite, Epidote, pyroxene + plagioclase	M
179729	34	32	16	8						10	1		6		20	10			18				45	Epidote, Mg-chlorite, Pyroxene	M
179735	10	33		1						56	1		3		12	34			14				36	Epidote, Mg-chlorite, pyroxene + plagioclase	M
179775	31	48								21	7				27	10			10	5		12	29	Mg-chlorite, Epidote, Pyroxene	M
179777	10	45								44					17	15			11				56	Epidote, Mg-chlorite, Pyroxene	M
179877	6	50		19						24	20				1	44			5				31	Pyroxene, Epidote, Mg-chlorite	M
179882	6	72								22	10				5	16			2				67	Mg-chlorite, Pyroxene, Epidote	M
179884	1	95								5	21		1		6	12			23			1	35	Mg-chlorite, Pyroxene, Epidote+Plagioclase	M
180202	30	48								21	26				2	17			11				44	Epidote, Mg-chlorite, Pyroxene	M
180205	7	33								60	11		4			22			20				41	Mg-chlorite, Epidote, Pyroxene	M
179710	1					4	2	58		35	1				39				14	16		2	29	Prehnite + Quartz	N
179723	66			7		18				9					31	2			36	1			29	Epidote, prehnite + plagioclase, Quartz	N
179869	1	1		1		48	3	36		10					77				6	2		1	14	Prehnite, Margarite + Quartz	N
179870	28			1		63				8					82					7			10	Prehnite, Epidote + Quartz	N
179894	58	1		12		29				15	3				12				7	9		16	52	Epidote, prehnite + plagioclase, Quartz	N
179895	55	8		23		11				10	5				12				29	6		4	42	Epidote, Mg-Fe chlorite + Plagioclase, Prehnite	N
179896	26					74				4	9				67				13	5			7	Prehinte, Epidote +Quartz, Plagioclase	N
180212	30			2		64				4					71					12		4	13	Prehnite, Epidote + Quartz	N
176798								99		0	1				77				6	6			10	Margarite + Quartz	P
179724	1			1		3	2	4		88														Margarite??	P
179726				1		3	3	5		88														Margarite??	P
179740							55	43		3					39	1			18	17		10	16	Illite/Muscovite+Quartz, Plagioclase	P
179871						5	74	1		19					53				9	21	1		17	Illite/Muscovite+Quartz, Plagioclase	P

Sample no.	SWIR mineral abundances (%)										LWIR mineral abundances (%)													Interpreted metamorphic mineral assemblages by qualitatively combining SWIR and LWIR mineral abundances	Assemblage code
	Epidote	Mg-Chlorite	Fe-Chlorite	Mg-Fe Chlorite	Actinolite/Hbl	Prehnite	Illite/Muscov	Margarite	Pyrophyllite	Unclassified	Epidote	Chlorite	Actinolite	Hornblende	Quartz	Jadeite	Enstatite	Oligoclase	Albite	Illite/Muscov	Pyrophyllite	Cordierite	Unclassified		
180214							92			8					27				40	10		12	10	Illite/Muscovite+Quartz, Plagioclase	P
179872	2	8		1		17	1	1		69					37				13	29		3	17	Prehnite, Illite/Muscovite+ Quartz	P
179897									95	5					1				2		91	2	5	Pyrophyllite	P
179898									88	12					6				1		84	2	6	Pyrophyllite + Quartz	P
179899							99			1		1			39				26	11		6	17	Illite/Muscovite+Quartz, Plagioclase	P
180223							87			13					84					1	1		13	Illite/Muscovite+Quartz	P
180225							90			10					17				34	21	1	2	25	Illite/Muscovite+Quartz, Plagioclase	P

Appendix 4: Thin section interpretation using JEOL EDS System

Sample 179766

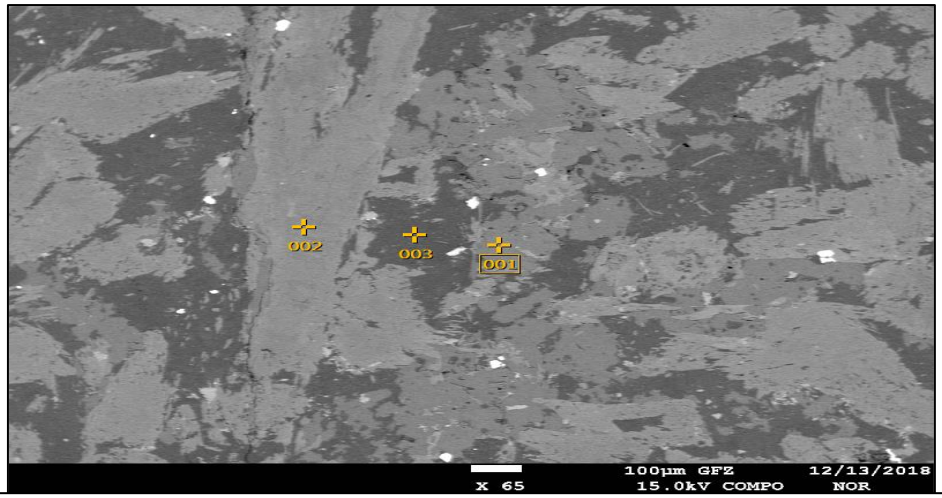

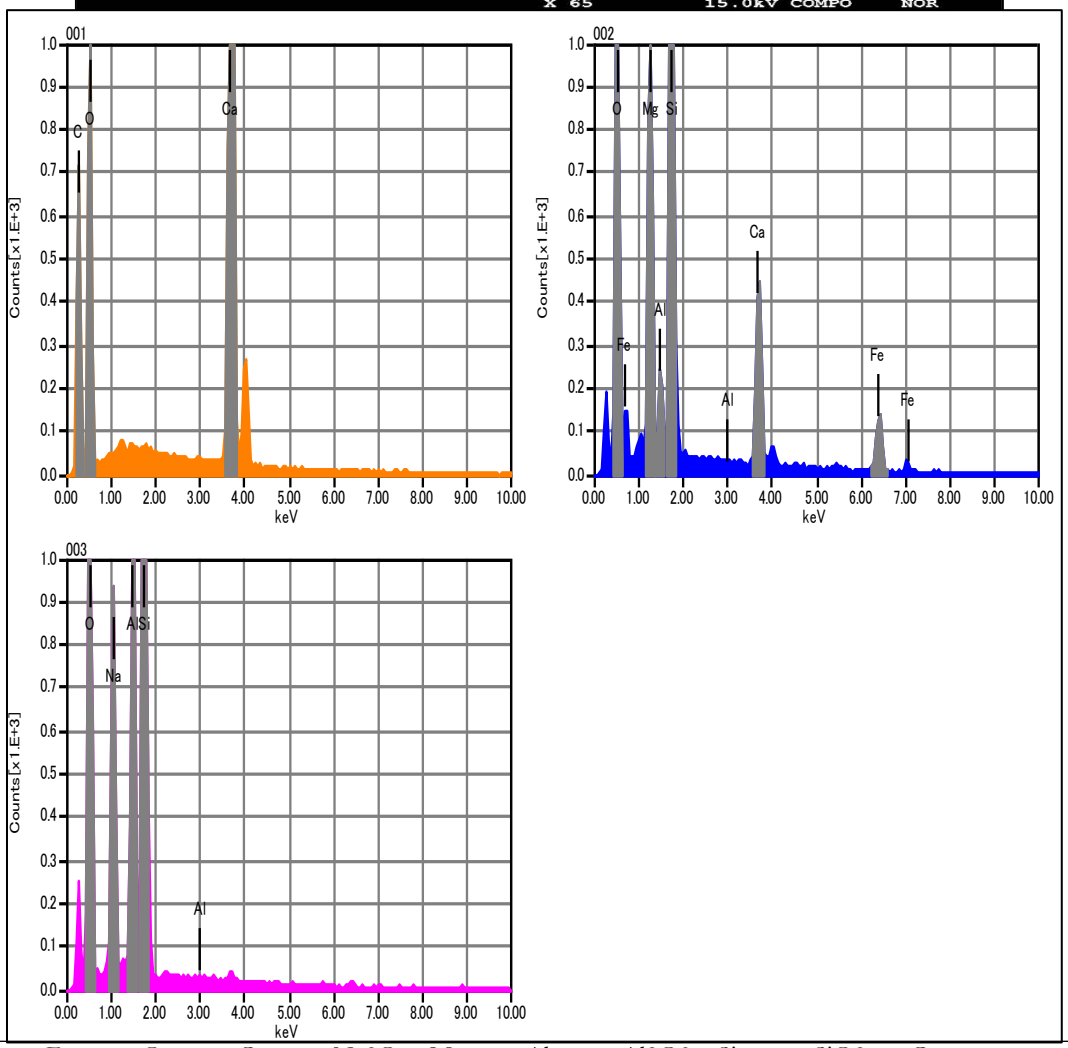

	Fe	O	C	Na2O	Mg	Al	Al2O3	Si	SiO2	Ca	
001		45.40	19.98							34.62	Calcite
002	9.03	47.67			9.50	1.50		24.01		8.28	Hornblende
003		0.00		11.00			19.41		69.59		Albite

Sample 179766…continue

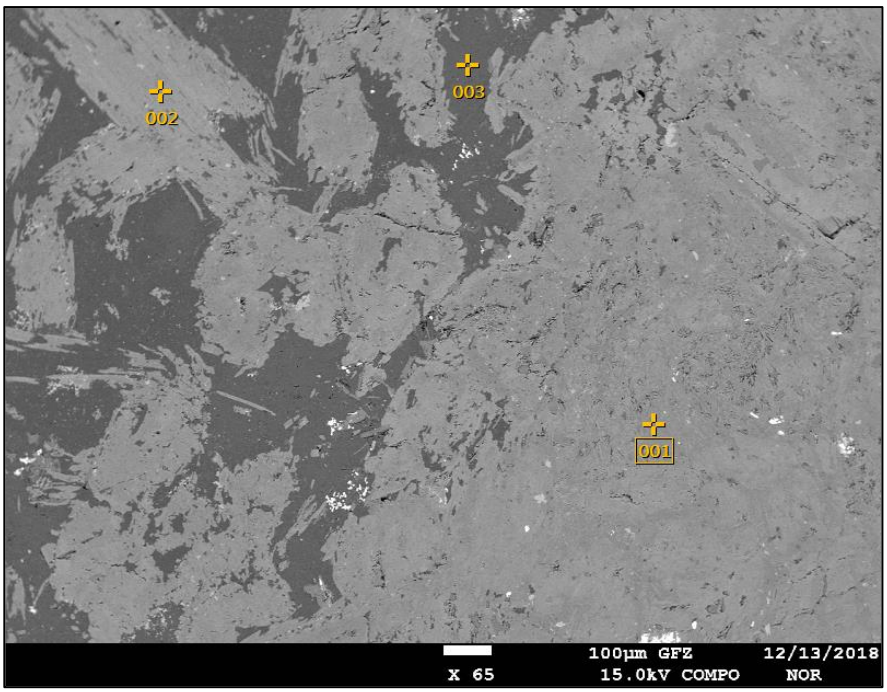

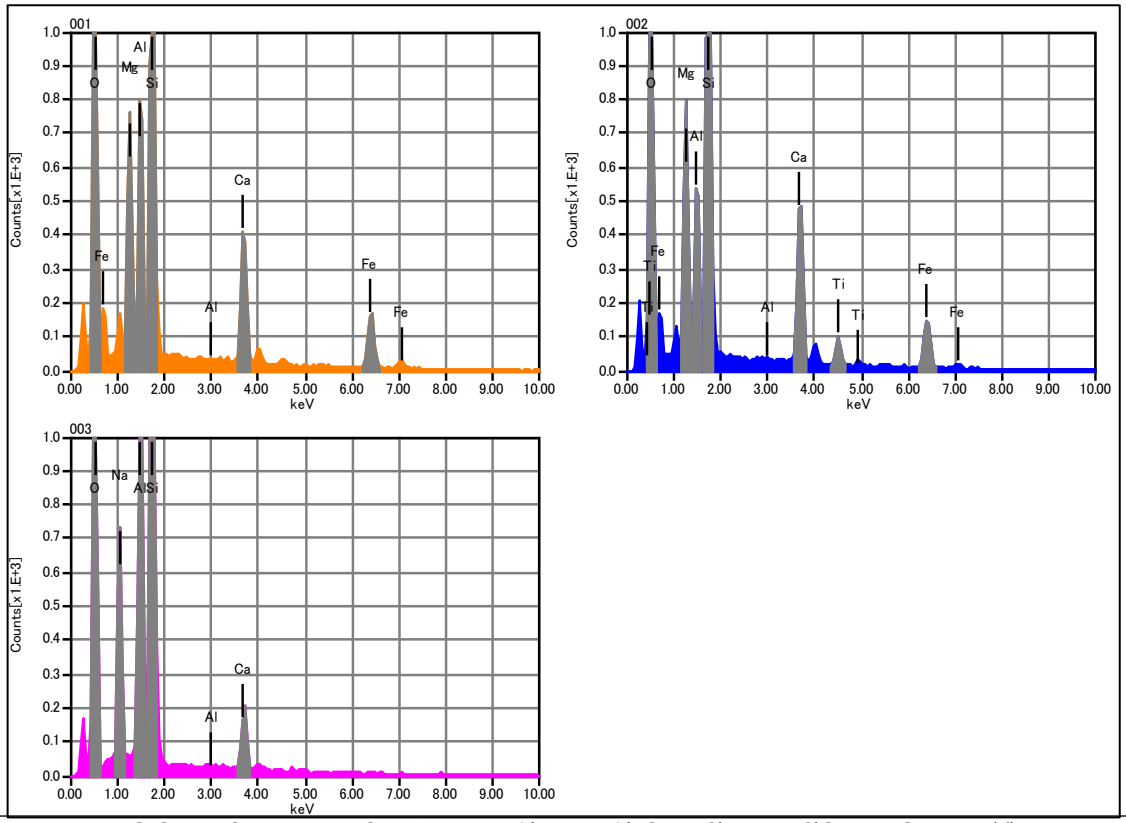

	Fe	CaO	O	Na2O	Mg	Al	Al2O3	Si	SiO2	Ca	Ti	
001	12.57		46.56		6.28	6.25		20.51		7.83		Hornblende
002	9.64		48.65		6.29	4.02		19.71		9.28	2.42	Hornblende
003		5.63	0.00	8.75			23.85		61.78			Albite

Sample 179722

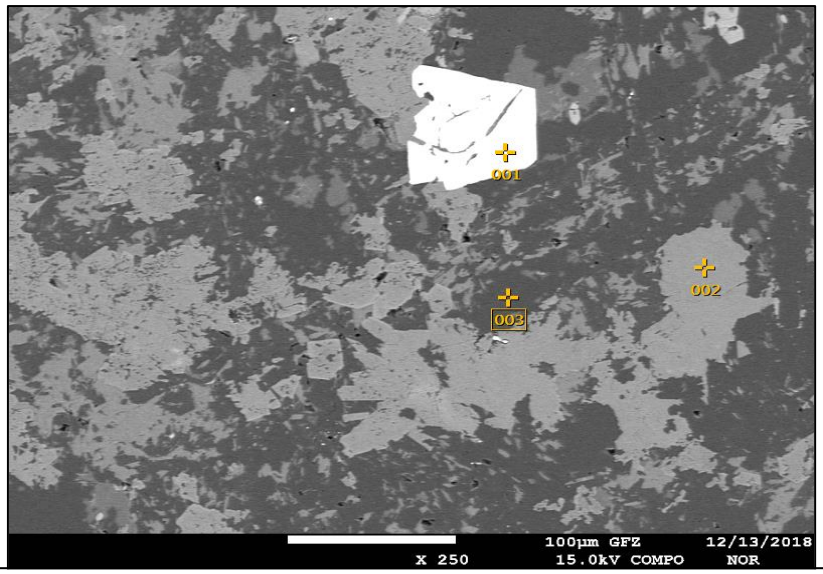

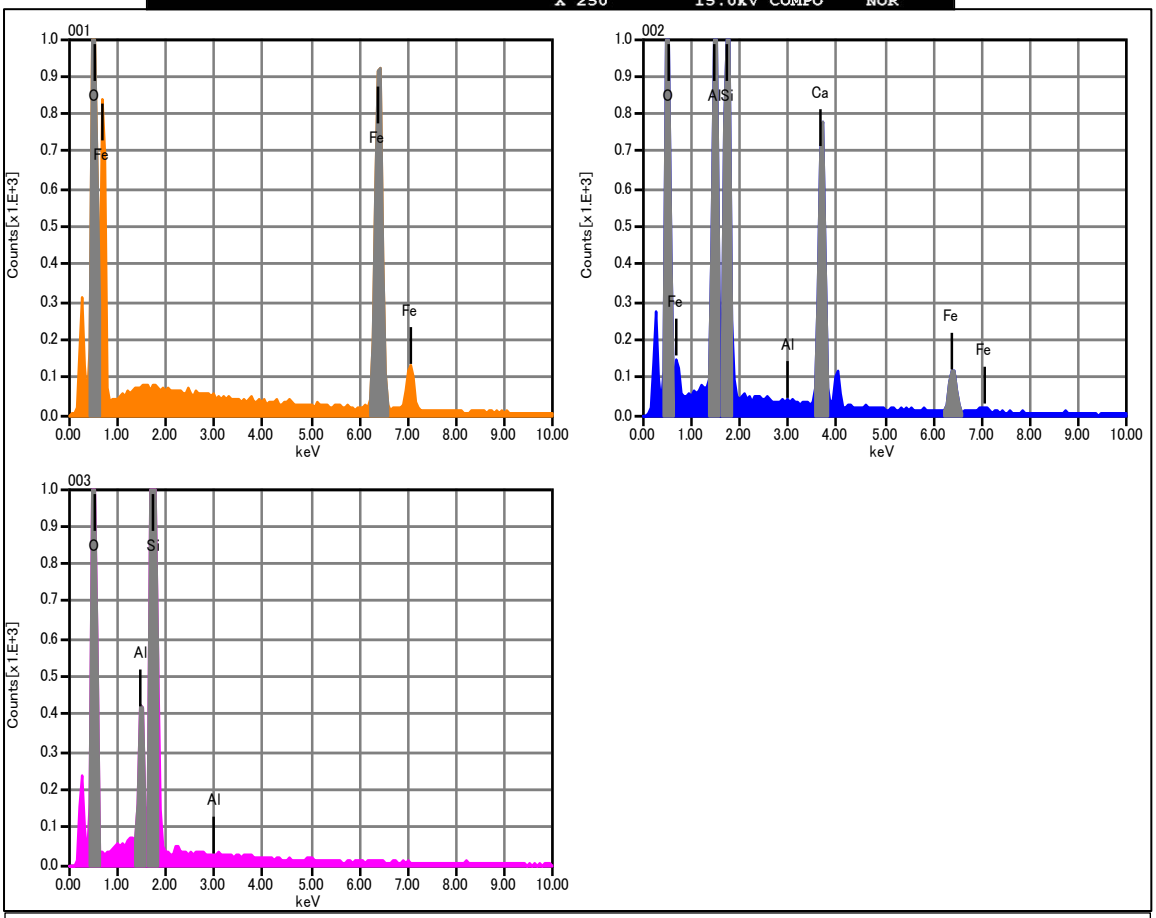

	CaO	O	Al2O3	SiO2	FeO	
001		0.00			100.00	Iron
002	23.36	0.00	23.86	40.86	11.92	Epidote
003		0.00	5.37	94.63		Quartz

Sample 179722…continue

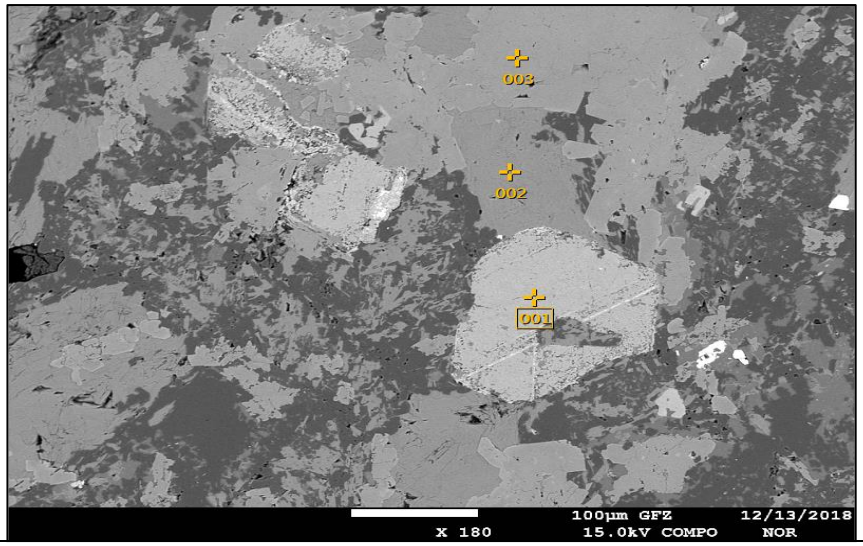

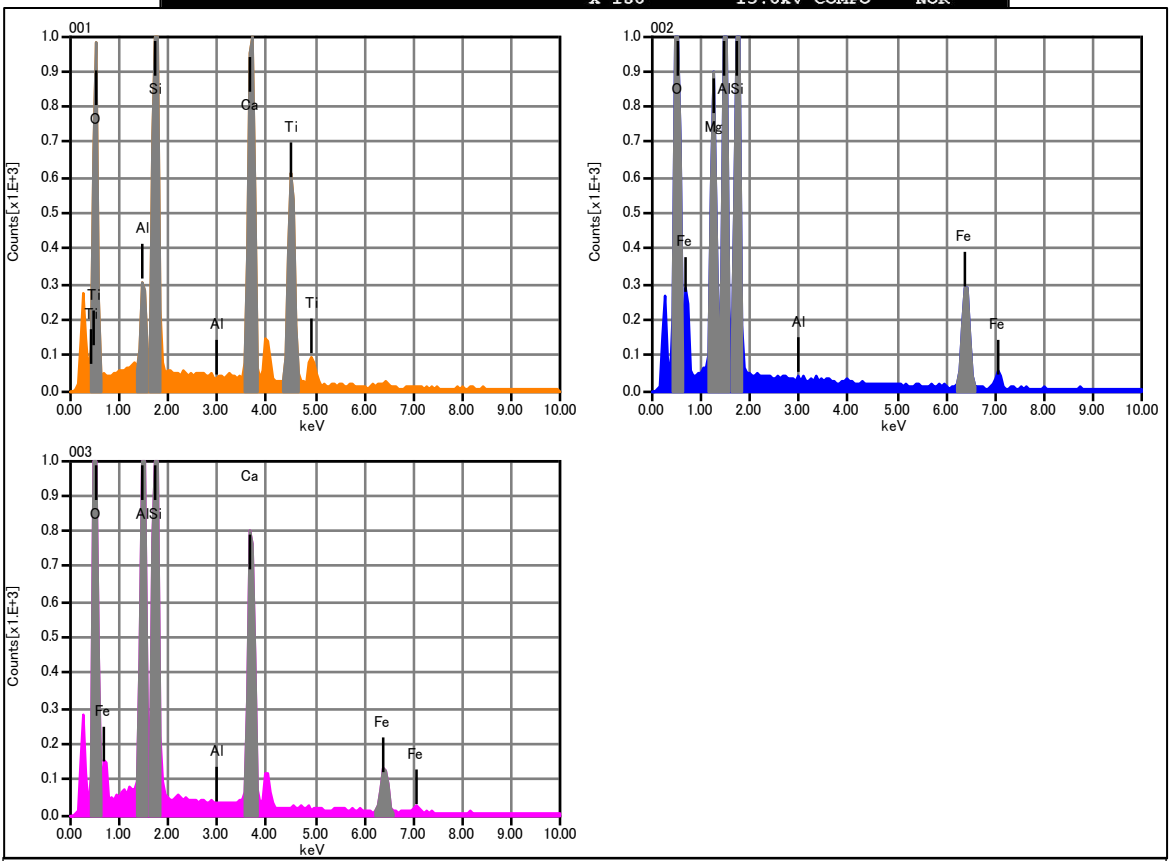

	Fe	CaO	O	Mg	Al2O3	Al	SiO2	Si	TiO2	FeO	
001		29.76	0.00		3.64		31.60		35.00		Titanite
002	21.90		48.49	8.00		9.95		11.65			Chlorite
003		23.51	0.00		24.18		39.88			12.43	Epidote

Sample 179725

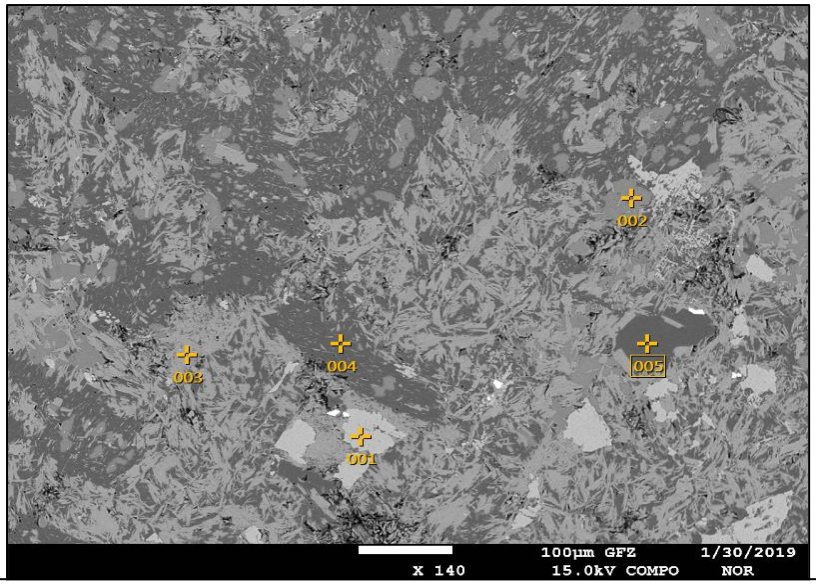

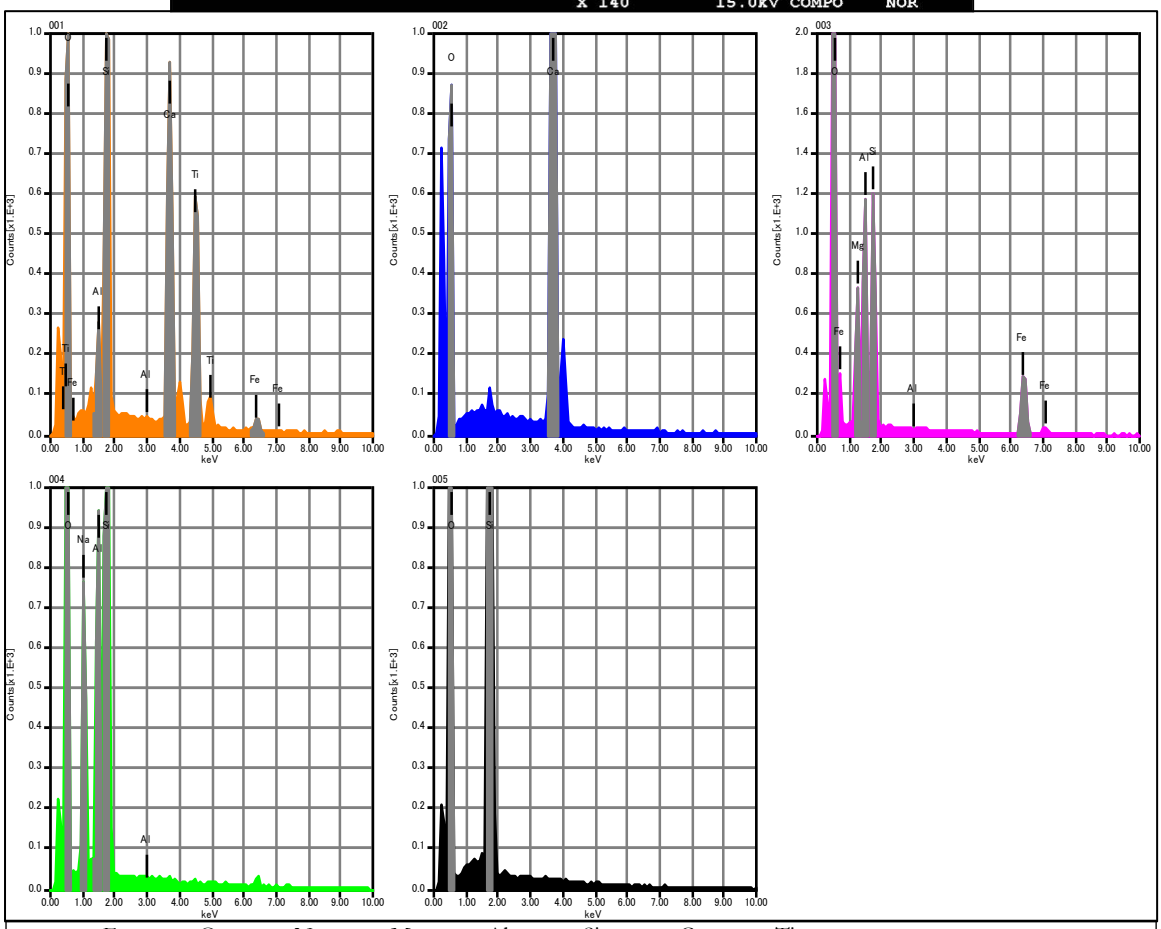

	Fe	O	Na	Mg	Al	Si	Ca	Ti	
001	2.09	43.13			1.76	14.33	18.86	19.83	Titanite
002		52.88					47.12		Calcite
003	21.95	49.04		6.84	10.45	11.71			Chlorite
004		51.85	6.82		7.45	33.88			Albite
005		54.52				45.48			Quartz

Sample 179725…continue

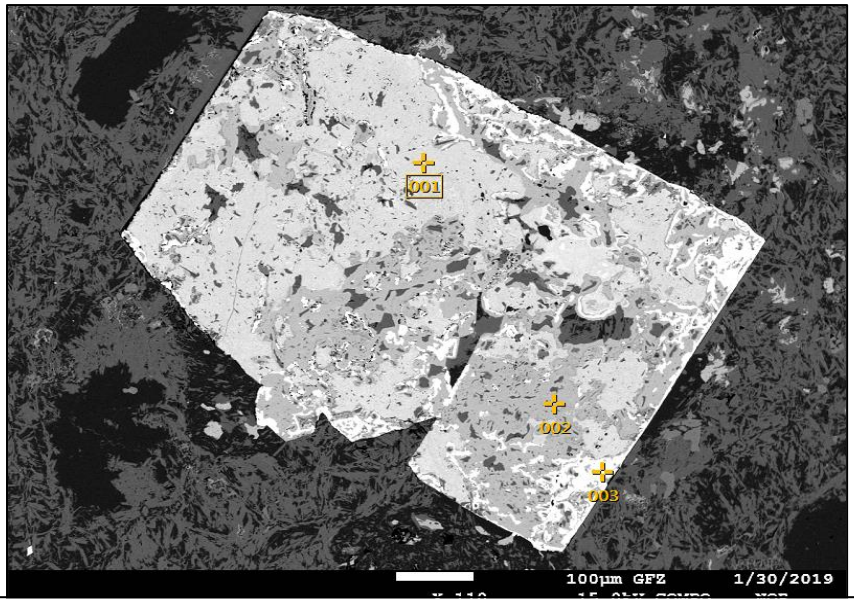

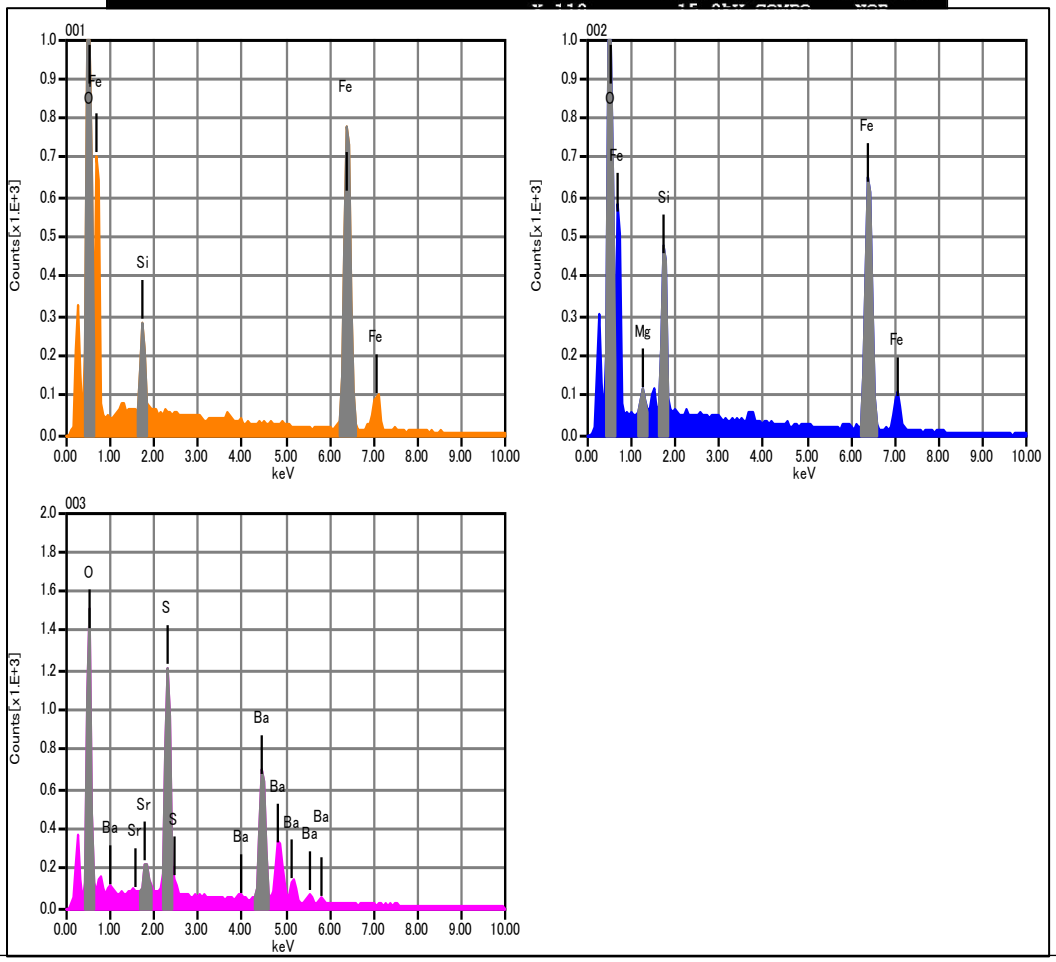

	Fe	O	Mg	SiO2	Si	S	FeO	Sr	Ba	
001		0.00		6.36			93.64			Enstatite
002	52.08	42.48	0.75		4.68					Hyperthene
003		27.64				13.89		3.74	54.73	Barite

Sample 179716

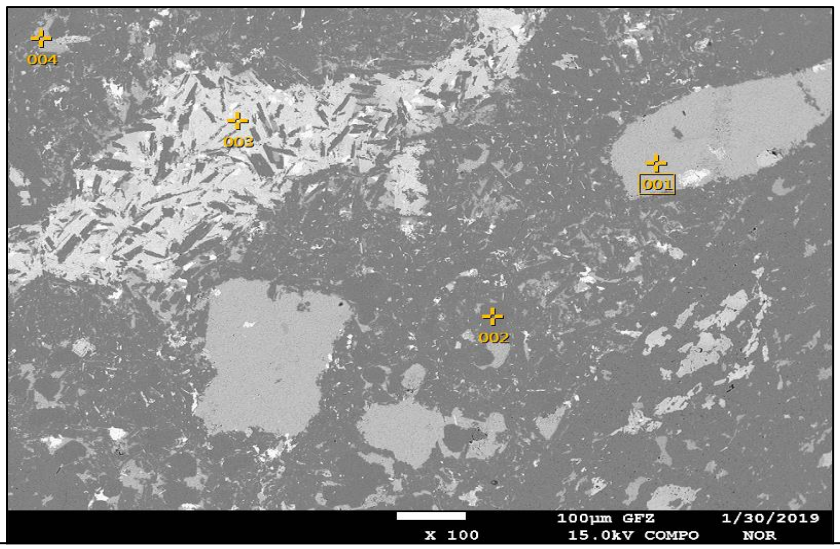

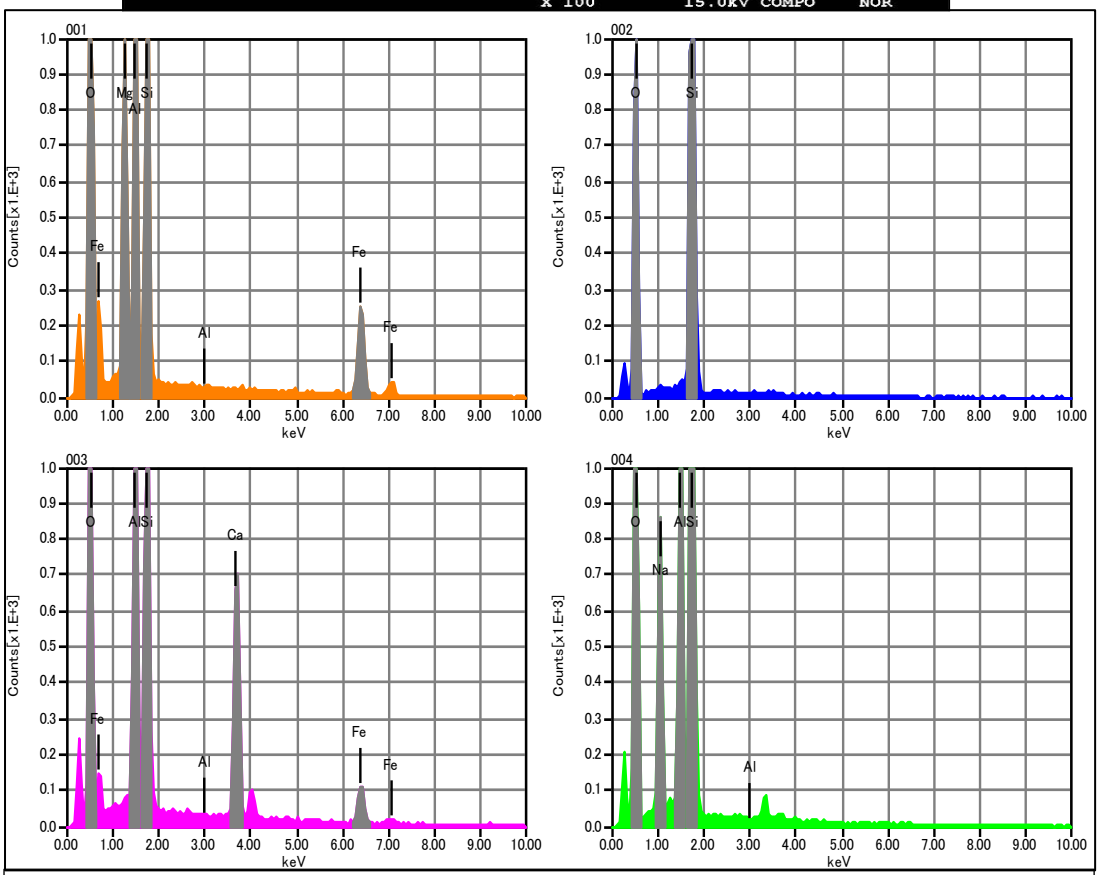

	Fe	O	Na2O	Mg	Al	Al2O3	Si	SiO2	Ca	
001	18.37	50.15		9.62	9.61		12.24			Olivine
002		0.00						100.00		Quartz
003	8.82	46.59			11.95		17.16		15.47	Epidote
004		0.00	10.37			20.25		69.38		Albite